Chapter 12

Applications to Soft Matter

In this chapter we describe some of the ways in which methods taken from the theory of simple liquids have been adapted to the study of much more complicated, molecular or macromolecular assemblies, generically referred to as *complex fluids* or *soft matter*.[1] Those labels encompass a wide variety of systems including, among others, polymer solutions and polymer melts, dispersions of colloidal particles of various sizes and shapes, thermotropic and lyotropic liquid crystals, and micelles, membranes or vesicles formed by ampiphilic surfactant molecules such as lipids. A theme common to all the example we discuss is the abandonment of the microscopic picture employed for simple systems in favour of a coarse-grained representation from which unnecessary detail has been eliminated.

12.1 COARSE GRAINING AND EFFECTIVE INTERACTIONS

The main barrier to the development of a fully microscopic description of complex fluids lies in the coexistence of widely different scales of length and time within the same system. Consider, for example, the case of an aqueous dispersion of colloidal particles that carry a high surface charge. The dimensions of the dispersed particles are typically of the order of tens or hundreds of nanometres and they move on time scales of the order of a nanosecond or microsecond, whereas the water molecules and microscopic counterions are much smaller (a fraction of a nanometre) and move much faster (on a picosecond time scale). A treatment of such highly asymmetric systems by the theoretical methods of earlier chapters would therefore be impractical, as would the use of numerical methods such as molecular dynamics simulation. However, the focus of interest often lies in the mesoscopic structure and dynamics of the colloidal particles rather than in the microscopic behaviour of the much smaller and lighter molecules and ions, which provide a thermal bath through which the large particles move. In that situation the problem can be greatly simplified by adoption of a coarse-graining strategy in which statistical averages are taken over the microscopic degrees of freedom for given configurations of the large

Theory of Simple Liquids, Fourth Edition. http://dx.doi.org/10.1016/B978-0-12-387032-2.00012-X

particles. This approach leads to the definition of effective interactions between 'dressed' colloidal particles which no longer depend on the microscopic details of the bath. Dynamical coarse graining switches from the newtonian equations of motion of both small and large particles to Langevin or brownian dynamics of the large particles alone; this involves a more elaborate procedure. We shall see examples of both forms of coarse graining in later sections.

We show first how a formally exact expression for the effective interaction between large particles can be derived, taking as a simple example that of a system consisting of N_1 large, spherical particles with coordinates $\{\mathbf{R}_i\}$ and $N_2 \gg N_1$ small particles with coordinates $\{\mathbf{r}_j\}$, all contained in a volume Ω. The total potential energy of the system is the sum of three terms:

$$V_{N_1N_2}(\{\mathbf{R}_i\},\{\mathbf{r}_j\}) = V_{11}(\{\mathbf{R}_i\}) + V_{22}(\{\mathbf{r}_j\}) + V_{12}(\{\mathbf{R}_i\},\{\mathbf{r}_j\}) \qquad (12.1.1)$$

corresponding to the interactions between large particles, that between small particles and the cross-interaction between them. The configuration integral of the mixture is then

$$\begin{aligned} Z_{N_1N_2} &= \int \exp\left(-\beta V_{N_1N_2}\right) \mathrm{d}\mathbf{R}^{N_1}\, \mathrm{d}\mathbf{r}^{N_2} \\ &= \int \mathrm{d}\mathbf{R}^{N_1} \exp\left(-\beta V_{11}\right) \int \mathrm{d}\mathbf{r}^{N_2} \exp[-\beta(V_{22}+V_{12})] \\ &= \Omega^{N_2} \int \mathrm{d}\mathbf{R}^{N_1} \exp[-\beta V_{11}(\{\mathbf{R}_i\}) - \beta F_2^{\mathrm{ex}}(\{\mathbf{R}_i\})] \end{aligned} \qquad (12.1.2)$$

where the definition (2.3.20) has been used. The quantity $F_2^{\mathrm{ex}}(\{\mathbf{R}_i\})$ is the excess free energy of the system of small particles in the external field V_{12} due to large particles fixed at positions $\{\mathbf{R}_i\}$. The dimensionless configuration integral $Z_{N_1N_2}/\Omega^N$, with $N = N_1 + N_2$, may therefore be written as

$$\frac{Z_{N_1N_2}}{\Omega^N} = \frac{Z_{N_1}}{\Omega^{N_1}} = \frac{1}{\Omega^{N_1}} \int \exp[-\beta V_{11}^{\mathrm{eff}}(\{\mathbf{R}_i\})] \mathrm{d}\mathbf{R}^{N_1} \qquad (12.1.3)$$

where the total, effective interaction between the large particles is

$$V_{11}^{\mathrm{eff}}(\{\mathbf{R}_i\}) = V_{11}(\{\mathbf{R}_i\}) + F_2^{\mathrm{ex}}(\{\mathbf{R}_i\}) \qquad (12.1.4)$$

The first term on the right-hand side corresponds to the direct interactions between large particles; the second term represents the interactions induced by the small ones. The induced term arises from integration over the coordinates of the small particles. It is therefore a free energy that depends parametrically on the positions of the large particles, meaning that the effective interaction is a state-dependent quantity to which there is an entropic contribution given by $-TS_2^{\mathrm{ex}}(\{\mathbf{R}_i\})$. Because the induced term is many-body in nature, the effective interaction between the large particles will not be pairwise additive, even when that is true of all three contributions to $V_{N_1N_2}$.

Explicit calculation of the effective potential is, in general, a difficult problem. Its solution relies on the use of approximations, often implemented within the framework of the density functional theory of an inhomogeneous fluid of small particles in the spatially varying potential $V_{12}(\{\mathbf{R}_i\}, \{\mathbf{r}_j\})$ due to the large particles. Two classic examples are the screened interaction between electric double layers, already discussed in Section 10.6, and the depletion interaction between colloidal particles induced by non-adsorbing polymers. Similar methods have been used in coarse-grained descriptions of interacting polymers in solution. We shall say more about all three problems in later sections. Two other, important examples of effective interaction should also be mentioned. One is the hydrophobic attraction between nano-sized or larger particles referred to at the end of Section 6.7. This plays a key role in molecular biology in relation to the stability of protein solutions. The second example is that of the fluctuation-induced Casimir force between surfaces, an effect that results from spatial confinement of critical fluctuations near a second-order phase transition. Let us take the case of a binary, liquid mixture near its critical consolute point, which is analogous to the liquid–gas critical point. The correlation length ξ, which measures the distance over which local concentrations are correlated, diverges when the critical temperature is approached at the critical concentration. If a near-critical mixture is confined to the region between the surfaces of two large, colloidal particles, critical fluctuations cannot develop beyond the surface-to-surface distance L. If $\sigma \ll L < \xi$, where σ measures the size of the microscopic fluid particles, confinement leads to a long-range attraction between the surfaces. The resulting force has been determined very accurately by use of a sophisticated dynanometer in conjunction with total internal reflection microscopy,[2] with results that are in excellent agreement with theoretical predictions. The strength of the interaction is comparable with the thermal energy and can strongly affect the stability of colloidal dispersions in a near-critical solvent.

The coarse-graining approach described here is applicable to complex fluids involving length scales that may differ by several orders of magnitude. Related approaches have been applied to assemblies of large molecules, such as alkanes or phospho-lipids, where small groups of atoms or functional groups are replaced by single interaction sites within a 'united atom' description, thereby reducing the resolution achievable by roughly an order of magnitude. Force fields of this type are used to speed up molecular dynamics simulations of complex processes such as aggregation and self-assembly. The same method has been used, mostly in *ad hoc* form, since the early days of computer simulation, but a more refined approach has subsequently evolved in which emphasis is placed on matching the results obtained from coarse-grained and atomistic descriptions.[3] At a more fundamental level a variational principle has been derived that provides a recipe for construction of a coarse-grained potential model for which the interaction-site distribution functions are consistent with the atomic distributions in the underlying, atomically detailed model.[4]

12.2 POLYMER SOLUTIONS

Polymer is a generic name for elongated, linear or branched molecules of high molecular weight. *Homopolymers* consist of long sequences of a single unit or *monomer*. Their dimensionless, reduced properties obey certain scaling laws in the limit in which the number of monomers becomes very large; these laws are independent of the chemical nature of the monomer involved. *Heteropolymers* consist of sequences of different monomeric species, which may be distributed along the molecule in either regular or random fashion. Homopolymers and regular, block copolymers are the systems which, by virtue of their chemical homogeneity, are best adapted to a coarse-grained description of their properties. Much of the material covered in this section and the one that follows is concerned specifically with linear (or 'chain') polymers, but some reference is also made to star polymers and block copolymers. For readers unfamiliar with the field, Appendix G provides a brief summary of the basic properties of polymers and establishes the notation used in this and later sections. Excellent introductory texts[5] also exist, together with several classic books[6] devoted to theory at a more advanced level.

The properties of polymer solutions are largely controlled by two factors: polymer density and solvent quality. The effect of changes in density can be discussed in terms of the *overlap density*

$$\rho^{\mathrm{o}} = \frac{3}{4\pi R_{\mathrm{g}}^3} \tag{12.2.1}$$

where R_{g} is the radius of gyration defined by (G.1). The overlap density is the number density beyond which polymer coils will, on average, overlap, since the mean volume of a single polymer, equal to $1/\rho^{\mathrm{o}}$, will then exceed the volume per polymer, $V/N = 1/\rho$. The range of monomer density is conventionally divided into the three regions pictured in Figure 12.1, corresponding to a dilute solution ($\rho < \rho^{\mathrm{o}}$), the onset of chain overlap ($\rho \sim \rho^{\mathrm{o}}$) and a semi-dilute solution

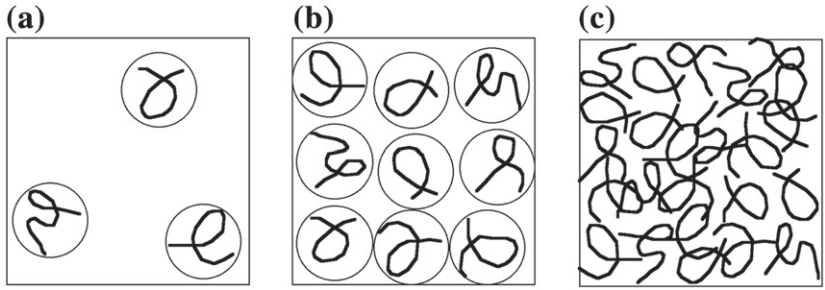

FIGURE 12.1 The three ranges of density described in the text for a system of chain polymers: (a) $\rho < \rho^{\mathrm{o}}$, (b) $\rho \sim \rho^{\mathrm{o}}$ and (c) $\rho > \rho^{\mathrm{o}}$.

($\rho > \rho^{o}$). Still higher densities are found in polymer melts, discussion of which is postponed until Section 12.3. The quality of a solvent is described as either 'good' or 'poor'. Good solvent conditions correspond to high temperatures, at which the effect of the short-range, repulsive interaction between monomers outweighs that of the attractive interaction; this leads to a swelling of the polymer coils. At low temperatures the reverse is true. The attractive forces are now dominant and the coils contract as the temperature is reduced until, in dilute solutions, the polymer becomes unstable against *coil-globule collapse*. The temperature at which the interactions balance each other is called the θ-temperature, T_θ. In 'θ-solvent' conditions the polymer behaves like an ideal chain of non-interacting monomers in a manner similar to that of an imperfect gas at the Boyle temperature.

In dilute solution polymer coils rarely overlap and in the limit $\rho \to 0$ the properties of individual polymers depend only on temperature. In particular, the osmotic pressure Π of an ultra-dilute solution is given by van't Hoff's law, $\beta\Pi = \rho$. As the density increases the probability of binary overlap also increases. This leads to deviations from ideal behaviour of a magnitude determined by the osmotic second virial coefficient:

$$\beta\Pi = \rho + B_2(L,T)\rho^2 + \mathcal{O}(\rho^3) \tag{12.2.2}$$

The virial coefficient, a function of polymer length and temperature, is defined by a generalisation of (3.9.7):

$$B_2(L,T) = \frac{1}{2}\int \left\langle 1 - \exp\left[-\beta V_2(1,2)\right]\right\rangle_{\mathbf{0},\mathbf{R}} \, \mathrm{d}\mathbf{R} \tag{12.2.3}$$

where the centre of mass or some other chosen centre of coil 1 is placed at the origin, that of coil 2 at $\mathbf{R}$, and $V_2(1,2)$ is the total energy of interaction between monomers on different coils. The statistical average in (12.2.3) must be taken over all chain conformations of the two coils for a given microscopic model of the polymer; its evaluation usually relies on data obtained by computer simulation. The dimensionless ratio

$$A_2(L,T) = \frac{B_2(L,T)}{R_{\mathrm{g}}^3(L,T)} = A_2^* + \frac{a_2(T)}{L^\delta} + \cdots \tag{12.2.4}$$

involves a quantity A_2^* which has a universal value in the scaling limit, where the polymer length $L \to \infty$, and a universal exponent $\delta \approx 0.517$, whereas the coefficient $a_2(T)$ of the first finite-size correction is model dependent.[7] The value of A_2^* has been calculated by extrapolation to infinite L of the results of Monte Carlo calculations of $A_2(L,T)$ for two self-avoiding walk (SAW) polymers, giving $A_2^* = 5.494 \pm 0.005$. A numerical estimate of the third virial coefficient has also been obtained but the calculation of higher-order coefficients poses severe computational problems.

A different description of dilute solutions is that based on a coarse-graining approach, first proposed by Flory and Krigbaum,[8] which involves integration

over monomer degrees of freedom for fixed coordinates of the polymer centres of mass. Let $\mathbf{R}_i$ be the centre-of-mass coordinates and let $\mathbf{r}_{i\alpha}$ be the coordinates of a monomer α of a chain labelled i. Then the probability distribution of centres of mass is

$$P_N(\{\mathbf{R}_i\}) = \frac{1}{Z_N}\int \exp\left[-\beta V_N(\mathbf{r}_{i\alpha})\right]\prod_{i=1}^{N}\delta\left(\mathbf{R}_i - \frac{1}{M}\sum_{\alpha=1}^{M}\mathbf{r}_{i\alpha}\right)\prod_{i=1}^{N}\prod_{\alpha=1}^{M}\mathrm{d}\mathbf{r}_{i\alpha} \tag{12.2.5}$$

where M is the number of monomers per chain, V_N is the total interaction energy and Z_N is the configuration integral. The effective interaction energy between the centres of mass is related to the probability distribution by

$$V_N^{\mathrm{eff}}(\{\mathbf{R}_i\}) = -k_{\mathrm{B}}T\ln\left[\mathcal{C}P_N(\{\mathbf{R}_i\})\right] \tag{12.2.6}$$

where $\mathcal{C}$ is an irrelevant constant which fixes the zero of energy. As discussed in Section 12.1, the effective energy is a free energy, and will therefore, in general, be many-body in nature. In the low-density limit, however, it will be pairwise additive, with an effective pair potential between centres of mass given by

$$\begin{aligned}\beta v_2^{\mathrm{eff}}(R) &= -\ln\left[\mathcal{C}P_2(|\mathbf{R}_2-\mathbf{R}_1|=R)\right]\\ &= -\ln\left\langle\exp\left[-\beta V_2(\{\mathbf{r}_{1\alpha}\},\{\mathbf{r}_{2\beta}\})\right]\right\rangle_{|\mathbf{R}_2-\mathbf{R}_1|=R}\end{aligned} \tag{12.2.7}$$

The statistical average is taken over conformations of the two chains for a fixed value of the separation R of their centres of mass. In common with the second virial coefficient, the pair potential is dependent on both L and T. Once the effective pair potential has been determined, typically from a Monte Carlo simulation of a system of two interacting polymers, the second virial coefficient is obtained by integration:

$$B_2(L,T) = \frac{1}{2}\int\left(1-\exp[-\beta v_2(R)]\right)\mathrm{d}\mathbf{R} \tag{12.2.8}$$

where the superscript 'eff' has now been dropped. A knowledge of the virial coefficient allows the calculation of the lowest-order correction to van't Hoff's law, but the potential may also be used to determine other properties of the solution.

The effective pair potential is expected to be soft even if the monomer–monomer potential contains a strongly repulsive component. We show in Appendix G that in good solvent the radius of gyration of a chain behaves as bL^{ν}, where b is the monomer diameter and $\nu \approx \frac{3}{5}$. This implies that above the θ-temperature the monomer volume fraction ϕ_{m} within a single coil behaves as $L/R_{\mathrm{g}}^3 \sim L^{1-3\nu} \sim L^{-4/5}$. That fraction will be very small when $L \gg 1$, in which case two polymer coils can easily interpenetrate. At full overlap, where the two centres of mass coincide, the potential has been shown[9] to scale as L^0, meaning that it is finite and independent of L in the scaling limit. Its range

is expected to be of the same order as the coil size, R_g. These findings have been confirmed by Monte Carlo simulations[10] of pairs of hard-sphere chains and SAW polymers with results which show that $\beta v_2(R)$ is reasonably well-represented by a gaussian function of the form

$$\beta v_2(R) \approx A \exp\left[-\alpha (R/R_g)^2\right] \tag{12.2.9}$$

where A and α are constants. For these athermal models the effective potentials are of purely entropic origin and therefore proportional to $k_B T$, but their application is limited to high temperatures where the interaction between monomers is dominated by excluded volume effects. As the temperature is reduced towards T_θ, the models must be augmented by terms that takes account of solvent induced, attractive interactions. When this is done, the effective potential acquires an additional temperature dependence; the amplitude A in (12.2.9) decreases with T and an attractive tail appears[11] for distances beyond R_g. It is also found that below a well-defined 'stability' temperature T_S the potential violates the condition required[12] for the existence of a thermodynamic limit, namely

$$I_2 = \int v_2(R) \mathrm{d}\mathbf{R} > 0 \tag{12.2.10}$$

The critical temperature T_S may be identified as the temperature below which coil-globule collapse occurs, given implicitly for a chain of length L by the relation

$$I_2(L, T = T_S) = 0 \tag{12.2.11}$$

On the other hand the θ-temperature is the temperature at which attractive and repulsive forces balance and the second virial coefficient vanishes. It is therefore determined by the condition

$$\lim_{L\to\infty} B_2(L, T = T_\theta) = 0 \tag{12.2.12}$$

Equation (12.2.12) has been used to estimate the θ-temperature of the SAW model with results that are consistent with those obtained in other ways.[13] The relationship between T_S and T_θ is less clear.

The low density, effective pair potential (12.2.9) is a special case of the purely repulsive, gaussian-core model,[14] for which

$$v_2(R) = \epsilon \exp\left[-(R/R_0)^2\right] \tag{12.2.13}$$

where ϵ and R_0 measure, respectively, the strength and range of the interaction. This model is of interest in its own right as one that exhibits a re-entrant fluid–solid phase diagram in the density–temperature plane; freezing is followed by a structural phase transition and then by remelting.[15] At high densities, where each particle is overlapped by many others, the behaviour is of mean field type[16] and accurately described by the random phase approximation of

(3.5.17), which becomes exact in the limit $\rho R_0^3 \to \infty$. Since there is no hard core, the reference part of the potential is zero, $w(r) = v_2(r)$ and (within the RPA) $c(r) = -\beta v_2(r)$. The compressibility equation (3.5.15) then shows that in its application to polymer solutions the osmotic pressure is given by

$$\beta\Pi = \rho + \frac{1}{2}\hat{v}_2(k=0)\rho^2 = \rho + \frac{\pi^{3/2}}{T^*}R_0^3\rho^2 \tag{12.2.14}$$

This result applies to the high-density limit and the coefficient of the quadratic term inevitably differs from the second virial coefficient, which determines the leading correction to the van't Hoff equation of state.

For polymer solutions in good solvent the semi-dilute regime corresponds to polymer densities greater than the overlap density. Overlap of polymers is now greatly increased, as pictured in Figure 12.1, the identity of individual coils is lost, and the polymer chains form a network characterised by a spatially homogeneous distribution of monomers and a mesh size, or correlation length, ζ. The dependence of ζ on density can be derived by a simple scaling argument. Let $R_{g0} \sim bL^{\nu}$ be the radius of gyration of an isolated polymer, which we assume to be related to ζ in typical scaling form:

$$\zeta = R_{g0} f\left(\frac{\rho_m}{\rho_m^o}\right) \tag{12.2.15}$$

where $f(x)$ is a dimensionless scaling function, $\rho_m = M\rho \sim L\rho$ is the monomer density and $\rho_m^o = M\rho^o \sim b^3 L^{1-3\nu}$. When polymers overlap, ζ will be independent of L, implying that the scaling function represents a power law, $f(x) \sim x^{\gamma}$, say. Thus

$$\zeta \sim bL^{\nu}(\rho_m b^3 L^{3\nu}/L)^{\gamma} \sim b^{1+3\gamma}\rho_m^{\gamma} L^{\nu+3\nu\gamma-\gamma} \tag{12.2.16}$$

which shows that γ must be equal to $-\nu/(3\nu-1)$ and hence that

$$\zeta = R_{g0}\left(\frac{\rho_m}{\rho_m^o}\right)^{-\nu/(3\nu-1)} \sim b\left(\rho_m b^3\right)^{-3/4} \tag{12.2.17}$$

for $\nu = \frac{3}{5}$.

A similar argument can be used to determine the asymptotic variation of osmotic pressure with monomer concentration. For obvious dimensional reasons $\beta\Pi$ may be written in the form

$$\beta\Pi = \rho f\left(\frac{\rho_m}{\rho_m^o}\right) = \frac{\rho_m}{L} f\left(\frac{\rho_m}{\rho_m^o}\right) \tag{12.2.18}$$

where $f(x)$ is another scaling function and $\rho_m^o \sim L\rho^o \sim b^{-3}L^{1-3\nu}$. In the regime of high polymer overlap the length of individual polymers becomes irrelevant and $\beta\Pi$ should therefore be independent of L. This implies that $f(x)$ is again a simple power law, $f(x) \sim x^{\alpha}$, where $\alpha = 1/(3\nu-1)$, leading in turn to the expression for the osmotic pressure due to des Cloizeaux[17] in which Π

behaves asymptotically as $\rho_m^{9/4}$:

$$\beta \Pi b^3 \sim (\rho_m b^3)^{3\nu/(3\nu-1)} \sim (\rho_m b^3)^{9/4} \sim b^3/\zeta^3 \tag{12.2.19}$$

The scaling argument provides a value for the exponent but not the prefactor. The des Cloizeaux exponent is larger than the quadratic value predicted by the RPA, which is based on the use of an effective, gaussian core interaction between polymer coils. Since the RPA is asymptotically exact for the gaussian potential, the breakdown of (12.2.14) in the semi-dilute regime must be ascribed to the inadequacy of the effective pair potential for densities above ρ^o. In the semi-dilute regime the role of many-body forces become significant, but their effect can be allowed for in an approximate way by introduction of a state-dependent effective pair potential. The density-dependent potential for the athermal SAW model has been calculated by inversion of the pair distribution function of polymer centres of mass obtained by Monte Carlo simulations.[18] Inversion is achieved by use of the HNC closure relation (4.3.19), which is known to be very accurate for soft, penetrable-core models. In this approximation the pair potential is given by

$$\beta v_2(R) = h(R) - c(R) - \ln g(R) \tag{12.2.20}$$

where all quantities are functions of density; $g(R)$ (and hence $h(R)$) are given by simulation and the direct correlation function is derived from the Ornstein–Zernike relation. The distribution function that serves as input depends weakly on L and the results must be extrapolated to the scaling limit, $L \to \infty$. Corrections to the scaling limit of the potential have also been obtained[7]; the leading correction is proportional to $1/L^\delta$, with $\delta \approx 0.517$, as in (12.2.4).

Examples of the pair distribution function and the resulting pair potential are shown in Figure 12.2. As the density increases, the size of the 'correlation hole' in $g(R)$ at small R decreases and $g(R = 0)$ increases towards unity. Such behaviour is indicative of the fact that short-range correlations become weaker with increasing density. This is the reverse of what is found in the case of simple liquids, but is consistent with Flory's conjecture, discussed in the section which follows, that polymers behave like ideal chains at high densities. The pair potential has a gaussian-like form with a range that increases with density. The only unexpected feature is that the value at full overlap, $v_2(R = 0)$, varies non-monotonically with density, passing through a maximum at $\rho \approx 2\rho^o$. The state dependence of the potential precludes the use of the energy and virial equations, (2.5.20) and (2.5.22), for the calculation of thermodynamic properties, but the compressibility equation (3.5.15) remains applicable if the direct correlation function is calculated from the pair potential via the HNC equation. The osmotic pressure is then obtained by integration over density:

$$\beta \Pi = \int_0^\rho \rho'[1 - \rho' \hat{c}(k = 0; \rho')] \mathrm{d}\rho' \tag{12.2.21}$$

and is found to follow the des Cloizeaux scaling law for densities greater than about $2\rho^o$.

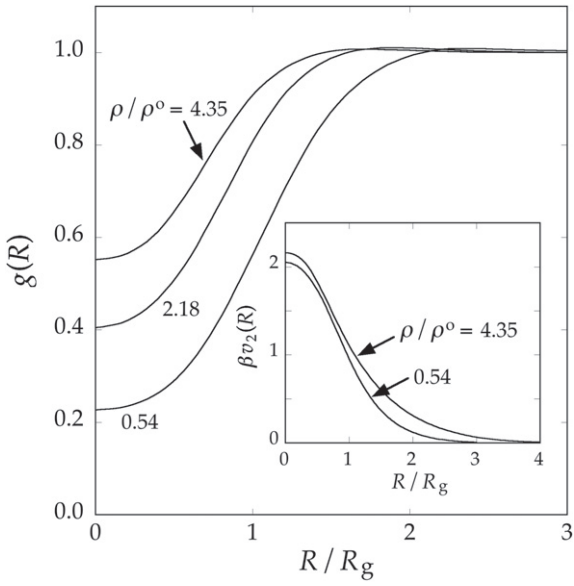

FIGURE 12.2 Pair distribution functions and effective pair potentials for polymers in a semi-dilute solution. *Redrawn with permission from Ref. 18 © 2001 American Institute of Physics.*

The same strategy can be pursued when the temperature is reduced from good solvent conditions to the θ-temperature and below,[11] but the potential is now dependent on both density and temperature. The collapse of isolated polymer coils into globules seen in dilute solutions at temperatures below T_θ is replaced by a polymer–solvent phase separation into a low-concentration phase of collapsed globules and a concentrated phase of stable polymer coils, with a concomitant lowering of the solvent volume fraction. This 'restabilisation' of concentrated polymer solutions is reflected in a strong density dependence of the pair potential, which satisfies the stability criterion (12.2.10) at sufficiently high densities. A disadvantage of the inversion procedure is the fact that its implementation relies on simulations of a microscopic model to extract the distribution function of centres of mass, which is a computationally costly procedure at high densities. The problem could be overcome by development of a theory that relates the mesoscopic distribution of centres of mass to the microscopic, monomer–monomer distribution. This can be achieved, at least approximately, by an extension (discussed below) of the RISM formalism of Section 11.8.

Soft-potential coarse graining applies to other polymer topologies and in particular to star polymers. These are made up of $f = 3$ or more linear branches, as shown in Figure G.1. The connection point of the branches is the natural choice of centre for a star polymer rather than the centre of mass. Scaling arguments[19] have shown that the effective interaction between two star polymers with SAW branches and centres separated by R behaves logarithmically when

R is less than R_g, i.e.

$$\beta v_2(R) = -\alpha f^{3/2} \ln (R/R_g), \quad R < R_g \tag{12.2.22}$$

where the prefactor α is a positive quantity. The potential therefore has a very soft but ultimately impenetrable core, since it diverges as $r \to 0$, in contrast to the effective potentials between the centres of mass of linear molecules. It becomes more stiffly repulsive as the number of branches increases and interpenetration of two star polymers becomes entropically more costly. The form of (12.2.22) has been confirmed by Monte Carlo simulations, which also provide both the value of α and the variation of $v_2(R)$ with separation for $R > R_g$; the potential is everywhere repulsive.[20] Integral equations, thermodynamic perturbation theory and simulations, all based on an effective pair potential of that type, have been used to determine the phase diagram of star polymer solutions[19b] over a range of values of f.

For linear polymers the complications associated with use of a state-dependent effective pair potential in the semi-dilute regime can be by-passed[21] by representing each chain not by a single, penetrable sphere located at the centre of mass but by a chain of n tethered 'blobs', each representing a sequence of $m = M/n$ monomers, as pictured in Figure 12.3. The average size of a blob is given by its radius of gyration, $r_g \sim b\ell^\nu$, with $\ell = m - 1$ and $\nu \approx \frac{3}{5}$. It is natural to choose n such that r_g is equal to the correlation length ζ given by (12.2.16), i.e.

$$b\left(\frac{L}{n}\right)^\nu = \zeta \approx bL^\nu \left(\frac{\rho_m}{\rho_m^o}\right)^{-\nu/(3\nu-1)} \tag{12.2.23}$$

which shows that

$$n \approx \left(\frac{\rho_m}{\rho_m^o}\right)^{1/(3\nu-1)} \approx \left(\frac{\rho}{\rho^o}\right)^{5/4} \tag{12.2.24}$$

If n is chosen to be at least as large as that given by this expression, the blob density $\rho_b = n\rho$ remains at or below the blob overlap density $\rho_b^o = 3/4\pi r_g^3$, corresponding to the dilute blob regime, even though the polymer density may be greater than ρ^o. In that situation we may assume that the effective interaction between blobs, $v_{bb}(r)$, is well approximated by its low-density limit. It is also

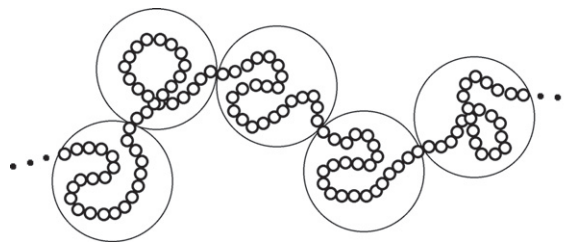

FIGURE 12.3 A multi-blob representation of part of a linear polymer.

reasonable to assume that the potential between non-bonded blobs is identical for all pairs, whether on the same or different polymers, and given by the gaussian form (12.2.9) but with R_g replaced by r_g, i.e.

$$v_{bb}(r) = A_{bb} \exp\left[-\beta\alpha_{bb}(r/r_g)^2\right] \tag{12.2.25}$$

where A_{bb} and α_{bb} each has approximately the same value as the corresponding quantity in (12.2.9). The effective potential between bonded blobs can then be written as the superposition of $v_{bb}(r)$ and a tethering, harmonic spring potential $\phi(r)$ that acts between blobs, similar to the entropic spring of an ideal, gaussian chain, described in Appendix G:

$$\phi(r) = \frac{1}{2}k(r - r_0)^2 \tag{12.2.26}$$

The potential parameters k and r_0 are determined by measurement of the intramolecular distribution function $P(r)$ of the distance r between the centres of mass of the two blobs in a simulation of a single dimer of SAW polymers, from which the potential is obtained via the relation

$$\phi(r) = -k_B T \ln P(r) \tag{12.2.27}$$

The total potential energy of the two polymers is then

$$V_2(\{\mathbf{r}_{1\alpha}\},\{\mathbf{r}_{2\beta}\}) = \sum_{i=1}^{2}\sum_{\alpha=1}^{n-1}\phi(|\mathbf{r}_{i,\alpha+1} - \mathbf{r}_{i,\alpha}|) + \sum_{i=1}^{2}\sum_{\alpha=1}^{n-1}\sum_{\beta=\alpha+1}^{n} v_{bb}(|\mathbf{r}_{i\beta} - \mathbf{r}_{i\alpha}|) + \sum_{\alpha=1}^{n}\sum_{\beta=1}^{n} v_{bb}(|\mathbf{r}_{2\beta} - \mathbf{r}_{1\alpha}|) \tag{12.2.28}$$

where $\mathbf{r}_{i\alpha}$ now represents the coordinates of the centre of mass of blob α on polymer i. The three terms on the right-hand side represent, successively, the potential energies due to tethering and those due to interaction between blobs on the same or different polymers.

As examples of the use of the multi-blob representation we show first how a tractable expression can be obtained for the static structure factor.[21] The structure factor of a system of N chains, each composed of n blobs, is

$$S(k) = \frac{1}{Nn}\langle\rho_{\mathbf{k}}\rho_{-\mathbf{k}}\rangle = \hat{\omega}(k) + \frac{1}{n}\sum_{\alpha}\sum_{\beta} s_{\alpha\beta}(k) \tag{12.2.29}$$

where $\rho_{\mathbf{k}}$ is a Fourier component of the monomer density, $\hat{\omega}(k)$ is the form factor (G.6) of a single polymer and $s_{\alpha\beta}(k)$ is the partial, intermolecular structure factor for blobs α and β. By anticipating the results of PRISM theory, described in Section 12.3, we may assume that all $s_{\alpha\beta}(k)$ are identical and equal to a unique blob–blob structure factor $s(k)$, which in turn is related to a blob–blob direct correlation function $\hat{c}(k)$ and the form factor by a generalised Ornstein–Zernike

relation. This leads to the PRISM expression for $S(k)$:

$$S(k) = \frac{\hat{\omega}(k)}{1 - \rho_{\rm b}\hat{\omega}(k)\hat{c}(k)} \tag{12.2.30}$$

Within the RPA (3.5.17), $\hat{c}(k) = -\beta\hat{v}_{\rm bb}(k)$ and substitution of the Fourier transform of (12.2.25) in (12.2.30) shows that

$$S_{\rm RPA}(k) = \frac{\hat{\omega}(k)}{1 + \rho_{\rm b} r_{\rm g}^3 \hat{\omega}(k) A_{\rm bb}(\pi/\alpha_{\rm bb})^{3/2} \exp\left(-k^2 r_{\rm g}^2/4\alpha_{\rm bb}\right)} \tag{12.2.31}$$

which is a generalisation to the multi-blob model of the classic RPA expression for the structure factor of a polymer solution.[22] Use of (3.6.11) and the fact that $\hat{\omega}(k=0) = n$, together with substitution for n from (12.2.24), leads to an expression for the osmotic compressibility:

$$\rho k_{\rm B} T \chi_T = \frac{1}{1 + c(\rho/\rho^{\rm o})^{1/(3\nu-1)}} \tag{12.2.32}$$

with $c = 3A_{\rm bb}(\pi/\alpha_{\rm bb})^{3/2}/4\pi \approx 3.23$. For $\rho \gg \rho^{\rm o}$, (12.2.32) leads back to the des Cloizeaux scaling law (12.2.19) in the form

$$\frac{\beta\Pi^{\rm ex}}{\rho^{\rm o}} = \frac{3\nu - 1}{3\nu} c \left(\frac{\rho}{\rho^{\rm o}}\right)^{3\nu/(3\nu-1)} \tag{12.2.33}$$

The RPA therefore yields an expression for the prefactor, which the scaling argument does not.

As a second example, advantage can be taken of the weakness of the effective blob–blob potential and its gaussian form in a way that allows the use of perturbation theory to calculate the free energy F_N of a system of N interacting n-blob polymers.[21] The reference system is chosen to be the solution of N non-interacting gaussian chains of length n and spring constant $k_0 = 3k_{\rm B}T/b'^2$, where the bond length b' is used as as a variational parameter in minimising the right-hand side of the Gibbs–Bogoliubov inequality (5.2.27):

$$F_N \leq F_N^{(0)} + \left\langle V_N - V_N^{(0)} \right\rangle_0 \tag{12.2.34}$$

where V_N is the total potential energy of the N interacting polymers, $V_N^{(0)}$ is the corresponding energy of N gaussian coils, obtained from (G.3), and the average is taken with gaussian statistics. The two terms on the right-hand side can be calculated analytically as functions of b'; their sum is then minimised with respect to the reduced bond length $b_0 = b'/r_{\rm g}$ to provide the best variational estimate of the radius of gyration of the interacting polymers relative to that of the reference, gaussian chain, given by (G.5). The result is

$$R_{\rm g} = \frac{n^{1/2} b_0 r_{\rm g}}{\sqrt{6}} \approx \frac{n^{1/2} b_0}{\sqrt{6}} b \left(\frac{L}{n}\right)^{\nu} \tag{12.2.35}$$

or, after substitution for n from (12.2.24) and setting $\nu = \frac{3}{5}$:

$$R_g \approx bL^{\nu}\left(\frac{\rho}{\rho^o}\right)^{-(2\nu-1)/2(3\nu-1)} \approx R_{g0}\left(\frac{\rho}{\rho^o}\right)^{-1/8} \tag{12.2.36}$$

where $R_{g0} \approx bL^{\nu}$ is the radius of gyration of an isolated SAW polymer. The optimum value of the dimensionless variational parameter b_0 is found to increase with the number of blobs and saturates at a value $b_0 \approx 2.24$. The result in (12.2.36) agrees with the prediction of a scaling argument similar to the one that leads to (12.2.17); it shows that the radius of gyration of interacting polymers in a semi-dilute solution slowly contracts as ρ/ρ^o increases.

Use of the multi-blob representation in the examples discussed hinges on the assumption of transferability implied in the use for any value of n of effective pair potentials derived in the low-density limit. Since intramolecular interactions beyond the two-body level are neglected, the effective pair potentials cannot account quantitatively for intramolecular correlations, nor for thermodynamic properties at finite concentrations. Improvements have been proposed that include the use of effective bending and torsion angle potentials[23] or blobs of fluctuating size.[24] Multi-blob calculations have also been made for AB diblock copolymers in which different effective and tethering potentials are used for AA, AB and BB pairs. The differences in solvent-induced potentials lead to self-assembly and phase separation into ordered or disordered micellar, cylindrical, lamellar or bicontinuous phases, reminiscent of the phase behaviour of ampiphilic molecules in water or oil.[25a] This complex phase behaviour has been reproduced, at least qualitatively, by Monte Carlo simulations.[25b]

12.3 POLYMER MELTS

Polymer melts are solvent-free, viscoelastic liquids consisting of entangled macromolecules with a monomer volume fraction $\eta_m = \pi\rho_m b^3/6$ comparable with that of simple liquids. The large volume fraction means that monomer concentration fluctuations are strongly suppressed and the liquid is highly incompressible. The identity of the polymer to which a given monomer belongs is therefore largely irrelevant; the spatial constraints associated with high packing fraction dominate those due to connectivity. In other words, a polymer behaves, in a first approximation, like a liquid of disconnected monomers, at least as regards its structure and thermodynamics. Entanglement of the chains does play a major role in determining the dynamics of the melt,[6c] but we confine ourselves here to the discussion of static properties.

In the multi-blob representation of semi-dilute solutions described in the previous section we see from (12.2.24) that the number of blobs required to ensure the no-overlap condition increases with monomer concentration. This trend carries over to the melt, where $n \to M$. Each blob now corresponds to a single monomer, and the effective interaction between blobs is the microscopic,

excluded volume interaction that acts between monomers under good solvent conditions. On the other hand, if $n \approx M$, if follows from (12.2.35) that in the melt the radius of gyration of a linear polymer should scale as $bL^{1/2}$, as it does for an ideal chain. This surprising result was first noted by Flory, who conjectured that the conformations of individual polymer chains in a melt should follow gaussian statistics, as do ideal chains or interacting polymers in θ-solvent. No proof has been given of Flory's hypothesis but theoretical arguments have been forward that support it. At the simplest level, for example, the local monomer density $\rho_{\mathrm{m}}(\mathbf{r})$ will be constant throughout the melt if spatial fluctuations can be ignored. Hence the local potential energy $u(\mathbf{r})$ will also be constant and the force $-\nabla u(\mathbf{r})$ acting on a monomer located at $\mathbf{r}$ therefore vanishes. Thus the polymer behaves like an ideal chain of non-interacting monomers. The repulsive interactions between monomers along a given chain, which would lead to a swelling of the polymer if it were isolated, are now screened by the monomers of neighbouring chains.[26]

The screening mechanism can be quantified by an RPA calculation[27] in which the excluded volume interaction between monomers is modelled by a contact potential:

$$v(\mathbf{r}_{j\beta} - \mathbf{r}_{i\alpha}) = v_{\mathrm{x}} k_{\mathrm{B}} T \delta(\mathbf{r}_{j\beta} - \mathbf{r}_{i\alpha}) \tag{12.3.1}$$

where the excluded volume parameter $v_{\mathrm{x}} \approx b^3$. If the reference system is taken as one consisting of non-interacting gaussian chains, the RPA expression (5.6.24) for the structure factor may be written as

$$S(k) = \frac{S_0(k)}{1 + \rho_{\mathrm{m}} \beta \hat{v}(k) S_0(k)} = \frac{S_0(k)}{1 + \rho_{\mathrm{m}} v_{\mathrm{x}} S_0(k)} \tag{12.3.2}$$

where $S_0(k) = \hat{\omega}(k)$, defined by (G.7), is the structure factor of the reference system. If the Lorentzian approximation in (G.8) is used for $\hat{\omega}(k)$, with $R_{\mathrm{g}}^2 = Mb^2/6$, we find that

$$S(k) = \frac{12}{b^2} \frac{1}{k^2 + \zeta^{-2}} \tag{12.3.3}$$

The quantity ζ is a correlation length defined as

$$\zeta^2 = \frac{Mb^2}{12(1 + M\rho_{\mathrm{m}} v_{\mathrm{x}})} \approx \frac{b^2}{12\rho_{\mathrm{m}} v_{\mathrm{x}}} \tag{12.3.4}$$

where the approximation used is justified when $M \gg 1$. Equation (12.3.3) resembles the expression (5.7.22) for the structure factor of a fluid close to the critical point. The corresponding monomer–monomer pair correlation function is therefore of the same form as (5.7.23):

$$h(r) = \frac{3}{\pi \rho_{\mathrm{m}} b^2} \frac{\exp(-r/\zeta)}{r} \tag{12.3.5}$$

We now show that ζ plays the role of a screening length associated with the screening mechanism invoked earlier. Linear response theory can be used to

determine the induced modulation $\delta\rho_{\rm m}(r)$ of the monomer concentration and the corresponding potential energy profile $u(r)$ at a distance r from a monomer placed at the origin. According to (3.6.9):

$$\delta\hat{\rho}_{\rm m}(k) = -\beta\rho_{\rm m}\hat{v}(k)S(k) = -\rho_{\rm m}v_{\rm x}S(k) \tag{12.3.6}$$

On combining this result with (3.6.10) and (12.3.5) we find that in real space

$$\delta\rho_{\rm m}(r) = \rho_{\rm m}(r) - \rho_{\rm m} = -\frac{3\rho_{\rm m}v_{\rm x}}{\pi b^2}\frac{\exp(-r/\zeta)}{r} \tag{12.3.7}$$

and hence that

$$\begin{aligned} u(r) &= v(r) + \int v(\mathbf{r}' - \mathbf{r})\delta\rho_{\rm m}(r')\mathrm{d}\mathbf{r}' \\ &= k_{\rm B}Tv_{\rm x}\left(\delta(\mathbf{r}) - \frac{\exp(-r/\zeta)}{4\pi\zeta^2 r}\right) \end{aligned} \tag{12.3.8}$$

where the first term on the right-hand side is the contribution to the local potential energy from the monomer at the origin and the second is that generated by modulation of the surrounding monomer density. The quantity $u(r)$ may be treated as the effective pair potential between the central monomer and a neighbouring monomer at a distance r from the origin; this accounts for the presence of other monomers located between the two, which reduces the bare potential. In fact integration of $u(r)$ over all space yields zero, meaning that the attraction induced by intermediate monomers exactly cancels the direct interaction for distances larger than ζ; the situation is identical to that of polymer coils in solution under θ-point conditions. Thus the individual coils in melts behave like non-interacting polymers, obeying gaussian statistics with $R_{\rm g} \sim L^{1/2}$ on length scales greater than ζ.

Equation (12.3.8) is reminiscent of the screened Coulomb interaction in ionic systems, as represented by (4.6.27), with the correlation length playing the role of the Debye screening length; both quantities decrease as the number concentration increases. In a dense melt, $\rho_{\rm m}v_{\rm x} \approx 1$, and polymers behave like ideal chains on all length scales. The derivation that leads to (12.3.8) also applies to concentrated solutions of overlapping polymers, but in that case $\rho_{\rm m}v_{\rm x} \ll 1$ and hence $\zeta \gg b$. Non-ideal behaviour, characterised by a swollen radius of gyration, $R_{\rm g} \sim L^{\nu}$ with $\nu \approx \frac{3}{5}$, prevails over length scales r such that $b < r < \zeta$.

It is possible is to formulate an accurate theory of the monomer–monomer pair structure that exploits Flory's hypothesis but goes beyond the RPA result given by (12.2.31); the RPA does not account properly for short-range correlations and (12.2.31) is therefore valid only for small wavenumbers. Each monomer may instead be regarded as an interaction site on a polymer chain so that a system of polymers can be treated within the RISM formalism of Section 11.8. The difference here is the fact that when $M \gg 1$, the matrices $\hat{\mathbf{h}}$, $\hat{\mathbf{c}}$ and $\hat{\mathbf{w}}$ are very large. The application to polymers, known as PRISM,[28] is based on the assumption that all monomers are geometrically equivalent and

that the pair functions $h_{\alpha\beta}(r)$ and $c_{\alpha\beta}(r)$ are therefore the same for all α, β. The $M \times M$ RISM-OZ relation (11.8.6) then reduces to a single scalar equation

$$\hat{h}(k) = \hat{\omega}(k)\hat{c}(k)\hat{\omega}(k) + \rho_{\mathrm{m}}\hat{\omega}(k)\hat{c}(k)\hat{h}(k) \tag{12.3.9}$$

where

$$\hat{\omega}(k) = \frac{1}{M}\sum_{\alpha}\sum_{\beta}\left\langle \hat{\omega}_{\alpha\beta}(k)\right\rangle \tag{12.3.10}$$

is the form factor (G.7) of the single polymer. For the rigid molecules discussed in Section 11.8 the quantities $\hat{\omega}_{\alpha\beta}$ depend only on fixed intramolecular bond lengths, but here they must be averaged over macromolecular conformations, as indicated in (12.3.10). The basic assumption underlying the PRISM equation (12.3.9), namely the equivalence of all monomers, is true for ring polymers and for linear polymers if end effects can be ignored. Equation (12.3.9) is easily generalised, in matrix form, to multi-component melts, such as binary mixtures of homopolymers or block copolymer systems, in which monomers of two or more different chemical species are present.[29]

When combined with a suitable closure relation, such as PY, HNC or a molecular closure better adapted to multi-site systems,[30] the PRISM-OZ relation (12.3.9) can be solved numerically to yield the monomer–monomer pair correlation function $h_{mm}(r)$. All that is required is an expression for the form factor $\hat{\omega}(k)$, one possible choice of which is the Debye function (G.7), corresponding to a gaussian chain. The static structure factor of the melt, as measured by diffraction experiments, is given by a generalisation of (3.6.10) in which the monomers now take the role of atoms:

$$S(k) = \hat{\omega}(k) + \rho_{\mathrm{m}}\hat{h}(k) = \frac{\hat{\omega}(k)}{1 - \rho_{\mathrm{m}}\hat{\omega}(k)\hat{c}(k)} \tag{12.3.11}$$

The isothermal compressibility follows from (11.3.6):

$$\rho k_{\mathrm{B}} T \chi_T = 1 + \rho\hat{h}(k=0) = \frac{S(k=0)}{M} \tag{12.3.12}$$

where $\rho = \rho_{\mathrm{m}}/M$ is the polymer density. An example of the agreement achievable between theory and experiment is illustrated by Figure 12.4, which shows a comparison between the results of molecular dynamics calculations and the predictions of PRISM for a system of Lennard-Jones chains consisting of 200 monomers. The form factor used is the one computed in the simulation, a procedure designed to test the internal consistency of the theory.[28b]

A different application of PRISM leads to an accurate relation between the monomer and centre-of-mass pair correlation functions in both polymer solutions and melts,[31] as already referred to in Section 12.2. The key idea is to consider the centre of mass of each polymer i as an additional, auxiliary site $\mathbf{R}_i$, linked to the monomer coordinates $\mathbf{r}_{i\alpha}$ by the constraint that

$$\mathbf{R}_i = \frac{1}{M}\sum_{\alpha=1}^{M}\mathbf{r}_{i\alpha} \tag{12.3.13}$$

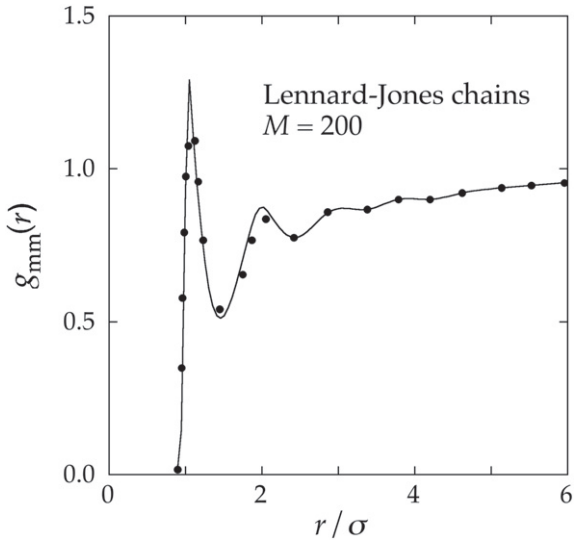

FIGURE 12.4 Monomer–monomer radial distribution function for a system of Lennard-Jones chains with $M = 200$ at a reduced temperature $T^* = 1.0$ and $\rho_m \sigma^3 = 0.85$. The points are the results of molecular dynamics calculations and the curve is calculated from the PRISM equation with a form factor computed in the simulation. *Redrawn with permission from Ref. 28(b) © 1989 American Institute of Physics.*

Since the auxiliary site does not interact with the monomers, it must be treated separately. Thus each polymer contains two types of site, the single, auxiliary one, labelled x, and the M equivalent, interaction sites associated with the monomers, labelled m. The three relevant form factors are then $\hat{\omega}_{mm}(k)$, $\hat{\omega}_{mx}(k)$ and $\hat{\omega}_{xx}(k)$, of which $\hat{\omega}_{xx} = 1$ and

$$\begin{aligned}\hat{\omega}_{mx}(k) &= \left\langle \sum_{\alpha} \exp\left[i\mathbf{k}\cdot(\mathbf{r}_{i\alpha} - \mathbf{R}_i)\right] \right\rangle \\ &\approx \frac{\sqrt{\pi M}}{kR_g} \exp\left(-k^2 R_g^2\right) \mathrm{erf}\left(\frac{1}{2} k R_g\right) \end{aligned} \tag{12.3.14}$$

where the second line holds for gaussian statistics.

The single PRISM-OZ relation (12.3.9) is now replaced by a 2×2 matrix of relations, one of which is identical to (12.3.9) but with an mm subscript for all pair functions. The other three can be simplified by assuming that the direct correlation functions between auxiliary sites and between the auxiliary site in one polymer and the monomers of another are all identically zero since there is no physical interaction involved, i.e.

$$\hat{c}_{xx}(k) \equiv 0; \quad \hat{c}_{mx}(k) = \hat{c}_{xm}(k) \equiv 0 \tag{12.3.15}$$

What remains is

$$\hat{h}_{mx}(k) = \hat{\omega}_{mx}(k)\hat{c}_{mm}(k)\big[\hat{\omega}_{mm}(k) + \rho_{\mathrm{m}}\hat{h}_{mm}(k)\big]$$
$$\hat{h}_{xx}(k) = \hat{\omega}_{mx}(k)\hat{c}_{mm}(k)\big[\hat{\omega}_{mx}(k) + \rho_{\mathrm{m}}\hat{h}_{mx}(k)\big] \qquad (12.3.16)$$

Combination of (12.3.9) and (12.3.16) leads immediately to the desired result:

$$\hat{h}_{xx}(k) = \frac{\hat{\omega}^2_{mx}(k)}{\hat{\omega}^2_{mm}(k)}\hat{h}_{mm}(k) \qquad (12.3.17)$$

which, apart from the assumption (12.3.15), is independent of the choice of closure relation. To extract $\hat{h}_{xx}(k)$ from $\hat{h}_{mm}(k)$ requires a knowledge of the two form factors involved, which are available analytically for gaussian chains. Equation (12.3.17) is therefore directly applicable in the melt regime. It has also been successfully applied to coarse-grained multi-blob representations of polymer melts[32] similar to that adopted for semi-dilute solutions in Section 12.2. In that case the greater importance of concentration fluctuations and the consequent swelling of individual coils means that the ratio $\hat{\omega}^2_{mx}(k)/\hat{\omega}^2_{mm}(k)$ deviates significantly from its ideal form.

12.4 COLLOIDAL DISPERSIONS

Colloidal dispersions are highly asymmetric systems of mesoscopic particles suspended in a molecular solvent, with particle sizes typically in the range from 10 to 10^3 nm. They include polymer latex dispersions (in paints), casein micelles (in dairy products), oil-in-water emulsions and clays. Colloidal systems have an enormous range of applications, from the oil industry (drilling fluids) to the manufacture of cosmetics, food and pharmaceutical products.[33] This section is concerned with the relatively simple case of spherical, solid particles such as mineral silica or synthetic PMMA spheres. These are systems that have been much studied experimentally, in particular by photon correlation spectroscopy; visible light is well adapted to probe the structure and dynamics of micron-sized colloids, since the wavelength of the radiation is comparable with the dimensions of the particles. One complication that arises with colloidal systems, but not with atomic or molecular liquids, is that of size polydispersity. Even for carefully prepared samples the diameters of the particles may have a spread of 5–10%, but in theoretical work it is usually assumed that the system is monodisperse.

Colloidal particles are composed of very large numbers of atoms, roughly of order 10^6–10^{12}. A straightforward calculation[34] shows that summing the dispersion interactions ($\sim -C/r^6$) between pairs of atoms contained in two spheres of diameter d and centre-to-centre separation R leads to an attractive potential between spheres of the form

$$w(R) = -\frac{A}{12}h(x) \qquad (12.4.1)$$

where $A = \pi^2 C \rho^2$ is the Hamaker constant; ρ is the number density of atoms within each sphere, $x = R/d$ and

$$h(x) = \frac{1}{x^2 - 1} + \frac{1}{x^2} + 2\ln\left(1 - \frac{1}{x^2}\right) \tag{12.4.2}$$

with

$$\begin{aligned} h(x) &\approx \frac{1}{3x^6}, \qquad x \gg 1 \\ &\approx \frac{1}{2(x-1)}, \quad x \approx 1 \end{aligned}$$

The Hamaker constant is typically of order $10 k_B T$ at room temperature and the potential diverges as contact is approached ($x \to 1^+$). Such a strong, attractive interaction would lead to irreversible aggregation or *flocculation* unless balanced by a strong repulsive force. A dispersion can be stabilised against flocculation either by grafting polymers onto the surface of the colloidal particles or by formation of electric double layers around the particles, which acquire a surface charge in strongly polar solvents. *Charge stabilisation* is discussed in the following section; here we consider only *steric stabilisation* by grafted polymers.

Consider first a polymer 'brush' of identical polymer chains end-grafted onto a planar substrate, as pictured in Figure 12.5a. If σ is the surface grafting density, the mean distance between adjacent grafting sites will be $D \approx \sigma^{-1/2}$. If D is smaller than the radius of gyration of the polymer, then in good solvent the repulsion between monomers will cause the polymer to stretch in the direction normal to the substrate. The mean height h of the brush can be estimated by a simple scaling argument[35] based on the blob picture of Figure 12.5a. Let us suppose that the blob size is set equal to the correlation length ζ appropriate

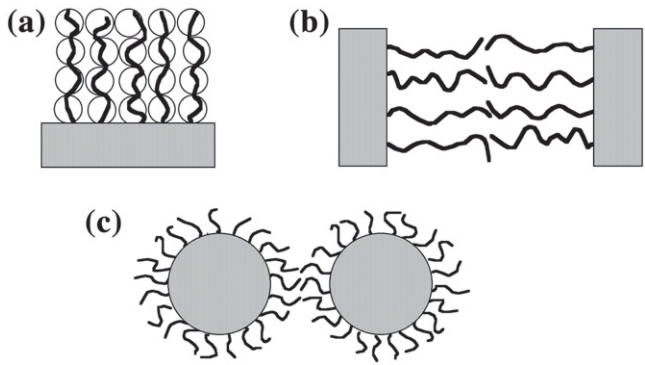

FIGURE 12.5 Steric stabilisation of colloid dispersions by grafted polymers. (a) A single polymer brush and its multi-blob representation. (b) Two polymer brushes repel each other when brought into contact. (c) Two colloidal particles stabilised by repulsion between their polymer layers.

to the semi-dilute regime, introduced in (12.2.17). Then, by taking $\zeta = D$, we ensure that blobs will not, on average, overlap. The number of monomers per blob is $\ell \approx (\zeta/b)^{1/\nu}$, where $\nu \approx \frac{3}{5}$. If Lb is the length of a chain, it follows that

$$h = \frac{L\zeta}{\ell} = \frac{L\zeta}{(\zeta/b)^{1/\nu}} = Lb(\sigma b^2)^{(1-\nu)/2\nu} \approx Lb(\sigma b^2)^{1/3} \tag{12.4.3}$$

Thus the stretching of the polymers increases with grafting density, as one would expect, and maximum stretching is achieved in the limit $\sigma = b^{-1/2}$, when the monomers of neighbouring chains come into contact; the same result can be derived by a free energy minimisation of the type that leads to Flory's estimate of the exponent ν (see Appendix G). These simple arguments imply that the monomer density profile is a step function:

$$\begin{aligned} \rho_{\mathrm{m}}(z) &= \frac{\sigma L}{h}, \quad z < h \\ &= 0, \qquad z > h \end{aligned} \tag{12.4.4}$$

which is strictly true only at $D = b$. For moderate grafting densities the monomer density as a function of distance z above the surface has been determined by a self-consistent calculation which relates the density to a mean field expression for the local chemical potential of the monomers[36]; the resulting profile turns out to be parabolic. The same result can be obtained by the simpler, density functional argument sketched in Appendix H. Monte Carlo calculations[37] of SAW polymer brushes show that a rapid transition from a partly stretched, parabolic profile to a fully stretched, near-rectangular profile similar to (12.4.4) occurs at a reduced grafting density $\sigma R_{\mathrm{g}}^2 \approx 25$.

Now consider the more complicated case of two parallel polymer brushes facing each other, illustrated in Figure 12.5b. As the distance z between the two substrates is reduced, the polymer brushes are compressed when $z < 2h$; the resulting decrease in entropy gives rise to an effective repulsion between the brushes. The force per unit area acting on each substrate is the *disjoining pressure*, i.e. the osmotic pressure of the grafted polymers, given by (12.2.19).[38] The correlation length ζ is given by (12.2.16), while for $z < 2h$ the mean monomer density between substrates is $\rho_{\mathrm{m}} = \sigma L/z$. Thus $\zeta \approx b(\sigma Lb^3/z)^{-\nu(3\nu-1)}$ and

$$\beta \Pi b^3 \approx \left(\frac{\sigma Lb^3}{z}\right)^{3\nu/(3\nu-1)} \approx \left(\frac{\sigma Lb^3}{z}\right)^{9/4} \tag{12.4.5}$$

The disjoining pressure increases with grafting density and polymer length and diverges as $z \to 0$; it is this strong repulsion which provides the mechanism for steric stabilisation.

Colloidal particles carrying a dense, grafted layer of short polymers, such as those pictured schematically in Figure 12.5c, are essentially hard-sphere-like

in their behaviour. By observing a dense suspension of slowly sedimenting, sterically stabilised PMMA particles in a mixture of decalin and carbon disulphide, Pusey and van Megen[39] were able to locate the freezing transition from a dense colloidal fluid to an opalescent crystal that diffracts visible light; the measured coexistence densities lay within roughly 1% of the values provided by simulations of hard-sphere systems. Also observed was a transition to an amorphous solid phase at $\eta \approx 0.59$, a density lying well below that of random close packing. The existence of such a phase could be explained by a small degree of size polydispersity in the sample and it is now recognised that polydispersity is not merely an unwanted complication but a variable of interest in its own right. An extension to a polydisperse, hard-sphere system of the density functional theory of freezing of Section 6.6 has shown that beyond a critical polydispersity crystallisation is inhibited in favour of transition to a high density, disordered state,[40] while specialised Monte Carlo simulations[41] have identified qualitative differences between the phase behaviour of monodisperse and polydisperse systems.

Studies of sedimentation equilibria of colloidal dispersions provide a direct, experimental route to the determination of the osmotic equation of state over a wide range of density. Optical techniques may be used to measure the density profile $\rho(z)$ of an equilibrated suspension of charged colloidal particles in a gravitational field or an ultracentrifuge, from which the osmotic pressure can be derived as a function of density. In the first case the external potential is

$$\beta\phi(z) = \frac{mg}{k_{\mathrm{B}}T}z = \alpha z \tag{12.4.6}$$

where g is the acceleration due to gravity and $m = M - 4\pi R^3 d_{\mathrm{m}}/3$ is the buoyant mass, with M and R being the mass and radius of the particles and d_{m} the mass density of the suspending fluid; α is the inverse gravitational length. By adjusting d_{m} to be close to the mass density of the colloidal particles, α can be made sufficiently small to ensure that the potential varies very slowly with z. Under those conditions the free energy functional $\mathcal{F}[\rho(z)]$ may be replaced by its local density approximation (6.2.5). This leads to the condition for mechanical equilibrium given by (6.2.7), which here takes the form

$$\frac{\mathrm{d}\Pi(z)}{\mathrm{d}z} = -mg\rho(z) \tag{12.4.7}$$

This is easily integrated to give

$$\beta\Pi(z) - \beta\Pi(z=0) = \beta\Pi(z) - \alpha n_s - \alpha\int_0^z \rho(z')\mathrm{d}z' \tag{12.4.8}$$

where

$$n_s = \int_0^\infty \rho(z)\mathrm{d}z \tag{12.4.9}$$

is the number of colloids per unit area at $z = 0$. A single measurement of the equilibrium density profile is therefore sufficient[42] to determine the equation of state as a function of the overall number density by elimination of z between

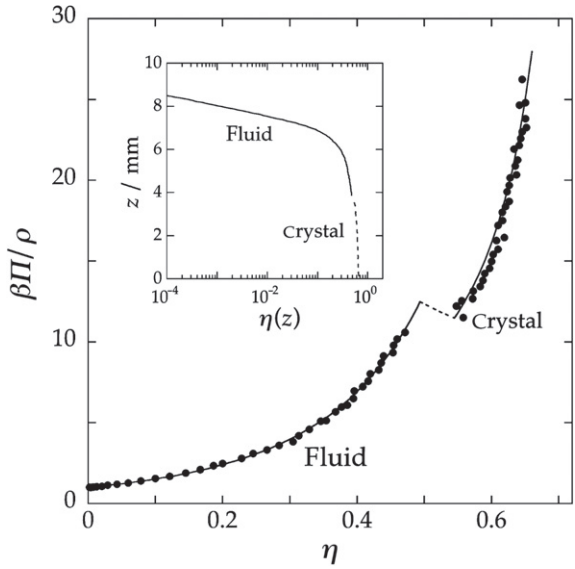

FIGURE 12.6 The main figure shows the osmotic equation of state as a function of the hard-sphere packing fraction for a sterically stabilised colloidal dispersion. The points are experimental results and the curves are calculated from the Carnahan–Starling equation (fluid branch) or an empirical equation of state[44] (solid branch). The broken line links the values obtained by simulation for the packing fractions of the two phases at coexistence. The inset shows the packing fraction profile from which the equation of state is deduced; see text for details. *Redrawn with permission from Ref. 43* © *2007 American Physical Society.*

$\rho(z)$ and $\Pi(z)$. Figure 12.6 shows the results of such an experiment[43] on an aqueous suspension of spherical, colloidal particles (a fluorinated polymer), sterically stabilised by addition of surfactant. The particles again behave, to a very good approximation, as hard spheres. There is excellent agreement with both the Carnahan–Starling equation in the fluid phase and an empirical equation of state[44] in the solid phase, with the fluid–solid transition occurring very close to that expected from computer simulations of hard-sphere systems.

The argument leading to (12.4.8) holds for colloidal particles much larger than those of the solvent; in that case it is justified to employ an expression for the buoyant mass which derives from Archimedes' principle. When that condition is not met, subtle effects due to the depletion forces discussed in the next section come into play, the solvent can no longer be treated as a continuum, and a generalised form of Archimedes' principle must be employed.[45]

12.5 COLLOID–POLYMER MIXTURES

In the previous section it was shown how grafted polymers can stabilise colloidal dispersions against flocculation. By contrast, free, non-adsorbing polymers may destabilise homogeneous colloidal suspensions by driving a separation into

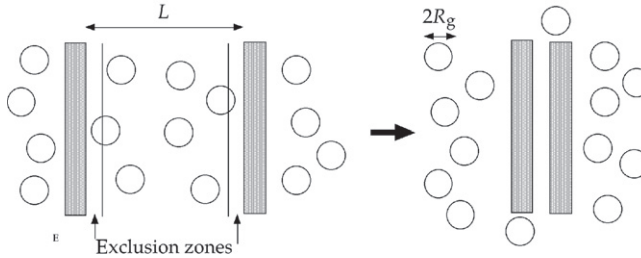

FIGURE 12.7 Exclusion zones at the surfaces of two plates immersed in a a polymer solution. When the distance between the plates is reduced to a value at which the exclusion zones overlap, the polymers initially found between the plates are expelled, leading to an imbalance in osmotic pressure.

concentrated (or 'liquid') and dilute (or 'gas') colloid phases. Phase separation arises from a polymer *depletion* effect, which is of essentially entropic origin.[33] The physical basis of the effect is easily understood by considering the very simple case of two parallel plates immersed in a solution of non-interacting polymers, as shown in Figure 12.7. The polymers are free to interpenetrate but their centres cannot approach the plates within a distance equal to their radius of gyration; this leads to the polymer exclusion zones represented in the figure. When the separation L of the plates is less than $2R_g$ the two exclusion zones overlap and the polymer coils are expelled. This creates an osmotic pressure imbalance which represents an attractive force per unit area between the plates equal to the decrease in pressure, given by van't Hoff's equation:

$$\Delta\Pi = -\rho k_B T \Theta(L - 2R_g) \tag{12.5.1}$$

where ρ is the bulk polymer density and $\Theta(x)$ is the Heaviside step function. The force is the (negative) derivative of an effective depletion potential given by

$$V^{\text{eff}}(L) = -\rho k_B T (2R_g - L)\Theta(L - 2R_g) \tag{12.5.2}$$

Both force and potential vanish when $L > 2R_g$. The depletion attraction can also be understood in terms of a gain in total volume accessible to the polymers, and hence an increase in their entropy, when the exclusion zones around the plates overlap. The increase in entropy, and hence the decrease in free energy or grand potential when $L < 2R_g$ lead to the effective attraction between the two plates.

These simple arguments can be formalised within the general framework of the coarse-graining strategy described in Section 12.1. Consider a dispersion of N_C spherical, colloidal particles of radius R_0 in a solution of polymer coils of fluctuating number N_P in osmotic equilibrium with a pure solution of polymers which serves as a reservoir and fixes the chemical potential μ of the polymers. The system can be described within the semi-grand canonical ensemble (rather than the canonical ensemble for a binary mixture considered in Section 12.1), characterised by the variables N_C, V (the total volume of the suspension), T,

and μ. Let $V_{\mathrm{CC}}(\{\mathbf{R}_i\})$, $V_{\mathrm{PP}}(\{\mathbf{r}_j\})$ and $V_{\mathrm{CP}}(\{\mathbf{R}_i\},\{\mathbf{r}_j\})$ be the contributions to the total potential energy from colloid–colloid, polymer–polymer and colloid–polymer interactions. Then the semi-grand partition function may be written as a generalisation of (2.4.6):

$$\Xi(V,T,N_{\mathrm{C}},\mu)=\frac{1}{N_{\mathrm{C}}!\Lambda_{\mathrm{C}}^{3N_{\mathrm{C}}}}\sum_{N_{\mathrm{P}}=0}^{\infty}\frac{z^{N_{\mathrm{P}}}}{N_{\mathrm{P}}!}Z(V,T,N_{\mathrm{C}},N_{\mathrm{P}}) \tag{12.5.3}$$

where Λ_{C} is the de Broglie thermal wavelength of the colloidal particles, $z=\exp(\beta\mu/\Lambda_{\mathrm{P}}^3)$ is the activity of the polymers (Λ_{P} being the thermal wavelength associated with their centre-of-mass motion) and Z is the configuration integral:

$$Z(V,T,N_{\mathrm{C}},\mu)=\int\exp\big[-\beta(V_{\mathrm{CC}}(\{\mathbf{R}_i\})+V_{\mathrm{PP}}(\{\mathbf{r}_j\})+V_{\mathrm{CP}}(\{\mathbf{R}_i\},\{\mathbf{r}_j\})\big]\mathrm{d}\mathbf{R}^{N_{\mathrm{C}}}\,\mathrm{d}\mathbf{r}^{N_{\mathrm{P}}} \tag{12.5.4}$$

The grand partition function of the system of polymers for a given configuration $\{\mathbf{R}_i\}$ of the colloids is

$$\Xi_{\mathrm{P}}(V,T,\mu;\{\mathbf{R}_i\})=\sum_{N_{\mathrm{P}}=0}^{\infty}\frac{z^{N_{\mathrm{P}}}}{N_{\mathrm{P}}!}\int\exp\big(-\beta\big[V_{\mathrm{PP}}(\{\mathbf{r}_j\})+V_{\mathrm{CP}}\big(\{\mathbf{R}_i\},\{\mathbf{r}_j\}\big)\big]\big)\mathrm{d}\mathbf{r}^{N_{\mathrm{P}}} \tag{12.5.5}$$

and the polymer grand potential is

$$\Omega_{\mathrm{P}}(V,T,\mu;\{\mathbf{R}_i\})=-k_{\mathrm{B}}T\ln\Xi_{\mathrm{P}}(V,T,\mu;\{\mathbf{R}_i\}) \tag{12.5.6}$$

Combination of (12.5.3)–(12.5.6) yields an expression for the semi-grand partition function:

$$\Xi(V,T,N_{\mathrm{C}},\mu)=\frac{1}{N_{\mathrm{C}}!\Lambda^{3N_{\mathrm{C}}}}\int\exp\big(-\beta\big[V_{\mathrm{CC}}(\{\mathbf{R_i}\})+\Omega_{\mathrm{P}}(V,T,\mu;\{\mathbf{R}_i\})\big]\big)\mathrm{d}\mathbf{R}^{N_{\mathrm{C}}} \tag{12.5.7}$$

This result shows that the initial colloid–polymer mixture has been mapped onto a system of N_{C} colloidal particles for which the total interaction energy is

$$V^{\mathrm{eff}}(\{\mathbf{R}_i\})=V_{\mathrm{CC}}(\{\mathbf{R}_i\})+\Omega_{\mathrm{P}}(V,T,\mu;\{\mathbf{R}_i\}) \tag{12.5.8}$$

which depends on the thermodynamic state variables V,T and μ. The semi-grand partition function (12.5.7) is therefore equivalent to the canonical partition function of a system of N_{C} interacting colloidal particles for which the total potential energy is given by (12.5.8). The derivation of (12.5.8) takes no account the internal partition function of the polymer coil; it implicitly assumes that a coarse-grained representation of the polymer coils has been used. The

internal partition function would contribute a temperature-dependent term to the effective potential energy but is independent of the colloid configuration. This contribution is conventionally referred to as a 'volume' term; it may affect the thermodynamic properties of the suspension but not its structure.

As an illustration of (12.5.8) consider a model of hard sphere colloids and non-interacting polymers which are excluded from a sphere of radius $R_x = R_0 + R_g$ around each of the colloids. This is an extreme example of a non-additive hard-sphere mixture with diameters (in the notation of Section 3.10) given by $d_{11} = 2R_0, d_{22} = 0$ and $d_{12} = \frac{1}{2}(d_{11} + d_{22})(1 + \Delta)$, where $\Delta = 1 + R_g/R_0$; it is equivalent to an ideal gas confined to an accessible volume $\mathcal{V}(\{\mathbf{R}_i\})$, the magnitude of which depends on the instantaneous colloid configuration. The accessible volume is the volume of the suspension less the volume occupied by colloidal particles and their exclusion shells. Since exclusion spheres may overlap, $\mathcal{V}(\{\mathbf{R}_i\})$ will in general be a highly complicated function of the colloid coordinates. Formally, according to (2.4.11), which is valid for ideal particles:

$$\Xi_P^{id} = \exp[z\mathcal{V}(\{\mathbf{R}_i\})] \tag{12.5.9}$$

where z is equal to ρ_R, the polymer reservoir density, not the polymer density in the mixture. Thus

$$\Omega_P(V, T, \mu; \{\mathbf{R}_i\}) = -\rho_R k_B T \mathcal{V}(\{\mathbf{R}_i\}) = -\Pi\mathcal{V}(\{\mathbf{R}_i\}) \tag{12.5.10}$$

where Π is the osmotic pressure of the polymers, which is assumed to take its ideal value.

Consider first the case of a pair of colloidal particles, as pictured in Figure 12.8; $\mathcal{V}$ is now dependent only on the distance R between the centres of the spheres and the effective, depletion-induced, pair potential is

$$\begin{aligned} v_2(R) &= \Omega_P(T, \rho_R; R) - \Omega_P(T, \rho_R; R \to \infty) \\ &= 0, \quad R > 2R_x \\ &= -\rho_R k_B T \frac{4\pi}{3} R_x^3 \left[1 - \frac{3R}{4R_x} + \frac{1}{16}\left(\frac{R}{R_x}\right)^3\right], \quad 2R_0 < R < 2R_x \end{aligned} \tag{12.5.11}$$

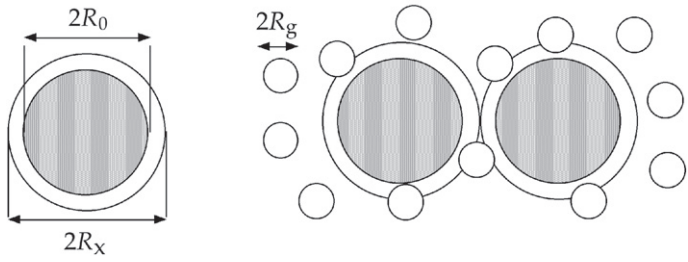

FIGURE 12.8 Exclusion zones around two hard-sphere colloids in a polymer solution.

where $R_x = R_0 + R_g$ is the radius of the exclusion sphere shown in Figure 12.8 and the last line involves the volume of intersection of two exclusion spheres separated by a distance R, which vanishes when $R > 2R_x$. Equation (12.5.11) is a famous result, first obtained by Asakura and Oosawa.[46]

The range of interaction increases with polymer size and its amplitude increases with polymer concentration. The effective interaction between colloids can therefore be tuned by changes in the two physical parameters. As the colloid concentration increases, overlap of the exclusion spheres of more than two colloids becomes increasingly probable, leading to effective, many-body interactions. All pair and higher-order interactions can be taken into account within thermodynamic perturbation theory,[47] whereby the system of unperturbed hard-sphere colloids is chosen as a reference system and the accessible volume $\mathcal{V}(\{\mathbf{R}_i\})$ in (12.5.10) is replaced by its mean value, $\bar{\mathcal{V}} = \alpha V$, obtained by averaging over all configurations of the reference system. The accessible volume fraction α depends only on the colloid packing fraction $\eta_C = 4\pi R_0^3 N_C/3V$ and the polymer–colloid size ratio $q = R_g/R_0$. The free energy of the colloid–polymer system therefore splits into two parts:

$$F = F_C(V, T, N_C) + F_P(\alpha V, T, N_P) \tag{12.5.12}$$

The excess free energy of the hard-sphere system is given by the Carnahan–Starling result (3.9.21) for the fluid phase or by an empirical equation of state for the face-centred cubic, solid phase,[44] while the free energy of the non-interacting polymers is, from (2.3.16):

$$F_P(\alpha V, T, N_P) = V\rho k_B T \ln(\rho \Lambda_P^3/\alpha - 1) \tag{12.5.13}$$

The remaining task is to estimate the accessible volume fraction $\alpha(\eta_C)$. This is achieved by a straightforward generalisation of Widom's particle insertion formula (2.4.33) in which the test particle in Figure 2.2 is of radius R_x and the probability p_0 is equal to α. Thus

$$\alpha = \exp\left(-\beta\mu^{ex}\right) \tag{12.5.14}$$

where μ^{ex} is the excess chemical potential of a particle of radius R_x in a binary mixture with hard spheres of smaller radius R_0 in the limit of vanishing concentration of the test particle species. If the Percus–Yevick approximation is used for μ^{ex}, we find that α is given by a simple formula:

$$\alpha = (1 - \eta_C)\exp\left(-A\gamma - B\gamma^2 - C\gamma^3\right) \tag{12.5.15}$$

where $\gamma = \eta_C/(1 - \eta_C)$, $A = 3q + 3q^2 + q^3$, $B = 9q^2/2 + 3q^3$ and $C = 3q^3$. By equating the chemical potentials and osmotic pressures of the two species in coexisting colloid gas, liquid or crystal phases it is possible to deduce the phase diagram of the colloid–polymer mixture for any value of q in the η_R versus η_C plane, where $\eta_R = 4\pi\rho_R R_g^3/3$ is the polymer packing fraction in the reservoir. The polymer-induced, effective attraction between the colloidal

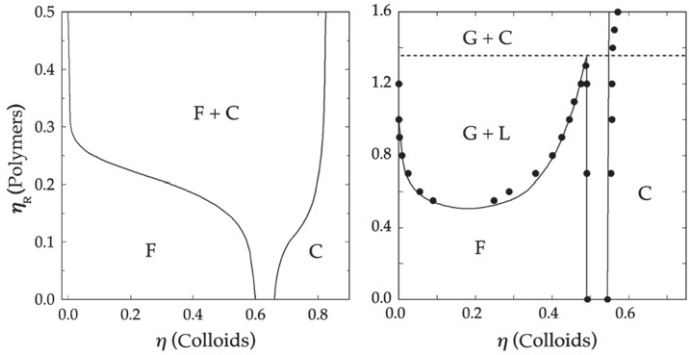

FIGURE 12.9 Phase diagrams of the Asakura–Oosawa model of a colloid–polymer mixture for two values of the size ratio q. Left-hand panel: $q = 0.1$. From H.N.W. Lekkerkerker et al., 'Phase behaviour of colloid + polymer mixtures', *Europhys. Lett.* **20**, 559–564 (1992). Right-hand panel: $q = 0.6$; the points show the results of Monte Carlo calculations. *Redrawn with permission from Ref. 47 © 2006 American Physical Society.*

particles drives a gas–liquid phase separation, while the hard-sphere repulsion leads to a liquid–crystal phase transition at sufficiently high values of η_C; in the limit of vanishing polymer density ($\mu_P \to -\infty$), colloid crystallisation reduces to that of hard spheres.

Figure 12.9 shows the phase diagrams[47,48] of the Asakura–Oosawa model, augmented by the correction for many-body interactions provided by (12.5.13), for two values of the size ratio q. For $q = 0.1$ the gas–liquid transition is pre-empted by a fluid–crystal transition; hence there is no colloid liquid phase. For q greater than approximately 0.32 a gas–liquid critical point emerges and the phase diagram resembles that of a simple liquid, such as that shown in Figure 1.1, with η_R playing the role of an inverse temperature. As q increases further, the critical packing fractions of polymers and colloids both decrease, while the ratio of critical to triple point packing fraction for the polymers increases. The phase diagram is therefore very sensitive to the range of the depletion-induced attraction relative to the size of the colloidal particles. If the range is too short, the liquid phase disappears altogether, or is at best metastable to freezing, as seen in experiments[49] on PMMA–polystyrene mixtures, where three-phase coexistence occurs only for q greater than approximately 0.25.

The phase diagrams of Figure 12.9 should provide a fair description of the phase behaviour of real colloidal systems under θ-solvent conditions but in good solvent the interactions between polymer coils cannot be ignored. More realistic models[50] that include effective polymer–polymer and colloid–polymer interactions, constructed in ways similar to those described in Section 12.2, have been used in Gibbs ensemble Monte Carlo calculations[51] for a range of values of q. The calculated phase diagrams are topologically similar to those in Figure 12.9, but there are major quantitative and even qualitative differences. For $q = 0.34$ there is reasonable agreement between the results for interacting and

non-interacting polymers; in each case the gas–liquid transition is metastable relative to freezing. As q increases,[52] the differences become greater. These are particularly pronounced in the location of the triple point, for which the inclusion of interactions leads to very good agreement with experimental results,[49] whereas in the non-interacting case the triple point moves to polymer reservoir packing fractions that are much too high.

In binary mixtures of large and small hard-sphere colloids, or of colloids and nanoparticles, the small hard spheres can act as depletants. The interaction thereby induced between two large spheres is attractive at short range and damped oscillatory at larger distances; the oscillations arise from a layering of the small spheres around the large ones.[53] Monte Carlo simulations[54] based on an effective pair potential lead, for q less than about 0.2, to a fluid–solid coexistence curve that widens considerably as the small sphere packing fraction increases; this has the effect of pre-empting a fluid–fluid transition. This behaviour is qualitatively similar to that observed for a colloid–polymer mixture and confirmed by simulations of the underlying hard-sphere mixture. It implies that the fluid–fluid phase separation predicted for a highly asymmetric binary mixture by thermodynamically self-consistent integral equations[55] is only metastable, but may nonetheless be observable, given the slow rates of crystal nucleation expected for such a system.

As we have seen, a feature of colloid–polymer mixtures is that no fluid–fluid critical point exists if the range of the effective, attractive forces between colloidal particles is too short. Similar considerations apply to simpler systems. Analysis of results obtained for a number of spherically symmetric pair potentials has shown, as would be expected, that the reduced critical temperature $T_c^* = k_B T/\epsilon$, where ϵ is the depth of the potential well, decreases rapidly with a reduction in range of the attractive interaction. What is surprising is the fact that the value of the reduced second virial coefficient $B_2^*(T_c)$ is insensitive to variation in range or choice of potential and given[56] to a good approximation by

$$B_2^*(T_c) = \frac{B_2(T_c)}{v_0} \approx -6 \tag{12.5.16}$$

where $v_0 = \pi d^3/6$ is the volume of a particle of effective diameter d. A striking illustration of this apparent 'universality' is the fact that for the mean field equation of state (5.7.4), which is most accurate when the range of attraction is large, $B_2^* \approx -6.66$, while for the Baxter sticky-sphere model (4.4.18), representative of very short-ranged attractions, $B_2^* \approx -6.2$. Use of (12.5.16) therefore allows a rough estimate of the critical temperature to be made from a simple integral involving only the pair potential. This semi-empirical line of reasoning has been carried further by the suggestion that an extended law of corresponding states[57] applies to non-conformal potentials, the difference compared with conformal potentials (3.10.1) being that the compressibility factor $\beta P/\rho$ is now a function of three, rather than two reduced variables: $T^* = k_B T/\epsilon, \rho^* = \rho d^3$ and $B_2^* = B_2/v_0$, where d is related to the repulsive part of the potential by the

Barker–Henderson prescription (5.4.11). The effective range q of an arbitrary, attractive potential is then taken to be the range of attraction, $q = \gamma - 1$ (see Figure 1.2), for a square-well potential having the same, reduced second virial coefficient as the potential of interest. With this definition of q, the boundary of stability of the fluid–fluid transition for a wide variety of non-conformal potentials is found to lie within a narrow range extending from about 0.13 to 0.15.

12.6 CHARGE-STABILISED COLLOIDS

We now show how the methods developed in earlier sections can be adapted to the calculation of the effective interaction between large polyions in solution. As our main example we take the case of a dispersion of hard sphere, colloidal particles of radius R_0 in a polar solvent of dielectric constant ϵ. We assume that each particle carries a uniform charge density σ, corresponding to a total charge equal to Ze ($|Z| \gg 1$), which gives rise an electric double layer at the surface similar to that formed near a charged, planar surface, as described in Section 10.6. We again adopt a primitive-model description of the solvent, with both coions and counterions represented as charged hard spheres of diameter $d(\ll R_0)$, and assume that the dispersion is in equilibrium with a salt reservoir that fixes the chemical potentials μ_+, μ_- of the microions. The three-component system can be described within the semi-grand canonical ensemble introduced in the previous section, characterised here by the variables V, T, N_0, μ_+ and μ_-. Thus the number of polyions, N_0, is fixed but the numbers of microions, N_+ and N_-, are allowed to fluctuate. If, as before, we denote the coordinates of the large particles (polyions, subscript 0) by $\{\mathbf{R}_i\}$ and those of the small particles (microions, subscript M) by $\{\mathbf{r}_j\}$, the total potential energy of the system may be written in short-hand form as

$$V_{\{N\}}\big(\{\mathbf{R}_i\},\{\mathbf{r}_j\}\big) = V_{00}\big(\{\mathbf{R}_i\}\big) + V_{\mathrm{MM}}\big(\{\mathbf{r}_j\}\big) + V_{0\mathrm{M}}\big(\{\mathbf{R}_i\},\{\mathbf{r}_j\}\big) \qquad (12.6.1)$$

where V_{00}, V_{MM} and $V_{0\mathrm{M}}$ are all sums of pair potentials of primitive-model type and $\{N\} \equiv N_0, N_+, N_-$.

The coarse-graining approach that we adopt has a now familiar pattern in which the degrees of freedom of the microions are averaged out, thereby reducing the problem to that of an effective, one-component system of polyions dressed by their electric double layers. This reduction is accomplished by writing the semi-grand partition function of the semi-grand canonical system in a form similar to (12.5.7):

$$\Xi(V,T,N_0,\mu_+,\mu_-) = \frac{1}{N_0!\Lambda_0^{3N_0}} \times \int \exp[-\beta V_{00}(\{\mathbf{R}_i\})]\Xi_{\mathrm{M}}\big(V,T,\mu_+,\mu_-;\{\mathbf{R}_i\}\big)\mathrm{d}\mathbf{R}^{N_0} \qquad (12.6.2)$$

where

$$\Xi_{\mathrm{M}} = \sum_{N_+=0}^{\infty} \sum_{N_-=0}^{\infty} \frac{z_+^{N_+} z_-^{N_-}}{N_+! N_-!} \iint \exp\left[-\beta\left(V_{\mathrm{MM}}\left(\{\mathbf{r}_j\}\right) + V_{0\mathrm{M}}\left(\{\mathbf{R}_i\}, \{\mathbf{r}_j\}\right)\right]\mathrm{d}\mathbf{r}^{N_+}\, \mathrm{d}\mathbf{r}^{N_-} \qquad (12.6.3)$$

is the grand partition function of the microions in the external potential $\phi_\nu(\mathbf{r})$ of the polyions in a configuration $\{\mathbf{R}_i\}$:

$$\phi_\nu(\mathbf{r}) = \sum_{i=1}^{N_0} v_{0\nu}(|\mathbf{r} - \mathbf{R}_i|), \quad \nu = +, - \qquad (12.6.4)$$

and z_+, z_- are the activities of the microions. Equation (12.6.2) may be re-expressed as

$$\Xi(V, T, N_0, \mu_+, \mu_-) = \frac{1}{N_0! \Lambda_0^{3N_0}} \int \exp\left(-\beta V^{\mathrm{eff}}(\{\mathbf{R}_i\})\right)\mathrm{d}\mathbf{R}^{N_0} \qquad (12.6.5)$$

in which the effective interaction between the dressed polyions is

$$V^{\mathrm{eff}}\left(\{\mathbf{R}_i\}\right) = V_{00}\left(\{\mathbf{R}_i\}\right) + \Omega_{\mathrm{M}}\left(V, T, \mu_+, \mu_-; \{\mathbf{R}_i\}\right) \qquad (12.6.6)$$

where $\Omega_{\mathrm{M}} = -k_{\mathrm{B}}T \ln \Xi_{\mathrm{M}}$ is the grand potential of the microions. The first term on the right-hand side of (12.6.6) arises from the direct interaction between polyions, while the second is a state-dependent, microion-induced interaction, which depends parametrically on the coordinates $\{\mathbf{R}_i\}$. The direct interaction is pairwise additive but the effective interaction is not; the effective interaction also includes a volume term which is independent of the polyion coordinates.[58]

The grand potential Ω_{M} can be evaluated by the methods of density functional theory. If we limit ourselves to a mean field approach we may take over the grand potential functional defined by (10.6.6), (10.6.7) and (10.6.10) (with $\mathcal{F}^{\mathrm{corr}} = 0$). The solution of the resulting Euler–Lagrange equations for the local densities $\rho_\nu^{(1)}(\mathbf{r})$ in the multi-centre, external potential (12.6.4) poses a formidable task. Numerical results can be obtained through a molecular dynamics scheme in which the Fourier components of the local densities are treated as dynamical variables,[59] a scheme inspired by the Car–Parrinello method for simulating systems of classical ions and quantum mechanical, valence electrons.[60] Further progress can be made analytically if the inhomogeneities induced by the polyions are assumed to be weak. In that case it is justifiable to expand the ideal free energy functional (3.1.22) to second order in the deviation $\Delta\rho_\nu^{(1)}(\mathbf{r})$ of the local density from its bulk value, i.e.

$$\Delta\rho_\nu^{(1)}(\mathbf{r}) = \rho_\nu^{(1)}(\mathbf{r}) - n_\nu \qquad (12.6.7)$$

The intrinsic free energy functional of the microions is then

$$\mathcal{F}\left[\rho_+^{(1)}, \rho_-^{(1)}\right] = \sum_\nu \left(F^{\mathrm{id}}(n_\nu) + k_\mathrm{B}T \ln\left(n_\nu \Lambda_\nu^3\right) \int \Delta\rho_\nu^{(1)}(\mathbf{r})\mathrm{d}\mathbf{r} + \frac{k_\mathrm{B}T}{2n_\nu} \int \left[\Delta\rho_\nu^{(1)}\mathbf{r}\right]^2 \mathrm{d}\mathbf{r} \right) + \frac{1}{2}\int e\rho_Z(\mathbf{r})\Phi^\mathrm{C}(\mathbf{r})\mathrm{d}\mathbf{r} \tag{12.6.8}$$

where the electrostatic potential $\Phi^\mathrm{C}(\mathbf{r})$ satisfies Poisson's equation (10.6.3). Substitution of (12.6.8) in (10.6.6), replacement of the chemical potentials μ_ν by their ideal values, and use of the variational principle (3.4.3) gives

$$\frac{\Delta\rho_\nu^{(1)}(\mathbf{r})}{n_\nu} + z_\nu \Phi^\mathrm{C}(\mathbf{r}) = -\beta\phi_\nu(\mathbf{r}), \quad \nu = +, - \tag{12.6.9}$$

The last two equations are coupled through the terms in $\Phi^\mathrm{C}(\mathbf{r})$. If the polyions were point particles, the coulombic contribution to $\phi_\nu(\mathbf{r})$ would be everywhere equal to $z_\nu e\Phi^\mathrm{ext}(\mathbf{r})$, where $\Phi^\mathrm{ext}(\mathbf{r})$ is the 'external' electrostatic potential acting on the microions.[61] If there were no boundaries, the total electrostatic potential within the fluid would then be

$$\Phi(\mathbf{r}) = \Phi^\mathrm{C}(\mathbf{r}) + \Phi^\mathrm{ext}(\mathbf{r}) = e\int \frac{\rho_Z(\mathbf{r}') + Z\rho^\mathrm{ext}(\mathbf{r}')}{\epsilon|\mathbf{r}-\mathbf{r}'|}\mathrm{d}\mathbf{r}' \tag{12.6.10}$$

where $\rho^\mathrm{ext}(\mathbf{r}) = \sum_i \delta(\mathbf{r}-\mathbf{R}_i)$ is the microscopic density of the polyions. Equation (12.6.9) now becomes

$$\Delta\rho_\nu^{(1)}(\mathbf{r}) = -\frac{n_\nu z_\nu e^2}{k_\mathrm{B}T}\int \frac{\rho_Z(\mathbf{r}') + Z\rho^\mathrm{ext}(\mathbf{r}')}{\epsilon|\mathbf{r}-\mathbf{r}'|}\mathrm{d}\mathbf{r}' \tag{12.6.11}$$

To simplify the problem, we consider only the salt-free case, where all microions are counterions. The coupled equations (12.6.11) then reduce to a single integral equation from which the subscript ν can be dropped and the charge density $\rho_Z(\mathbf{r})$ replaced by $z\rho^{(1)}(\mathbf{r})$. On taking Fourier transforms of both sides of (12.6.11), applying the convolution theorem and incorporating the result in (10.1.5), we find that the Fourier transform of $\Delta\rho^{(1)}(\mathbf{r})$ is

$$\hat{\rho}^{(1)}(\mathbf{k}) = \frac{Zk_\mathrm{D}^2}{k^2+k_\mathrm{D}^2}\sum_{i=1}^{N_0}\exp\left(-i\mathbf{k}\cdot\mathbf{R}_i\right) \tag{12.6.12}$$

where $k_\mathrm{D}^2 = 4\pi n z^2 e^2/\epsilon k_\mathrm{B}T$ is the square of the Debye wavenumber associated with the counterions. Inverse Fourier transformation of (12.6.12) leads to a counterion density profile given by

$$\rho^{(1)}(\mathbf{r}) = \sum_{i=1}^{N_0}\frac{Zk_\mathrm{D}^2}{4\pi}\frac{\exp\left(-k_\mathrm{D}|\mathbf{r}-\mathbf{R}_i|\right)}{|\mathbf{r}-\mathbf{R}_i|} \equiv \sum_{i=1}^{N_0}\rho_i^{(1)}(\mathbf{r}) \tag{12.6.13}$$

The total profile is therefore a superposition of profiles associated with each of the polyions. The radius of the polyions is now reintroduced by imposing the constraint that $\rho_i^{(1)}(\mathbf{r})$ must be zero whenever $|\mathbf{r} - \mathbf{R}_i| < R$. Charge neutrality means that $\rho_i^{(1)}(\mathbf{r})$ must be normalised such that

$$\int_{|\mathbf{r}-\mathbf{R}_i|>R} \rho_i^{(1)}(\mathbf{r})\mathrm{d}\mathbf{r} = |Z/z| \tag{12.6.14}$$

For the profile defined by (12.6.13) this requirement would be met if the polyion charge Ze were replaced by an apparent charge $Z'e$, where

$$Z' = Z\frac{\exp(k_\mathrm{D}R)}{1 + k_\mathrm{D}R} \tag{12.6.15}$$

The normalisation in (12.6.14) implicitly assumes that the colloid concentration is low and hence that the electric double layers associated with neighbouring polyions have, on average, little overlap. From Poisson's equation it is evident that the total electrostatic potential may similarly be written as a superposition of N_0 screened potentials:

$$\Phi(\mathbf{r}) = \sum_{i=1}^{N_0} \frac{Z'e}{\epsilon}\frac{\exp(-k_\mathrm{D}|\mathbf{r} - \mathbf{R}_i|)}{|\mathbf{r} - \mathbf{R_i}|} \equiv \sum_{i=1}^{N_0} \Phi_i(\mathbf{r}) \tag{12.6.16}$$

If the density profile (12.6.13) and the potential (12.6.16) are substituted in the free energy functional (12.6.8), we find that the effective interaction energy (12.6.6) takes the form

$$V^{\mathrm{eff}}(\{\mathbf{R}_i\}) = V_0 + \sum_i \sum_{j>i} v_2(|\mathbf{R}_j - \mathbf{R}_i|) \tag{12.6.17}$$

where the effective pair potential $v_2(R)$ provides the electrostatic contribution to the Derjaguin–Landau–Verwey–Overbeek (DLVO) potential[62]:

$$\begin{aligned} v_2(|\mathbf{R}_j - \mathbf{R}_i|) &= \int \Phi_i(\mathbf{r})\rho_j^{(1)}(\mathbf{r})\mathrm{d}\mathbf{r} \\ &= \frac{Z'^2e^2}{\epsilon}\frac{\exp(-k_\mathrm{D}|\mathbf{R}_j - \mathbf{R}_i|)}{|\mathbf{R}_j - \mathbf{R}_i|} \end{aligned} \tag{12.6.18}$$

The pairwise additivity is a consequence of the quadratic form of the approximate functional (12.6.8).

The effective interaction energy (12.6.17) contains a structure-independent term, V_0. This term has no effect on the forces acting between the polyions, but it has a significant influence on the phase diagram.[58] It includes, among other contributions, the self-energy of the double layers associated with individual polyions. The DLVO potential is a function of density and temperature through

its dependence on the Debye wavenumber; its form remains the same even in the presence of coions provided the contributions of all microions are included in the definition of k_D and in V_0. It is strictly repulsive, which would stabilise the system against flocculation induced by the van der Waals forces that are present in any real dispersion. On the other hand, if the salt concentration is sufficiently low, the structure-independent term can drive a phase transition into colloid-rich and colloid-poor dispersions even in the absence of attractive forces.

A quadratic functional would seem unlikely to be adequate for use in calculations for systems of highly charged particles. In practice the strong electrostatic attraction exerted by the polyions on the counterions leads to a substantial fraction of the latter becoming tightly bound to the colloid surface; this 'counterion condensation' reduces[63] the magnitude of the bare polyion charge to an effective value $|Z_{\text{eff}}| < |Z|$. The remaining counterions therefore experience a much weaker external potential, so the diffuse part of the double layer may still be described within the quadratic approximation. The functional can also be extended in a way that allows the determination of effective, three-body interactions.[64] For triplet configurations close to contact the three-body interaction provides a substantial, attractive correction to the pairwise-additive, repulsive interaction described by (12.6.18). Nonetheless, direct measurement of the effective pair potential between charged colloidal particles shows that (12.6.18) provides a good representation of the data when Z_{eff} is suitably chosen, as the results shown in Figure 12.10 illustrate.

An explicit relation between $|Z|$ and $|Z_{\text{eff}}| < |Z|$ can be derived within Poisson–Boltzmann theory.[66] Consider the case of an isolated planar surface

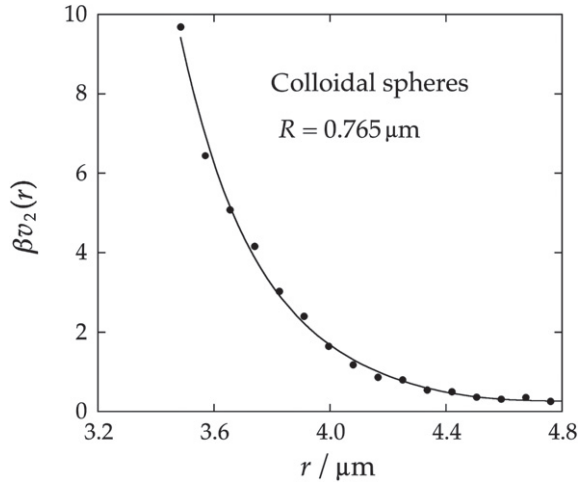

FIGURE 12.10 Effective pair potential between polystyrene sulphate spheres of radius $0.765 \pm 0.01\,\mu\text{m}$ dispersed in water. The points are experimental results and the curve is calculated from (12.6.18) for an effective charge $|Z_{\text{eff}}| = 22,793$. *Redrawn with permission from Ref. 65 © 1994 American Physical Society.*

immersed in a symmetric electrolyte of bulk concentration n_0, already discussed in Section 10.6. Use of the identity $\tanh^{-1} x = \frac{1}{2}\ln[(1+x)/(1-x)]$ allows the solution (10.6.23) of the Poisson–Boltzmann equation for the dimensionless electrostatic potential to be written in the form

$$\Phi^*(z) = 2\ln\left(\frac{1 + g\exp(-k_{\mathrm{D}}z)}{1 - g\exp(-k_{\mathrm{D}}z)}\right) \tag{12.6.19}$$

while the boundary condition (10.6.16) yields an expression for g:

$$g = (1 + x^2)^{1/2} - x \tag{12.6.20}$$

where $x = k_{\mathrm{D}}e/2\pi l_{\mathrm{B}}\sigma$. Far from the charged plane, $k_{\mathrm{D}}z \gg 1$, and to linear order $\Phi^*(z)$ reduces to

$$\Phi^*(z) \approx \Phi_S^* \exp(-k_{\mathrm{D}}z), \quad k_{\mathrm{D}}z \gg 1 \tag{12.6.21}$$

where $\Phi_S^* = 4g$. Thus for $z = 0$:

$$\left.\frac{\partial\Phi^*(z)}{\partial z}\right|_{z=0} = -4k_{\mathrm{D}}g \tag{12.6.22}$$

The linearised Poisson–Boltzmann equation

$$\frac{\mathrm{d}^2}{\mathrm{d}z^2}\Phi^*(z) = k_{\mathrm{D}}^2\Phi^*(z) \tag{12.6.23}$$

has a solution of the same form as (12.6.21) but if that solution is to be consistent with (12.6.22) the bare charge density in the boundary condition (10.6.16) must be replaced by an effective charge

$$\sigma_{\mathrm{eff}} = \frac{ek_{\mathrm{D}}g}{\pi l_{\mathrm{B}}} \tag{12.6.24}$$

with g given by (12.6.20). On defining what turns out to be a saturation charge density $\sigma_{\mathrm{sat}} = k_{\mathrm{D}}e/\pi l_{\mathrm{B}}$, we see that $x = \sigma_{\mathrm{sat}}/2\sigma$. If the surface charge density is very low, i.e. if $x \gg 1$, then $g \approx (1 - 1/4x^2)/2x$ and

$$\sigma_{\mathrm{eff}} \approx \sigma\left[1 - (\sigma/\sigma_{\mathrm{sat}})^2\right], \quad \sigma \ll \sigma_{\mathrm{sat}} \tag{12.6.25}$$

while in the opposite limit of very high charge density, $x \ll 1$, $g \approx 1 - x$ and

$$\sigma_{\mathrm{eff}} \approx \sigma_{\mathrm{sat}}\left[1 - (\sigma_{\mathrm{sat}}/2\sigma)\right], \quad \sigma \gg \sigma_{\mathrm{sat}} \tag{12.6.26}$$

As expected, the effective surface charge reduces to its bare value when that is low; counterion condensation is negligible and linear Poisson–Boltzmann theory is adequate. For high surface charge, the effective value reaches its maximum value σ_{sat}, which is independent of σ. In that case counterion

condensation strongly reduces the absolute value of the bare charge and the linear theory remains applicable to the diffuse part of the double layer.

A similar argument to that just outlined applies in the case of an isolated colloidal sphere of radius R_0 and bare charge Ze in a symmetric electrolyte. The radial Poisson–Boltzmann equation for this problem has no analytical solution, but in the limit $R_0 \gg k_D^{-1}$, where planar geometry is recovered, the calculations become simpler and show that the effective charge at saturation is[66]

$$Z_{sat} = \frac{4R_0}{l_B}(1 + k_D R_0) \tag{12.6.27}$$

An improved estimate of Z_{sat}, valid down to $k_D R_0 \approx 1$ has also been obtained, together with an analytical approximation for its dependence on the bare charge.[67]

Thus far we have considered only the case of a single polyion in a bulk electrolyte, corresponding to the limit of infinite dilution of the polyions. At high concentrations the polyions form a dense, colloidal fluid in which each particle is confined to a cage formed by its nearest neighbours. This situation is well described by a Wigner–Seitz cell model in which each polyion is placed at the centre of a cell of volume $v = V/N_0$ together with monovalent coions and counterions in osmotic equilibrium with a reservoir of overall concentration n_0; the total charge within the cell is assumed to vanish.[68] The geometry of the cell mimics the shape of the polyion; thus for spherical ions the cell is a sphere of radius $a = (3v/4\pi)^{1/3}$. Since the cell is overall neutral, it does not interact with the cells associated with neighbouring polyions, so calculations are needed for only a single sphere. The radial Poisson–Boltzmann equation is now

$$\left(\frac{d^2}{dr^2} + \frac{2}{r}\frac{d}{dr}\right)\Phi^*(r) = k_{D0}^2 \sinh \Phi^*(r), \quad R_0 < r < a \tag{12.6.28}$$

where $k_{D0}^2 = 4\pi n_0 l_B$. Equation (12.6.28) must be solved subject to boundary conditions at $r = R_0$ (surface of the polyion) and $r = a$ (surface of the Wigner–Seitz cell):

$$\left.\frac{d\Phi^*(r)}{dr}\right|_{r=R} = -\frac{Zl_B}{R^2}, \quad \left.\frac{d\Phi^*(r)}{dr}\right|_{r=a} = 0 \tag{12.6.29}$$

The microion charge density within the Wigner–Seitz sphere is

$$\rho_Z(r) = \rho_+^{(1)}(r) - \rho_-^{(1)}(r) = -\frac{k_{D0}^2}{4\pi l_B}\sinh \Phi^*(r) \tag{12.6.30}$$

and its integral over the available volume, for a polyion of charge $-Ze$, is equal to Z:

$$4\pi \int_{R_0}^{a} \rho_Z(r) r^2 \, dr = Z \tag{12.6.31}$$

Equation (12.6.28) can be solved numerically for the electrostatic potential, in particular for its value at $r = a$; this is the only numerical input needed to determine the effective charge. The analytical solution involves expansion of

$\Phi^*(r)$ and $\rho_Z(r)$ to first order around $\Phi^*(a)$; the resulting, linear equation for $\delta\Phi^*(r) = \Phi^*(r) - \Phi^*(a)$ is

$$\left(\frac{\mathrm{d}^2}{\mathrm{d}r^2} + \frac{2}{r}\right)\delta\Phi^*(r) = k_{\mathrm{D}0}^2\left(\gamma_a + \delta\Phi^*\right), \quad R < r < a \tag{12.6.32}$$

where $\gamma_a = \tanh \Phi^*(a)$ and the boundary conditions are now

$$\delta\Phi^*(a) = 0, \quad \frac{\mathrm{d}}{\mathrm{d}r}\delta\Phi^*(r)\bigg|_{r=a} = 0 \tag{12.6.33}$$

The solution to this equation determines the charge density via the linearised form of (12.6.30), i.e.

$$\rho_Z(r) \approx -\frac{k_{\mathrm{D}}^2}{4\pi l_{\mathrm{B}}}\left[\gamma_a + \delta\Phi^*(r)\right] \tag{12.6.34}$$

where $k_{\mathrm{D}}^2 = k_{\mathrm{D}0}^2 \cosh \Phi^*(a)$, and the effective charge of the polyion is obtained by substitution in (12.6.31). The value of Z_{eff} is given by a lengthy expression:

$$\begin{aligned} Z_{\mathrm{eff}} = \frac{\gamma_0}{k_{\mathrm{D}} l_{\mathrm{B}}}\Big[&(k_{\mathrm{D}}^2 Ra - 1)\sinh\left(k_{\mathrm{D}}(a-R)\right) + k_{\mathrm{D}}(a-R) \\ &\times \cosh\left(k_{\mathrm{D}}(a-R)\right)\Big] \end{aligned} \tag{12.6.35}$$

but its key feature is that Z_{eff} depends on the bare charge only through the term $\tanh \Phi^*(a)$, which is calculated from (12.6.28). The effective charge is therefore that charge which, within linearised Poisson–Boltzmann theory, leads at $r = a$ to the same electrostatic potential and its gradient as the full theory does for the bare charge Z. The fact that $|Z_{\mathrm{eff}}| < |Z|$ accounts implicitly for the effects of counterion condensation, thereby justifying the use of the linear theory at small values of r. This implies that the quantity Z' in the DLVO potential should be replaced by $Z'_{\mathrm{eff}} = Z_{\mathrm{eff}} \exp(k_{\mathrm{D}}R)/(1 + k_{\mathrm{D}}R)$.

While accounting approximately for the non-linearity of mean field Poisson–Boltzmann theory, charge renormalisation does not allow for microion correlations, which can no longer be ignored when multivalent microions are present. As shown in Section 10.6 for the case of parallel, charged plates, microion correlations may lead to charge inversion and hence to an effective attraction between like-charged polyions.[69] A simple model of charge inversion in the presence of multivalent counterions is based on the idea that highly correlated ions tightly bound to a planar, charged surface will form a two-dimensional, hexagonal Wigner crystal.[70] These periodic charge patterns lead to an attraction between two plates carrying surface charges of the same sign when the patterns on opposite plates are favourably staggered.[71] This is an appealing picture, but not one that is wholly consistent; it ignores the discreteness of the distribution of ionised sites on the colloid surface, which is replaced by a uniform charge density.

Application of the methods discussed thus far can be extended to systems of non-spherical particles. For example, much theoretical as well as experimental

work has been devoted to aqueous suspensions of laponite particles. Laponite is a synthetic clay consisting of disc-like particles which have a thickness to diameter ratio of approximately 0.03 and carry a substantial surface charge. In the semi-dilute regime, suspensions are found experimentally to undergo a transition from a liquid-like sol to a network-forming gel[72] or a colloidal glass,[73] depending on experimental conditions. At high concentration, the suspensions, like certain natural clays of geophysical importance, form lamellar stacks that swell as the ionic strength is increased. The swelling is linked to the effective interaction between electric double layers. It can be described by non-linear Poisson–Boltzmann theory applied to the problem of two parallel plates confined, together with coions and counterions, within a cylindrical Wigner–Seitz cell.[74] The DLVO potential (12.6.18) can also be generalised to the case of charged, anisometric particles by introduction of anisotropy factors that are dependent on the orientations of the two particles involved[75] and an explicit expression for the anisotropy factor of rod-like particles has been derived.

12.7 COLLOIDAL LIQUID CRYSTALS

The discussion of colloidal systems up till now has been focused on the properties of spherical, hard-core particles, but rod-like and plate-like, mesoscopic particles are also very common both in nature and in the laboratory. Examples include elongated particles, such as the tobacco mosaic virus, which has a length to thickness ratio of $\approx$15, and thin clay platelets such as gibbsite, a form of aluminium hydroxide. The orientational degrees of freedom confer on dispersions of elongated or flat hard bodies a very rich phase behaviour, with partially ordered *mesophases* appearing between the fully isotropic, fluid phase, and the three-dimensionally ordered, crystal phase. Dispersions of highly anisometric colloidal particles are referred to as *lyotropic* liquid crystals; their thermodynamic and structural properties are largely controlled by excluded volume effects. *Thermotropic* liquid crystals, by contrast, are dense assemblies of smaller molecules for which long-range, attractive interactions play an important role; temperature is therefore the key control parameter. Although the length scales involved may be very different, lyotropic and thermotropic liquid crystals are structurally similar, but are generated by varying the packing fraction at constant temperature in one case and by changes in temperature at constant pressure in the other. The properties of thermotropic liquid crystals and their theoretical description are dealt with at length in classic texts[76]; this section is devoted exclusively to the lyotropic case.[77]

The equilibrium, single-particle density of a system of rigid, non-spherical particles is a function of the centre-of-mass coordinates $\mathbf{R}$ of the particle and its orientation $\boldsymbol{\Omega}$ relative to a laboratory-fixed frame:

$$\rho^{(1)}(\mathbf{R}, \boldsymbol{\Omega}) = \left\langle \sum_{i=1}^{N} \delta(\mathbf{R}_i - \mathbf{R}) \delta(\boldsymbol{\Omega}_i - \boldsymbol{\Omega}) \right\rangle \tag{12.7.1}$$

As we shall limit the discussion to the case of uniaxial particles, $\mathbf{\Omega} = (\theta, \phi)$, where θ and ϕ are the usual polar angles. In the homogeneous, isotropic phase, $\rho^{(1)}$ is just the mean number density ρ, while the crystal phase has full translational periodicity and orientational order. In the *nematic* liquid crystal phase the particles are preferentially ordered along the *director*, a unit vector $\hat{\mathbf{n}}$ parallel to the polar axis, but the translational invariance characteristic of the liquid state persists. Thus

$$\rho^{(1)}(\mathbf{R}, \mathbf{\Omega}) = \rho \Psi(\mathbf{\Omega}) \quad \text{(nematic)} \tag{12.7.2}$$

where $\Psi(\mathbf{\Omega})$ is an orientational distribution function normalised such that $\int \Psi(\mathbf{\Omega}) \mathrm{d}\mathbf{\Omega} = 1$. As there is axial symmetry around the director, $\Psi(\mathbf{\Omega})$ is a function only of $\cos\theta = \hat{\mathbf{n}} \cdot \hat{\mathbf{\Omega}}$, where $\hat{\mathbf{\Omega}}$ is another unit vector. The degree of alignment of the particles is measured by a nematic order parameter $\mathcal{Q}$ defined as

$$\mathcal{Q} = \langle P_2(\cos\theta) \rangle_{\mathbf{\Omega}} = 2\pi \int_0^{\pi} \Psi(\cos\theta) P_2(\cos\theta) \sin\theta \, \mathrm{d}\theta \tag{12.7.3}$$

where $P_2(x)$ is the second-order Legendre polynomial. For perfectly aligned particles, $\mathcal{Q} = 1$, while in the isotropic phase $\mathcal{Q} = 0$.

The *smectic-A* phase has an orientationally ordered, lamellar structure which is also translationally ordered along the director. The single-particle density is now a function of the vertical coordinate z and orientation $\mathbf{\Omega}$:

$$\rho^{(1)}(\mathbf{R}, \mathbf{\Omega}) = \rho^{(1)}(z, \mathbf{\Omega}) = \rho^{(1)}(z, \hat{\mathbf{n}} \cdot \hat{\mathbf{\Omega}}) \quad \text{(smectic-A)} \tag{12.7.4}$$

This is a periodic function of z, meaning that $\rho^{(1)}(z + \ell h, \hat{\mathbf{n}} \cdot \hat{\mathbf{\Omega}}) = \rho^{(1)}(z, \hat{\mathbf{n}} \cdot \hat{\mathbf{\Omega}})$ for any integer ℓ, where h is the smectic layer thickness. The smectic-C phase also has a lamellar structure, but one in which the orientations of the particles are tilted relative to $\hat{\mathbf{n}}$. Plots of configurations of the isotropic, nematic, smectic-A and crystal phases of a system of elongated particles are shown in Figure 12.11.

Three hard-core models of lyotropic liquid crystals have been widely studied both theoretically and by simulation:

- Ellipsoids of revolution with major and minor axes of length, respectively, L and d, are prolate (elongated) if $L > d$ or oblate (flat) for $L < d$; the quantity $\kappa = L/d$ is called the *aspect ratio*.
- Cylinders of length L and diameter d are rod-like if $\kappa > 1$, and plate-like if $\kappa < 1$. Their behaviour in the so-called needle limit, where $\kappa \to \infty$, was studied by Onsager in a paper[78] that set the standard for theoretical work on lyotropic liquid crystals.
- Spherocylinders, pictured in Figure 12.11, are cylinders that are capped at both ends by hemispheres of the same diameter as the cylinder.

Transitions involving mesophases are accompanied by the appearance of orientational and translational inhomogeneities. The natural choice for their description within statistical mechanics is therefore density functional theory,

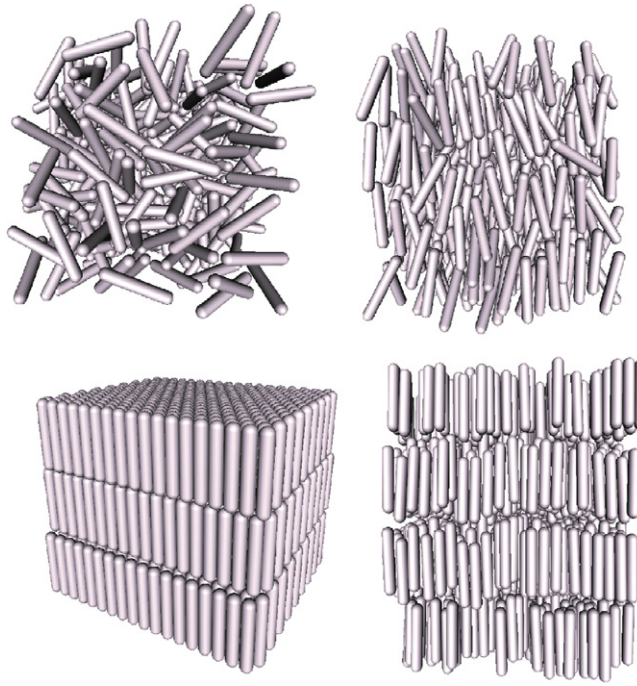

FIGURE 12.11 Plots, reading clockwise from upper left, of configurations of the isotropic, nematic, smectic-A and ordered crystal phases of a system of hard spherocylinders. Picture by courtesy of P. Bolhuis.

as described in Chapters 3 and 6; see, in particular, Section 6.8 for the application to freezing. The free energy is now a functional of $\rho^{(1)}(\mathbf{R}, \boldsymbol{\Omega})$ and can be written, as a generalisation of (3.3.2), in the form

$$\mathcal{F}[\rho^{(1)}] = \mathcal{F}^{\mathrm{id}}[\rho^{(1)}(\mathbf{R}, \boldsymbol{\Omega})] + \mathcal{F}^{\mathrm{ex}}[\rho^{(1)}(\mathbf{R}, \boldsymbol{\Omega})] \tag{12.7.5}$$

where the ideal contribution, which for spheres is given by (3.1.22), must now be integrated over all orientations. In the case of the nematic phase, $\rho^{(1)}$ is given by (12.7.2), and

$$\mathcal{F}^{\mathrm{id}}[\rho^{(1)}(\mathbf{R}, \boldsymbol{\Omega})] = Nk_{\mathrm{B}}T\left(\ln \rho\Lambda^3 - 1 + \int \Psi(\boldsymbol{\Omega}) \ln\left[4\pi\Psi(\boldsymbol{\Omega})\right] \mathrm{d}\boldsymbol{\Omega} \right) \tag{12.7.6}$$

In the isotropic phase, where $\Psi(\boldsymbol{\Omega}) = 1/4\pi$, the orientational contribution to $\mathcal{F}^{\mathrm{id}}$ vanishes.

We focus first on the isotropic–nematic transition. An approximate expression for the excess part of the free energy functional is required which, following Onsager,[78] can be based on the virial expansion of the free energy. To lowest order in density (6.2.21), which applies to hard spheres, may be

generalised to the case of non-spherical particles in the form

$$\beta\mathcal{F}^{\mathrm{ex}}[\rho^{(1)}(\mathbf{R},\boldsymbol{\Omega})] = -\frac{1}{2}\int \mathrm{d}\boldsymbol{\Omega}\int \mathrm{d}\boldsymbol{\Omega}'\int \mathrm{d}\mathbf{R}\int \mathrm{d}\mathbf{R}'\rho^{(1)}(\mathbf{R},\boldsymbol{\Omega}) f(\mathbf{R}'-\mathbf{R},\boldsymbol{\Omega},\boldsymbol{\Omega}')\rho^{(1)}(\mathbf{R}',\boldsymbol{\Omega}') \tag{12.7.7}$$

where $f(x)$ is the Mayer function, which, for hard particles, is equal to -1 when the particles overlap but is otherwise zero. Substitution of (12.7.2) in (12.7.7), followed by integration over $\mathbf{R}'$ gives

$$f^{\mathrm{ex}} = \frac{\beta\mathcal{F}^{\mathrm{ex}}}{N} = \frac{1}{2}\rho\int \mathrm{d}\boldsymbol{\Omega}\int \mathrm{d}\boldsymbol{\Omega}'\,\Psi(\boldsymbol{\Omega})v_{\mathrm{x}}(\boldsymbol{\Omega},\boldsymbol{\Omega}')\Psi(\boldsymbol{\Omega}') \tag{12.7.8}$$

where

$$v_{\mathrm{x}}(\boldsymbol{\Omega},\boldsymbol{\Omega}') = -\int f(\mathbf{r},\boldsymbol{\Omega},\boldsymbol{\Omega}')\mathrm{d}\mathbf{r} \tag{12.7.9}$$

is the excluded volume for two particles of orientations $\boldsymbol{\Omega},\boldsymbol{\Omega}'$, calculated by integration over relative coordinates $\mathbf{r}=\mathbf{R}'-\mathbf{R}$. The excluded volume for two hard cylinders of aspect ratio sufficiently large that end effects can be neglected is related to the angle $\gamma = \cos^{-1}(\hat{\boldsymbol{\Omega}}\cdot\hat{\boldsymbol{\Omega}}')$ between the long axes by[77b]

$$v_{\mathrm{x}} = 2L^2d|\sin\gamma(\boldsymbol{\Omega},\boldsymbol{\Omega}')| \tag{12.7.10}$$

In the isotropic phase, $\Psi(\boldsymbol{\Omega}) = 1/4\pi$, and (12.7.10) reduces to the second virial coefficient approximation for f^{ex}:

$$f^{\mathrm{ex}} = \frac{1}{2}\rho\frac{1}{(4\pi)^2}\int \mathrm{d}\boldsymbol{\Omega}\int \mathrm{d}\boldsymbol{\Omega}'v_{\mathrm{x}}(\boldsymbol{\Omega},\boldsymbol{\Omega}') = B_2\rho = B_2^*\eta \tag{12.7.11}$$

where $B_2 = \pi L^2d/4$ is the second virial coefficient in the limit $\kappa \gg 1$, $B_2^* = B_2/v_0$ and $\eta = \rho v_0$, $v_0 = \frac{1}{4}\pi Ld^2$ being the volume of a rod.

If the rods are sufficiently long, higher order terms in the virial expansion of the excess free energy can be neglected. The term of order ρ^2 would be

$$\frac{1}{2}B_3\rho^2 = \frac{1}{2}(B_3/B_2^2)(\rho B_2)^2$$

Onsager showed by use of geometric arguments that $B_3/B_2^2 \sim \kappa^{-1}\ln\kappa \to 0$ as $\kappa \to \infty$; the same is true for ratios of all higher-order coefficients, B_n/B_2^{n-1}. This behaviour has been confirmed by explicit, numerical calculation[79] of B_n/B_2^{n-1} as functions of κ for n in the range $3 \le n \le 5$, but convergence of the expansion is slow when the aspect ratio falls below $\kappa \approx 100$.

Combination of (12.7.6)–(12.7.10) leads to Onsager's free energy functional for the nematic phase:

$$f[\Psi(\boldsymbol{\Omega})] = \ln\rho\Lambda^3 - 1 + \int \Psi(\boldsymbol{\Omega})\ln\left[4\pi\Psi(\boldsymbol{\Omega})\right]\mathrm{d}\boldsymbol{\Omega} + \rho L^2d\int \mathrm{d}\boldsymbol{\Omega}\int \mathrm{d}\boldsymbol{\Omega}'\,\Psi(\boldsymbol{\Omega})|\sin\gamma(\boldsymbol{\Omega},\boldsymbol{\Omega}')|\Psi(\boldsymbol{\Omega}') + \mathcal{O}(\rho^2) \tag{12.7.12}$$

which must be minimised with respect to the orientational distribution function $\Psi(\mathbf{\Omega})$. The minimum arises from the competition between the orientational entropy, which favours the isotropic phase where all orientations are equally probable, and the excess term, which favours the nematic phase. The extremum condition analogous to (3.3.1), according to which

$$\frac{\delta f[\Psi(\mathbf{\Omega}]}{\delta \Psi(\mathbf{\Omega})} = \beta \mu_{\text{or}} \tag{12.7.13}$$

where μ_{or} is the orientational contribution to the chemical potential, leads to a non-linear equation for $\Psi(\mathbf{\Omega}) \equiv \Psi(\theta)$ in the form:

$$\Psi(\theta) = (4\pi)^{-1} \exp\left(\beta \mu_{\text{or}} - 2\rho L^2 d \int \Psi(\theta) |\sin \gamma(\mathbf{\Omega}, \mathbf{\Omega}')| \mathrm{d}\mathbf{\Omega}'\right) \tag{12.7.14}$$

Equation (12.7.14) always has the isotropic solution, for which $\Psi(\theta) = 1/4\pi$ and $\beta \mu_{\text{or}} = 2B_2\rho$. As the density increases, an anisotropic solution appears. Detailed analysis[77b,80] based on an expansion of $\Psi(\theta)$ around its isotropic form, i.e. $\Psi(\theta) = [1 + \epsilon \Delta \Psi(\theta)]/4\pi$, shows that the isotropic phase becomes unstable beyond a dimensionless concentration $c = \eta\kappa = 4$.

A more straightforward but approximate method,[77b] similar to that used in Section 6.8, is to use a trial function $\Psi_\alpha(\theta)$, dependent on a variational parameter α, and to minimise the free energy resulting from (12.7.12) with respect to α. A convenient choice for $\Psi_\alpha(\theta)$ is the properly normalised gaussian function:

$$\begin{aligned} \Psi_\alpha(\theta) &= A \exp\left(-\frac{1}{2}\alpha\theta^2\right), \qquad 0 \le \theta \le \frac{1}{2}\pi \\ &= A \exp\left(-\frac{1}{2}\alpha(\pi - \theta)^2\right), \quad \frac{1}{2}\pi < \theta < \pi \end{aligned} \tag{12.7.15}$$

where the two ranges of θ correspond, respectively, to orientations parallel or anti-parallel to the director. For large α, $\Psi_\alpha(\theta)$ is sharply peaked for orientations close to $\hat{n}$. With this simplification the prefactor is determined by the condition

$$\begin{aligned} \int_0^{\pi/2} \exp\left(-\frac{1}{2}\alpha\theta^2\right) \sin\theta \, \mathrm{d}\theta &\approx \int_0^{\infty} \exp\left(-\frac{1}{2}\alpha\theta^2\right) \left[\theta - \frac{1}{6}\theta^3 + \mathcal{O}(\theta^5)\right] \mathrm{d}\theta \\ &= 1/4\pi A(\alpha) \end{aligned} \tag{12.7.16}$$

from which it follows that

$$A(\alpha) \approx \frac{\alpha}{4\pi}\left(1 + \frac{1}{3\alpha} + \cdots\right) \tag{12.7.17}$$

Substitution of (12.7.15) and (12.7.17) in (12.7.12) gives

$$f(\alpha) \approx c + \ln\alpha + \frac{4c}{(\pi\alpha)^{1/2}} \tag{12.7.18}$$

and minimisation of $f(\alpha)$ shows that to leading order

$$\alpha \approx 4c^2/\pi \tag{12.7.19}$$

The corresponding value of the nematic order parameter is

$$\mathcal{Q} \approx 1 - \frac{3}{\alpha} \approx 1 - \frac{3\pi}{4c^2} \tag{12.7.20}$$

Coexistence between the isotropic (I) and nematic (N) phases is determined by equating the osmotic pressures and chemical potentials derived by the usual thermodynamic relations from the free energies of the two phases, (12.7.11) and (12.7.18). This leads to values of the packing fractions $\eta = c/\kappa = cd/L$ at coexistence given by

$$\eta_{\mathrm{I}} \approx 3.45d/L, \quad \eta_{\mathrm{N}} \approx 5.12d/L$$

and to an order parameter $\mathcal{Q} \approx 0.910$. The transition is strongly first order; not only are the rods highly aligned in the nematic phase but the increase in packing fraction is large ($\Delta\eta/\eta_{\mathrm{N}} \approx 0.33$). The values of the order parameter and of the two packing fractions are sensitive to the choice of trial function. For the function used by Onsager, i.e.

$$\Psi_\alpha(\theta) = \frac{\alpha \cosh(\alpha \cos\theta)}{4\pi \sinh\alpha} \tag{12.7.21}$$

the packing fractions are[78]

$$\eta_{\mathrm{I}} \approx 3.34d/L, \quad \eta_{\mathrm{N}} \approx 4.48d/L \quad \text{(Onsager)}$$

and $\mathcal{Q} \approx 0.848$. The important point to bear in mind, however, is that whatever the choice of trial function the theory is valid only for $L/d \gg 1$, a regime in which the packing fractions are sufficiently small for use of a second virial approximation to be justified. When the aspect ratio is less than about 100, the contributions from higher order terms are no longer negligible.

Several efforts have been made to extend Onsager's theory to physically relevant values of κ. A simple, phenomenological approach[81] uses a hard-sphere fluid as a reference system, the packing fraction of which is set equal to that of the system of interest. In the case of hard cylinders, the excess part of the free energy functional in (12.7.12) is replaced by

$$f^{\mathrm{ex}} = f_d^{\mathrm{ex}} \int \mathrm{d}\boldsymbol{\Omega} \int \mathrm{d}\boldsymbol{\Omega}' \Psi(\boldsymbol{\Omega}) \frac{v_{\mathrm{x}}(\boldsymbol{\Omega}, \boldsymbol{\Omega}')}{8v_0} \Psi(\boldsymbol{\Omega}') \tag{12.7.22}$$

where v_{x} is given by (12.7.10), $f_d^{\mathrm{ex}} = \eta(4 - 3\eta)/(1 - \eta)^2$ is the Carnahan–Starling expression for the excess free energy of the reference system, v_0 is the hard-sphere volume and the quantity $8v_0$ is the excluded volume around a hard sphere. At low densities, $f_d^{\mathrm{ex}} \approx 4\eta$ and Onsager's expression for $f^{\mathrm{ex}}[\Psi(\boldsymbol{\Omega})]$ in (12.7.12) is recovered. Though simple, the results obtained represent a significant improvement over Onsager's theory. In particular, for $\kappa = 5$, the predicted increase in density at the isotropic–nematic transition is reduced by an

order of magnitude to a value close to that obtained by Monte Carlo calculations for hard spherocylinders.[79]

At a more fundamental level density functional methods have been employed that go beyond the second virial approximation. The case of hard ellipsoids, for example, has been treated[82] by factorisation of the direct correlation function into translational and orientational parts in the form

$$c(\mathbf{R}-\mathbf{R}',\boldsymbol{\Omega},\boldsymbol{\Omega}') \approx \frac{v_{\mathrm{x}}(\boldsymbol{\Omega},\boldsymbol{\Omega}')}{v_0} c_0\big(|\mathbf{R}-\mathbf{R}'|/d_0;\eta\big) \tag{12.7.23}$$

where $v_{\mathrm{x}}(\boldsymbol{\Omega},\boldsymbol{\Omega}')$ is the excluded volume of two ellipsoids of volume $v_0 = \pi L d^2/6$, $c_0(r)$ is the direct correlation function of a fluid of hard spheres of diameter d_0, chosen such that its volume matches that of the ellipsoid, and $\eta = \rho v_0$. The Percus–Yevick expression (4.4.10) is used for $c_0(r)$ and the free energies of the isotropic and nematic phases are calculated relative to that of the hard-sphere fluid by an angle-dependent generalisation of the exact expression (3.5.23); the free energy of the nematic phase is again obtained by minimisation with respect to a trial orientational distribution function. An interesting feature of the theory is that thermodynamic properties display a prolate–oblate symmetry; thermodynamic properties at a given packing fraction are the same for aspect ratios κ and κ^{-1}, a finding confirmed to a good approximation by Monte Carlo simulations.[83]

The transition between nematic and smectic-A phases of rod-like particles has been studied within density functional theory by imposing a one-dimensional, periodic, modulation of the single-particle density such that $\rho^{(1)}(\mathbf{r},\boldsymbol{\Omega}) = \rho^{(1)}(z,\hat{\mathbf{n}}\cdot\hat{\boldsymbol{\Omega}})$, where $\hat{\mathbf{n}}$ is the common director of the two phases.[84] Calculations are simplified for systems of parallel rods aligned along the director, which show[85] that the transition for this restricted model is continuous for all values of κ. The importance of particle shape is well illustrated by the fact that, unlike the case of parallel spherocylinders, no smectic phase exists for parallel ellipsoids. By scaling all z-coordinates by $1/\kappa$, the spherocylinders can be mapped onto hard spheres, leaving the partition function invariant,[86] and hard spheres cannot form a stable, lamellar phase. The case of freely rotating spherocylinders is much more complicated but density functional methods have been devised to study the stability of the nematic phase with respect to a smectic-A perturbation of the form

$$\delta\rho^{(1)}(\mathbf{R},\boldsymbol{\Omega}) = \Psi(\boldsymbol{\Omega}) \sum_{n=1}^{\infty} c_n \cos(2\pi n z/a) \tag{12.7.24}$$

where $a \approx L + d$ is the periodicity of the density wave.[87] The calculations show that an isotropic–nematic–smectic-A triple point should exist at $\kappa \approx 3.2, \eta \approx 0.46$, in fair agreement with Monte Carlo simulations in which the complete phase diagram of hard spherocylinders in the $\kappa - \eta$ plane was mapped out.[88] Part of the phase diagram is pictured in Figure 12.12, from which it can be seen that

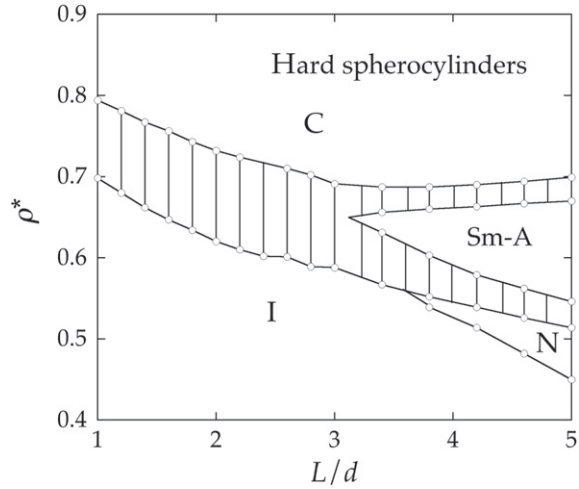

FIGURE 12.12 Part of the phase diagram of hard spherocylinders in the aspect ratio – packing fraction plane, showing the boundaries between isotropic, nematic, smectic-A and ordered crystal phases; $\rho^* = \rho/\rho_{\rm cp}$, where $\rho_{\rm cp}$ is the close-packed density. A plastic crystal phase appears at lower values of κ (not shown). The shaded area is the region of two-phase coexistence. *Redrawn with permission from Ref. 88 © American Institute of Physics.*

a direct transition between isotropic and smectic-A phases is possible for aspect ratios in the range from approximately 3.1 to 3.7. All transitions are first order.[89]

The limit in which $\kappa \to 0$ has received less attention. Early Monte Carlo studies[90] of infinitesimally thin ($\kappa = 0$) discs of diameter d detected a weakly first order, isotropic to nematic transition at a reduced density $\rho^* = Nd^3/V \approx 4.0$. Onsager's theory can be adapted to this case, with

$$v_{\rm x}(\mathbf{\Omega}, \mathbf{\Omega}') = \frac{1}{2}\pi d^3 |\sin\gamma(\mathbf{\Omega}, \mathbf{\Omega}')| \tag{12.7.25}$$

replacing the corresponding term in the functional (12.7.12). Now, however, the virial series is not rapidly convergent and the results of the theory are poor; calculations based on the trial function (12.7.21) lead to a transition that is strongly first order. A more successful approach to the problem of thin, hard platelets is based on the PRISM formalism[91] originally developed for polymer melts (see Section 12.3). Each platelet is assumed to carry a regular, rigid array of ν interaction sites, and the total interaction between two platelets labelled 1 and 2 is a sum of ν^2 site–site pair potentials. If it is assumed that all ν sites are equivalent, which here amounts to neglecting edge effects, the PRISM-OZ relation (12.3.9) between site–site total and direct correlation functions carries over to the case of platelets, with the interaction sites playing the role of monomers and the monomer density replaced by the quantity $\nu\rho$. A change is also required in the definition of the form factor (12.3.10). In the isotropic phase, the conformational average required for flexible polymers is replaced by an orientational

average, i.e.

$$\langle \hat{\omega}_{\alpha\beta} \rangle = \frac{\sin(kr_{\alpha\beta})}{r_{\alpha\beta}} \tag{12.7.26}$$

where $r_{\alpha\beta}$ is the separation of sites α, β on a given platelet. If, in addition, the sites are uniformly distributed over a disc of radius $R_0 = \frac{1}{2}d$, the form factor is

$$\hat{\omega}(k) = \frac{2\nu}{(kR_0)^2}\left(1 - \frac{\mathcal{J}_1(2kR_0)}{kR_0}\right) \tag{12.7.27}$$

where $\mathcal{J}_1(x)$ is the first-order, cylindrical Bessel function which reduces to the Lorentzian function

$$\hat{\omega}(k) \approx \frac{2\nu}{1 + k^2R_0^2} \tag{12.7.28}$$

at both small and large k. For an anisotropic phase with preferential orientation along the z-axis, an approximate, orientation-dependent form factor has been proposed[92] as a generalisation of (12.7.28):

$$\hat{\omega}(k) = \frac{2\nu}{2 + (k_z R_0)^2(1 + 2\mathcal{Q}) + (k_\perp R_0)^2(1 - \mathcal{Q})} \tag{12.7.29}$$

where the subscript $\perp$ refers to the plane orthogonal to the z-axis, and $\mathcal{Q}$ is the nematic order parameter.

With this approximation, an analytic solution of the PRISM-OZ relation (12.3.9) can be derived for infinitesimally thin discs if the Percus–Yevick closure $c(r) = c_0\delta(\mathbf{r})$ is adopted, the parameter $c_0 = \hat{c}(k)$ being determined by the core condition $h(r = 0) = -1$. The compressibility can then be determined from the resulting structure factor via (3.6.11) and the osmotic pressure follows by thermodynamic integration:

$$\frac{\beta P}{\rho} = 1 + 4\pi\rho\left(\frac{R_0'}{\sqrt{2}}\right)^3 + \frac{16}{3}\pi^2\rho^2\left(\frac{R_0'}{\sqrt{2}}\right)^6 \tag{12.7.30}$$

where $R_0' = R_0[(1 - \mathcal{Q})(1 + \mathcal{Q})^{1/2}]^{1/3}$ is an effective platelet radius; R_0' is equal to R_0 in the isotropic phase and vanishes in the fully aligned nematic phase. Despite appearances, (12.7.30) is not a truncated virial expansion. In the isotropic phase the coefficients of the terms of order ρ and ρ^2 are, respectively, $B_2' = \sqrt{2}\pi R_0^3$ and $B_3' = 2\pi^2 R_0^6/3 \approx 6.58R_0^6$, while the corresponding virial coefficients are $B_2 = \pi^2 R_0^3/2$ and $B_3 \approx 10.83R_0^6$.

The free energy for a given density must be minimised with respect to a trial orientational distribution function; the ideal contribution, given by (12.7.6), may be expressed in terms of $\mathcal{Q}$, while the excess part is obtained from the equation of state (12.7.30). Minimisation with respect to $\mathcal{Q}$ shows that the isotropic phase is stable for a reduced density $\rho^* = 8R_0^3\rho \leq 3.12$, while for higher densities a non-zero value of $\mathcal{Q}$ is obtained, corresponding to the onset of nematic

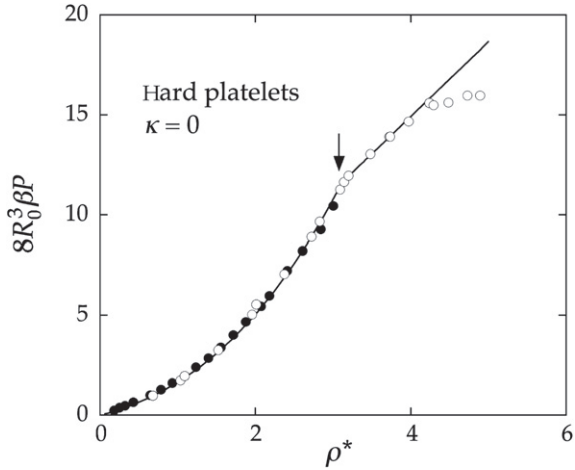

FIGURE 12.13 Osmotic equation of state of a suspension of infinitesimally thin, hard platelets of radius R_0. The points show the results of Monte Carlo calculations[90,93] and the curve is calculated from the PRISM equation (12.7.30); the arrow marks the density at which the isotropic–nematic transition is predicted to occur. From L. Harnau et al., 'A solvable interaction site model for lamellar colloids', *Europhys. Lett.* **53**, 729–734 (2001).

ordering. Figure 12.13 shows a comparison between results of the theory[91] and those obtained by Monte Carlo calculations; the agreement is excellent up to $\rho^* \approx 4$, but the isotropic–nematic transition is predicted to occur at $\rho^* \approx 3.2$ rather than $\rho^* \approx 4.1$.

Although infinitesimally thin platelets can form both isotropic and nematic phases the fact that they occupy zero volume means that no other phases exist. For $\kappa > 0$ we may expect to see the emergence of other phases, including a columnar phase in which the platelets form a hexagonal array of parallel, cylindrical stacks. Monte Carlo calculations[94] for oblate, hard spherocylinders have revealed the existence of isotropic, nematic, columnar and both tilted and aligned crystal phases, with an isotropic–columnar–crystal triple point for κ in the range 0.12–0.13. Overall the phase diagram is similar to that calculated earlier for the related system of cut, hard spheres.[95] The isotropic–nematic transition has been detected experimentally[96] for gibbsite platelets with $\kappa \approx 0.08$.

12.8 CLUSTERING AND GELATION

We have seen in earlier sections that stabilised suspensions of colloidal particles behave much like simple liquids, with the added freedom that the amplitude and range of the effective interactions can be tuned by changes, for example, in the concentration of non-adsorbing polymers or of added salt. Tunability of the interaction leads to a greater variety of phase behaviour than is seen in the phase diagram of simple liquids, as Figure 12.9 illustrates. Over the last decade

much progress has been made in the design and synthesis of colloidal particles involving competing interactions or specific surface patterns; these systems display even richer behaviour, such as clustering, microphase separation and gelation. Gelation corresponds to the formation of a space-spanning, fractal network of particles that represents a low-density, disordered phase with solid-like elastic properties. Unlike the gelation of polymers, which is an irreversible process characterised by the formation of cross-linking chemical bonds, colloidal systems can form physical, reversible gels because the bonds due to colloid–colloid interactions are typically of the order of a few $k_B T$. Here we describe briefly two examples that have been studied by a combination of experiment, simulation and theory.[97,98]

We first consider colloids with competing, spherically symmetric interactions, involving a hard core, a short-range attraction and a long-range repulsion. The attraction may be induced by non-adsorbing polymers acting as depletant, while the repulsion arises from a residual surface charge screened by microions. If the solvent is weakly polar, the concentration of disassociated ions is low, and the screening length $\lambda_D = k_D^{-1}$ (see (10.2.15)) may be much larger than the range of the depletion potential, which is roughly equal to the radius of gyration of the depletant. Fluorescence microscopy has shown that at low colloid volume fractions ($\eta < 0.1$) the particles form an equilibrium cluster phase; as the density is increased, the clusters are seen to grow and become increasingly anisotropic, tending ultimately to aggregate and thereby to form a percolating, dynamically arrested network, in other words a gel.[100] Reversible cluster formation has also been observed in small-angle X-ray and neutron scattering experiments on colloid–polymer mixtures and globular protein solutions, in which a well-defined pre-peak appears in the static structure factor at a wavenumber k_c lying well below that of the main peak at $k \approx 2\pi/d$, where d is the particle diameter; the pre-peak arises from cluster–cluster correlations.[99] A similar pre-peak, the amplitude of which grows rapidly as the temperature is lowered, has been seen in molecular dynamics simulations of a simple model which combines a generalised, $2\ell - \ell$, Lennard-Jones potential, with $\ell = 100$, and a long-range repulsion of Yukawa form. The high value chosen for ℓ ensures the attraction is very short ranged[101]; the resulting interaction between clusters is therefore both long ranged and repulsive. At very low densities this leads to the formation of a cluster glass as the temperature is lowered. If η is greater than about 0.12, the effect of reducing the temperature is different; the clusters first form a percolating network, which then evolves into a reversible gel. Dynamical arrest in the gel is characterised by an intermediate scattering function which resembles that observed at the kinetic glass transition of supercooled liquids, shown in Figure 8.12, with non-ergodic behaviour appearing at sufficiently low temperatures.

The balance between short-range attraction and long-range repulsion, which depends sensitively on their relative range, means that formation of the cluster phase preempts condensation into a colloidal liquid phase. Simple calculations

show that the internal energy of a spherical cluster goes through a minimum for a finite aggregation number.[101] The cluster phase is therefore stable, since the entropic contribution to the free energy will always favour small clusters.

Most theoretical calculations are based on the two-Yukawa model, consisting of hard spheres of diameter d with short-range attractive and long-range repulsive terms, both of Yukawa form, i.e.

$$\begin{aligned} v(x) &= \infty, \quad x < 1 \\ &= -\frac{\epsilon}{x}\big(\exp[-z_1(x-1)] - A\exp[-z_2(x-1)]\big), \quad x > 1 \end{aligned} \tag{12.8.1}$$

where $x = r/d, \epsilon$ (a positive quantity) is a characteristic energy, z_1 and z_2 are the dimensionless range parameters of the attractive and repulsive contributions (with $z_2 < z_1$) and $0 < A < 1$; the depth of the potential well at contact is $-\epsilon(1 - A)$. Physically, $z_1 \approx d/R_g$ and $z_2 \approx d/\lambda_D$. Figure 12.14 shows the form of the potential for typical choices of the parameters A, z_1 and z_2. The relative importance of the attractive and repulsive components of the potential (12.8.1) may be quantified by the integral

$$I = 4\pi \int_1^\infty v(x)x^2\,\mathrm{d}x = -4\pi\epsilon\left(\frac{z_1+1}{z_1^2} - A\frac{z_2+1}{z_2^2}\right) \tag{12.8.2}$$

For $A = 0$, the attraction leads to a first-order, gas–liquid transition. Within the mean field theory of Section 5.7 the critical temperature is largely determined by the value of the quantity $a = -\frac{1}{2}I$. As the long-range repulsion is switched

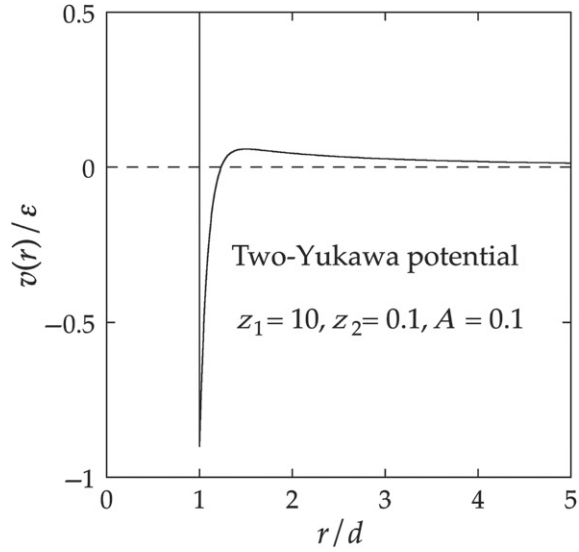

FIGURE 12.14 A two-Yukawa potential for typical values of the parameters A, z_1 and z_2.

on, a decreases and T_c is expected to fall.[102] The position of the prepeak in the structure factor, which signals the aggregation of particles into clusters, can be calculated within the random phase approximation (3.5.17) for the direct correlation function[103,104]:

$$\hat{c}(q) = \hat{c}_d(q) - \beta\hat{v}(q) \tag{12.8.3}$$

Here $q = kd$, $\hat{c}_d(q)$ is the Fourier transform of the hard-sphere direct correlation function, which is well approximated by the Percus–Yevick expression (4.4.10), and $\hat{v}(q)$ is the Fourier transform of the pair potential, with the continuous part extrapolated inside the hard core. Accordingly, $S(q) = 1/D(q)$, where, from (3.6.10) and (12.8.3):

$$\begin{aligned} D(q) &= 1 - \rho^*\left[\hat{c}_d(q) - \beta\hat{v}(q)\right] \\ &= 1 - \rho^*\left(\hat{c}_d(q) + \frac{4\pi\beta\epsilon_1}{z_1^2 + q^2} - \frac{4\pi\beta\epsilon_2}{z_2^2 + q^2}\right) \end{aligned} \tag{12.8.4}$$

where $\rho^* = \rho d^3, \epsilon_1 = \epsilon\exp(z_1)$ and $\epsilon_2 = A\epsilon\exp(z_2)$; a peak in $S(q)$ corresponds to a minimum in $D(q)$. We are interested in the low-q region, $q \ll 2\pi$ (2π is roughly the position of the main peak); in that range the hard-sphere structure factor is very flat. Thus $\hat{c}_d(q)$ is almost independent of q and therefore contributes little to the extremum condition, $\delta D(q)/\delta q = 0$, from which it follows that

$$\frac{8\pi\beta\epsilon_1 q}{\left(z_1^2 + q^2\right)^2} - \frac{8\pi\beta\epsilon_2 q}{\left(z_2^2 + q^2\right)^2} = 0 \tag{12.8.5}$$

Equation (12.8.5) has one root, $q = 0$, corresponding to a minimum in $S(q)$, and another given by

$$q_c = \frac{\left(z_1^2 - z_2^2\right)^{1/2}}{\alpha - 1} \tag{12.8.6}$$

where $\alpha = \left(\epsilon_1/\epsilon_2\right)^{1/2} > 1$, at which the cluster prepeak appears. Note that q_c is independent of density, but the amplitude of the peak depends on both density and temperature. The value of $S(q_c)$ will diverge as the temperature is reduced at constant density and the locus of points in the density–temperature plane at which this occurs is called the λ-line. The λ-line plays a role analogous to that of the spinodal line of the gas–liquid transition, along which $S(q)$ diverges at $q = 0$. Its relation to the gas–liquid coexistence curve and spinodal for a two-Yukawa fluid is illustrated in Figure 12.15, where it encloses a large portion of the density–temperature plane above the critical temperature.[104] Along the spinodal line the fluid becomes unstable against macroscopic phase separation; along the λ-line it becomes unstable against density modulations of mesoscopic wavelength $\lambda = 2\pi/q_c$, leading to a microphase transition into a spatially ordered, cluster phase. A one-dimensional modulation, for example, leads to

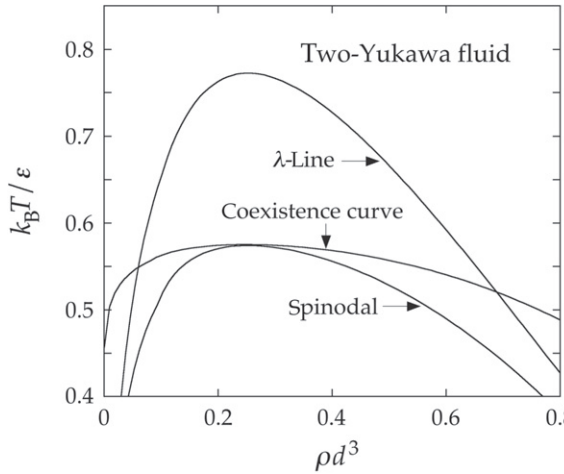

FIGURE 12.15 The λ-line, liquid–gas coexistence curve and spinodal line for a typical two-Yukawa fluid. From A.J. Archer et al., 'Theory for the phase behaviour of a colloidal fluid with competing interactions', *J. Phys. Condens. Matter* **20**, 41506 (2008). *© IOP Publishing 2008. Reproduced by permission of IOP Publishing. All rights reserved.*

a lamellar phase. The response to a modulation of that form has been studied in detail by mean field, density functional theory based on the free energy functional (3.4.10), but without the correlation term, and the local density approximation (6.2.5) for the hard-sphere contribution.[104]

Examples of the structure factor obtained by solution of a thermodynamically consistent integral equation[105] are compared with Monte Carlo data in Figure 12.16 for the cases when $z_1 = 10, z_2 = 0.10$ and $A = 0.01$ or 0.10. At the larger value of A the intensity of the pre-peak increases rapidly as the temperature is lowered, while for $A = 0.01$ the pre-peak appears at a significantly smaller wavenumber, indicative of the formation of increasingly larger clusters as the long-range repulsion is weakened.

A second type of model system suitable for the study of gelation is that of patchy particles of functionality f, already described in Section 11.10, in which a hard-sphere core has a pattern of f interaction sites on its surface.[98,106] Sites on different particles interact via a short-range, attractive potential, which in practice is taken to be of square-well form. If f is not too large and the sites are regularly distributed, it is possible to choose the range of the square-well interaction to be sufficiently short that at most only one bond can form between any two particles and no more than one particle can bond to a given site; this implies that f is the maximum number of bonds that a particle can form. Figure 11.8 shows how this comes about in the simplest case, when $f = 2$. Regular patterns of surface sites for which calculations have been made[107] include two diametrically opposite sites ($f = 2$) (as in the Figure), an equilateral, triangular distribution ($f = 3$), a tetrahedral distribution ($f = 4$) and the vertices

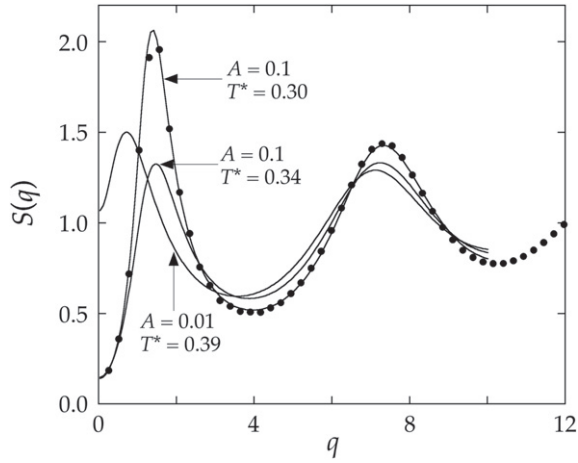

FIGURE 12.16 Structure factor of the two-Yukawa model at different reduced temperatures $T = k_B T/\epsilon$ and different values of the parameter A. The points show the results of Monte Carlo calculations and the curves are calculated from a thermodynamically consistent integral equation. The prepeak at $q < 2$ is a signal of cluster formation. *Redrawn with permission from Ref. 105* © *American Institute of Physics.*

of two face-sharing tetrahedra ($f = 5$). Larger patterns can be used, such as an octahedral distribution for $f = 6$, but as f increases a regular distribution of sites leads to less directional, quasi-isotropic interactions between particles. Mean, non-integral functionalities can be studied by taking binary mixtures of components having different values of f, for which $\bar{f} = xf_1 + (1 - x)f_2$. The case $f_1 = 2, f_2 = 3$ is of particular interest[108] as it allows $\bar{f}$ to vary continuously towards 2^+. The $f = 2$ model, where each particle interacts with at most two neighbours, can lead only to the formation of independent, linear chains. Bulk condensation into a liquid phase is inhibited, while gelation into a volume-spanning, cross-linked network is impossible, since branching would require at least some of the particles to be of higher functionality.

Figure 12.17 shows the phase diagrams of monodisperse systems of patchy particles for $f = 3, 4$ and 5, obtained by Monte Carlo calculations, together with the results[107] of Wertheim's thermodynamic perturbation theory, also described in Section 11.10. The agreement is fair for $f = 3$ but rapidly deteriorates as the functionality increases. What both sets of results show, however, is that the critical temperature and density decrease rapidly with f and the liquid–gas coexistence curve gradually shrinks towards the lower, left-hand corner of the density–temperature plane. This is confirmed by the spinodal curves calculated[108] from Wertheim's theory for a binary mixture of mean valence $2 < \bar{f} < 3$. As surmised earlier, gas–liquid phase separation disappears at $f = 2$.

The coexistence curves for $\bar{f} \leq 3$ show that the liquid state occupies a much wider range of density than is the case for simple liquids. These low density,

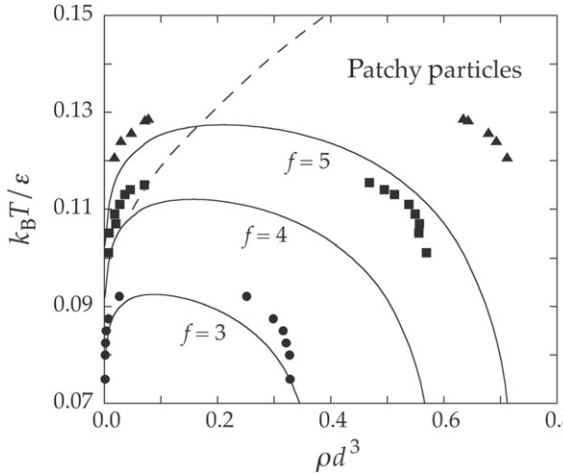

FIGURE 12.17 Phase diagrams for patchy particles of different functionalities. The curves show the predictions of Wertheim's theory, described in Section 11.10, and the points are the results of Monte Carlo calculations. The broken curve is the percolation line for $f = 4$. *Redrawn with permission from Ref. 107* © *American Institute of Physics.*

equilibrium states are referred to as 'empty liquids', since the particles occupy only a very small fraction of the available volume. For example, the critical packing fraction is approximately 0.070 for $f = 3$ and 0.046 for $\bar{f} = 2.5$. Thus, when a suspension of low-functionality, patchy particles is cooled along an isochore to the right of the coexistence curve, particles begin to aggregate into mostly linear clusters. Since phase separation is avoided, the liquid-like suspension remains in equilibrium throughout and the thermodynamic path is reversible down to low temperatures. Beyond a percolation threshold the system forms a transient, space-filling network. Figure 12.17 includes the percolation line predicted[109] by Wertheim's theory for $f = 4$. This merges into the coexistence curve at low density; the behaviour for $f = 3$ and $f = 4$ is qualitatively similar.

Thermal fluctuations in fluids consisting of patchy particles will lead to frequent breakage and recombination of the bonds between particles, so that bonded networks continually switch from percolating to disconnected configurations, thereby ensuring that ergodicity is maintained. The bond lifetime τ_B can be expected to satisfy an Arrhenius law, $\tau_B \sim \exp(\beta\epsilon)$, where ϵ is a measure of the strength of the bonding potential. When τ_B exceeds the experimental time scale, reversible gelation occurs, an effect similar to the glass transition in denser fluids. The difference is that at high densities arrested dynamics are a consequence of the caging of tightly packed particles, whereas in the low-density liquids formed by patchy particles dynamical arrest arises from the long-lived bonding.[110]

Reversible network formation and gelation at low packing fractions are features that are not peculiar to low-functionality, patchy particles. They may also result from the long-range, dipolar interactions typical of ferrofluids. Spherical particles with embedded point particles, of which the simplest example is that of dipolar hard spheres, favour head-to-tail configurations. This leads to the formation of linear chains at low temperatures,[111] as in the case of patchy particles with $f = 2$. However, slightly elongated particles that carry extended rather than point dipoles favour branching of the chains, which can then interconnect to form a three-dimensional network. This has been demonstrated in the case of dipolar dumbbells, similar to the model pictured in Figure 1.5 except that the charges are now q and $-q$ and the atoms are represented by repulsive, soft spheres. The point dipole limit is recovered in the limit in which the bondlength $L \to 0$ and $q \to \infty$ at a fixed value of the dipole moment $\mu = qL$. Molecular dynamics calculations[112] have found clear evidence of clustering, branching, network formation, percolation, gel formation and dynamical arrest at packing fractions as low as 0.02, behaviour similar to that observed for patchy particles of low functionality. Other simulations have revealed no sign of a gas–liquid transition in point dipolar systems[113]; though contrary to earlier speculation, this is consistent with results obtained for patchy particles with $f = 2$.

12.9 THE FOKKER–PLANCK AND SMOLUCHOWSKI EQUATIONS

Earlier parts of this chapter were largely concerned with the calculation of static properties based on coarse-graining strategies that lead to effective interactions between the mesoscopic particles that make up the systems of interest. We turn now to the problem of describing the dynamics of colloidal particles on the mesoscopic time scale by a coarse graining in time. The traditional approach to the problem is a stochastic one,[114,115] exploited more than a century ago by Einstein, Langevin and Smoluchowski. The underlying assumption is that there exists a separation of time scales which allows the fast processes to be treated in an averaged way. A classic example is provided by the Langevin equation introduced in Section 7.3, which yields an expression for the velocity autocorrelation function of a brownian particle. In this section we show how, starting from first principles, an expression can be obtained for the time evolution of the single-particle distribution function $f^{(1)}(\mathbf{R}, \mathbf{P}; t)$ of a brownian particle, of mass M and diameter Σ, suspended in a fluid consisting of particles of much smaller mass m and diameter σ. The result is called the Fokker–Planck or Kramers equation.

On the microscopic level the shortest time scale is the Enskog mean collision time $\tau_E = 1/\Gamma_E$, defined by (7.2.19), while a typical collective time scale is the time $\tau_s = \Sigma/c_s$ required for a sound wave of velocity c_s to propagate

over a distance of order Σ. For a solvent such as water and a colloidal particle of diameter of order 10^2 nm, $\tau_{\mathrm{E}} \approx 10^{-13}$ s, while $\tau_s \approx 10^{-11}$ s. Relevant mesoscopic time scales are the time $\tau_{\mathrm{B}} = 1/\xi$ over which the velocity of a brownian particle relaxes, where ξ is the friction coefficient of Langevin theory (see (7.3.6)), and a configurational relaxation time τ_{c}, which is the time required for an isolated brownian particle to diffuse over a distance equal to its diameter. An estimate of τ_{c} in terms of ξ is given by the Einstein relation (7.3.17):

$$\tau_{\mathrm{c}} = \frac{\Sigma^2}{D} = \frac{\xi M \Sigma^2}{k_{\mathrm{B}} T} \tag{12.9.1}$$

At room temperature, for typical values of M, Σ and ξ, we find that $\tau_{\mathrm{B}} \approx 10^{-9}$ s and $\tau_{\mathrm{c}} \approx 10^{-3}$ s. Thus the assumption of a clear separation of microscopic ($\tau_{\mathrm{E}}, \tau_{\mathrm{s}}$) and mesoscopic ($\tau_{\mathrm{B}}, \tau_{\mathrm{c}}$) time scales appears to be well justified.

The derivation of the Fokker–Planck equation starts from the Liouville equation (2.1.9) for the phase space probability density of a system of N bath particles and a single brownian particle. It relies on an expansion of the distribution function in powers of the natural small parameter $\epsilon = (m/M)^{1/2}$, which is the ratio of the thermal velocities of the brownian and bath particles. The task is nor a straightforward one, since a conventional perturbation expansion leads to secular divergence of the solution at sufficiently long times, irrespective of how small ϵ may be. A similar difficulty is encountered even in the simple case of a weakly damped harmonic oscillator when expansion is made in powers of the damping coefficient.[116] In each case, however, the problem can be overcome by use of a 'multiple time scale' method, first applied to the problem of brownian motion by Cukier and Deutch.[117]

The Hamiltonian of the $(N+1)$-particle system is

$$\mathcal{H} = \frac{P^2}{2M} + \sum_{i=1}^{N} \frac{p_i^2}{2m} + V_N\left(\mathbf{r}^N\right) + \Phi\left(\mathbf{R}, \mathbf{r}^N\right) \tag{12.9.2}$$

where V_N is the total interaction energy of the N bath particles and Φ is the potential energy of the bath particles in the field of a brownian particle placed at $\mathbf{R}$. The Liouville operator splits naturally into 'bath' and 'brownian' terms:

$$\mathcal{L} = \mathcal{L}_{\mathrm{b}} + \mathcal{L}_{\mathrm{B}} \tag{12.9.3}$$

with

$$\begin{aligned} \mathcal{L}_{\mathrm{b}} &= -i \sum_{i=1}^{N} \left(\frac{\mathbf{p}_i}{m} \cdot \frac{\partial}{\partial \mathbf{r}_i} + \mathbf{f}_i \cdot \frac{\partial}{\partial \mathbf{p}_i} \right) \\ \mathcal{L}_{\mathrm{B}} &= -i \left(\frac{\mathbf{P}}{M} \cdot \frac{\partial}{\partial \mathbf{R}} + \mathbf{F}_{\mathrm{B}} \cdot \frac{\partial}{\partial \mathbf{P}} \right) \end{aligned} \tag{12.9.4}$$

Here $\mathbf{f}_i = -\partial(V_N + \Phi)/\partial \mathbf{r}_i$ is the force acting on bath particle i and $\mathbf{F}_{\mathrm{B}} = -\partial \Phi / \partial \mathbf{R}$ is the force exerted on the brownian particle by particles of

the bath. The Liouville equation for the phase space probability density of the system of $(N+1)$ particles is therefore

$$\frac{\partial}{\partial t} f^{[N+1]}(\mathbf{B}, \mathbf{b}^N; t) = -i\big(\mathcal{L}_\mathrm{b} + \mathcal{L}_\mathrm{B}\big) f^{[N+1]}(\mathbf{B}, \mathbf{b}^N; t) \tag{12.9.5}$$

where we have used the short-hand notation $\mathbf{B} \equiv \{\mathbf{R}, \mathbf{P}\}$ and $\mathbf{b}^N \equiv \{\mathbf{r}^N, \mathbf{p}^N\}$ to represent, respectively, the phase space coordinates of the brownian and bath particles. Since ϵ is treated as a perturbation, it proves useful to express the momentum of the brownian particle in scaled form as $\mathbf{P}' = \epsilon\mathbf{P}$, in which case the kinetic energy $P^2/2M$ becomes $P'^2/2m$ and the brownian term in the Liouville operator scales as

$$\mathcal{L}_\mathrm{B} = -i\epsilon\left(\frac{\mathbf{P}'}{m}\cdot\frac{\partial}{\partial\mathbf{R}} + \mathbf{F}_\mathrm{B}\cdot\frac{\partial}{\partial\mathbf{P}'}\right) \equiv \epsilon\mathcal{L}'_\mathrm{B} \tag{12.9.6}$$

The single-particle distribution function $f_\mathrm{B}(\mathbf{B}, t) \equiv f^{[1]}(\mathbf{R}, \mathbf{P}', t)$ is the integral of $f^{[N+1]}$ over the coordinates and momenta of the bath particles and its time evolution is similarly obtained by integration of the Liouville equation (12.9.5):

$$\begin{aligned}\frac{\partial f_\mathrm{B}(\mathbf{B}, t)}{\partial t} &= \int \big(-i\mathcal{L}_\mathrm{b}\big) f^{[N+1]}(\mathbf{B}, \mathbf{b}^N; t)\, \mathrm{d}\mathbf{b}^N \\ &\quad + \epsilon\int \big(-i\mathcal{L}'_\mathrm{B}\big) f^{[N+1]}(\mathbf{B}, \mathbf{b}^N; t)\, \mathrm{d}\mathbf{b}^N \\ &= -\epsilon\frac{\mathbf{P}'}{m}\cdot\frac{\partial}{\partial\mathbf{R}} f_\mathrm{B}(\mathbf{B}, t) - \epsilon\int \mathbf{F}_\mathrm{B}\cdot\frac{\partial}{\partial\mathbf{P}'} f^{[N+1]}(\mathbf{B}, \mathbf{b}^N; t)\, \mathrm{d}\mathbf{b}^N\end{aligned} \tag{12.9.7}$$

The term involving the operator $\mathcal{L}_\mathrm{b}$ in the first equality vanishes for the same reasons as those invoked in passing from (2.1.17) to (2.1.18) in the derivation of the BBGKY hierarchy.

The multiple time scale method[116,118] involves the introduction of an auxiliary distribution function, $f_\epsilon^{[N+1]}(\mathbf{B}, \mathbf{b}^N; t_0, t_1, t_2, \ldots)$, which is a function of multiple time variables $t_0, t_1, t_2, \ldots$, corresponding to increasingly long time scales. The equation that describes the time evolution of the auxiliary function is then similar to (12.9.5) except that the single time derivative is replaced by a sum of derivatives with respect to $t_0, t_1, t_2, \ldots$:

$$\left(\frac{\partial}{\partial t_0} + \epsilon\frac{\partial}{\partial t_1} + \epsilon^2\frac{\partial}{\partial t_2} + \cdots\right) f_\epsilon^{[N+1]} = -i\big(\mathcal{L}_\mathrm{b} + \epsilon\mathcal{L}'_\mathrm{B}\big) f_\epsilon^{[N+1]} \tag{12.9.8}$$

This equation can be solved perturbatively by expansion of $f_\epsilon^{[N+1]}$ in powers of ϵ:

$$f_\epsilon^{[N+1]} = f_{\epsilon 0}^{[N+1]} + \epsilon f_{\epsilon 1}^{[N+1]} + \epsilon^2 f_{\epsilon 2}^{[N+1]} + \cdots \tag{12.9.9}$$

The physical distribution function $f^{[N+1]}$ is eventually recovered by relating the quantities $t_0, t_1, t_2, \ldots$ to the physical time t via the rule

$$t_0 = t,\ t_1 = \epsilon t,\ t_2 = \epsilon^2 t,\ \ldots,\ t_n = \epsilon^n t \tag{12.9.10}$$

The analogous auxiliary distribution function for the brownian particle, $f_{\mathrm{B}\epsilon}(\mathbf{B}; t_0, t_1, t_2, \ldots)$, satisfies the generalisation to multiple time variables of (12.9.7):

$$\begin{aligned}\left(\frac{\partial}{\partial t_0} + \epsilon\frac{\partial}{\partial t_1} + \epsilon^2\frac{\partial}{\partial t_2} + \cdots\right) f_{\mathrm{B}\epsilon} \\ = -\epsilon\frac{\mathbf{P}'}{m}\cdot\frac{\partial}{\partial \mathbf{R}} f_{\mathrm{B}\epsilon} - \epsilon\int \mathbf{F}_{\mathrm{B}}\cdot\frac{\partial}{\partial \mathbf{P}'} f_{\epsilon}^{[N+1]}\,\mathrm{d}\mathbf{b}^N\end{aligned} \tag{12.9.11}$$

Term by term integration of (12.9.9) shows that $f_{\mathrm{B}\epsilon}$ can be expanded in the form

$$f_{\mathrm{B}\epsilon} = f_{\mathrm{B}0} + \epsilon f_{\mathrm{B}1} + \epsilon^2 f_{\mathrm{B}2} + \mathcal{O}\left(\epsilon^3\right) \tag{12.9.12}$$

The crucial difference between (12.9.9) and a conventional perturbation expansion of $f^{[N+1]}$ itself is the fact that the auxiliary function has a physical meaning only along the so-called physical line defined by (12.9.10). We are therefore free to impose whatever boundary conditions are needed to ensure that the expansion is free of secular divergences at successive powers of ϵ; the same is true of the expansion of $f_{\mathrm{B}\epsilon}$.

We now restrict the discussion to order ϵ^2, retaining only the three time variables t_0, t_1 and t_2. Then, by substituting (12.9.9) and (12.9.12) in (12.9.11) and equating coefficients of equal powers of ϵ up to $\mathcal{O}\left(\epsilon^2\right)$, we arrive at the following results.

To zeroth order in ϵ: Equation (12.9.11) implies that

$$\frac{\partial f_{\mathrm{B}0}}{\partial t_0} = 0 \tag{12.9.13}$$

and hence that $f_{\mathrm{B}0} = f_{\mathrm{B}0}\left(\mathbf{R}, \mathbf{P}'; t_1, t_2\right)$. Similarly, it follows from (12.9.8) that

$$\frac{\partial f_{\epsilon 0}^{[N+1]}}{\partial t_0} = -i\mathcal{L}_{\mathrm{b}} f_{\epsilon 0}^{[N+1]} \tag{12.9.14}$$

Since the equilibrium, N-particle phase space probability density of the bath particles in the presence of the brownian particle at $\mathbf{R}$ satisfies the relation

$$i\mathcal{L}_{\mathrm{b}} f_0^{[N]}(\mathbf{b}^N|\mathbf{R}) = 0 \tag{12.9.15}$$

where $f_0^{[N]}$ is given by a minor generalisation of (2.3.1), the solution to (2.9.14) is simply

$$f_{\epsilon 0}^{[N+1]} = f_{\mathrm{B}0}(\mathbf{R}, \mathbf{P}'; t_1, t_2) f_0^{[N]}(\mathbf{b}^N|\mathbf{R}) \tag{12.9.16}$$

We can now exploit the freedom of choice of boundary conditions on the auxiliary function $f_{\mathrm{B}\epsilon}$ by imposing the initial condition that

$$f_{\mathrm{B}\epsilon}(\mathbf{R},\mathbf{P}';t_0=0,t_1,t_2)=f_{\mathrm{B}0}(\mathbf{R},\mathbf{P}';t_1,t_2) \tag{12.9.17}$$

which in turn implies that

$$f_{\mathrm{B}n}(\mathbf{R},\mathbf{P}';t_0=0,t_1,t_2)=0,\qquad n=1,2 \tag{12.9.18}$$

To first order in ϵ: Equations (12.9.8) and (12.9.11) reduce to

$$\frac{\partial f_{\epsilon 1}^{[N+1]}}{\partial t_0}+\frac{\partial f_{\epsilon 0}^{[N+1]}}{\partial t_1}=-i\mathcal{L}_{\mathrm{b}}f_{\epsilon 1}^{[N+1]}-i\mathcal{L}'_{\mathrm{B}}f_{\epsilon 0}^{[N+1]} \tag{12.9.19}$$

and

$$\frac{\partial f_{\mathrm{B}1}}{\partial t_0}+\frac{\partial f_{\mathrm{B}0}}{\partial t_1}=\int(-i\mathcal{L}'_{\mathrm{B}})f_{\epsilon 0}^{[N+1]}\,\mathrm{d}\mathbf{b}^N \tag{12.9.20}$$

Equations (12.9.13) and (12.9.16) show that $f_{\mathrm{B}0}$ and $f_{\epsilon 0}^{[N+1]}$ are both independent of t_0. To avoid secular growth of $f_{\mathrm{B}1}$ in (12.9.20) it is therefore necessary to impose the condition that

$$\frac{\partial f_{\mathrm{B}0}}{\partial t_1}+\int i\mathcal{L}'_{\mathrm{B}}f_{\epsilon 0}^{[N+1]}\,\mathrm{d}\mathbf{b}^N=0 \tag{12.9.21}$$

which implies that $\partial f_{\mathrm{B}1}/\partial t_0=0$ for all t_0. Combined with the initial condition (12.9.18) this in turn implies that $f_{\mathrm{B}1}$ is identically zero:

$$f_{\mathrm{B}1}(\mathbf{R},\mathbf{P}';t_0,t_1,t_2)\equiv 0 \tag{12.9.22}$$

We therefore focus on the time evolution of $f_{\mathrm{B}0}$. Substitution of (12.9.16) in the right-hand side of (12.9.21) and use of the definition (12.9.6) of $\mathcal{L}'_{\mathrm{B}}$ gives

$$\left(\frac{\partial}{\partial t_1}+\frac{\mathbf{P}'}{m}\cdot\frac{\partial}{\partial\mathbf{R}}\right)f_{\mathrm{B}0}(\mathbf{R},\mathbf{P}';t_1,t_2)=0 \tag{12.9.23}$$

Comparison with (7.7.13) shows that on the time scale t_1 the evolution of the distribution function of the brownian particle is the same as that of an ideal gas. Equation (12.9.19) can now be rearranged as

$$\begin{aligned}\left(\frac{\partial}{\partial t_0}+i\mathcal{L}_{\mathrm{b}}\right)f_{\epsilon 1}^{[N+1]}&=-\left(\frac{\partial}{\partial t_1}+i\mathcal{L}'_{\mathrm{B}}\right)f_{\epsilon 0}^{[N+1]}\\&=-\mathbf{F}_{\mathrm{B}}\cdot\left(\frac{\beta\mathbf{P}'}{m}+\frac{\partial}{\partial\mathbf{P}'}\right)f_{\mathrm{B}0}f_0^{[N]}\end{aligned} \tag{12.9.24}$$

which has the formal solution

$$\begin{aligned}&f_{\epsilon 1}^{[N+1]}(\mathbf{R},\mathbf{P}',\mathbf{b}^N;t_0,t_1,t_2)\\&\quad=-\int_0^{t_0}\mathrm{d}s\,\exp(-i\mathcal{L}_{\mathrm{b}}s)\mathbf{F}_{\mathrm{B}}\cdot\left(\frac{\beta\mathbf{P}'}{m}+\frac{\partial}{\partial\mathbf{P}'}\right)\\&\qquad\times f_{\mathrm{B}0}(\mathbf{R},\mathbf{P}';t_1,t_2)f_0^{[N]}(\mathbf{b}^N|\mathbf{R})\end{aligned} \tag{12.9.25}$$

That this is correct may be checked by direct substitution in (12.9.24).

To second order in ϵ: Equations (12.9.11) and (12.9.22) can be combined to give

$$\frac{\partial f_{\mathrm{B}2}}{\partial t_0} + \frac{\partial f_{\mathrm{B}0}}{\partial t_2} = -\int i\mathcal{L}'_{\mathrm{B}} f_{\epsilon 1}^{[N+1]}\, \mathrm{d}\mathbf{b}^N \tag{12.9.26}$$

Since $f_{\mathrm{B}0}$ is independent of t_0, secular growth is again suppressed by setting $\partial f_{\mathrm{B}2}/\partial t_0 = 0$. On substituting the solution (12.9.25) for $f_{\epsilon 1}^{[N+1]}$ in (12.9.26) we obtain a closed equation for the evolution of $f_{\mathrm{B}0}(\mathbf{R}, \mathbf{P}'; t_1, t_2)$:

$$\begin{aligned}\frac{\partial f_{\mathrm{B}0}}{\partial t_2} = \lim_{t_0\to\infty} \int \mathrm{d}\mathbf{b}^N\, f_0^{[N]}(\mathbf{b}^N|\mathbf{R}) i\mathcal{L}'_{\mathrm{B}} \\ \times \int_0^{t_0} \mathrm{d}s \exp\left(-i\mathcal{L}_{\mathrm{b}} s\right)\mathbf{F}_{\mathrm{B}} \cdot \left(\frac{\beta\mathbf{P}'}{m} + \frac{\partial}{\partial \mathbf{P}'}\right) f_{\mathrm{B}0}\end{aligned} \tag{12.9.27}$$

where the limit $t_0 \to \infty$ can be taken because $f_{\mathrm{B}0}$ is independent of t_0. Substitution for $\mathcal{L}'_{\mathrm{B}}$ from (12.9.6) and use of (2.1.14) for the time evolution of the dynamical variable $\mathbf{F}_{\mathrm{B}}$, (12.9.27) shows that

$$\begin{aligned}\frac{\partial f_{\mathrm{B}0}}{\partial t_2} &= \lim_{t_0\to\infty} \int_0^{t_0} \mathrm{d}s \left\langle i\mathcal{L}'_{\mathrm{B}} \mathbf{F}_{\mathrm{B}}(-s)\right\rangle_{\mathrm{bath}} \cdot \left(\frac{\beta\mathbf{P}'}{m} + \frac{\partial}{\partial \mathbf{P}'}\right) f_{\mathrm{B}0} \\ &= \frac{1}{3}\int_0^{\infty} \mathrm{d}s \left\langle \mathbf{F}_{\mathrm{B}} \cdot \mathbf{F}_{\mathrm{B}}(-s)\right\rangle_{\mathrm{bath}} \frac{\partial}{\partial \mathbf{P}'} \cdot \left(\frac{\beta\mathbf{P}'}{m} + \frac{\partial}{\partial \mathbf{P}'}\right) f_{\mathrm{B}0}\end{aligned} \tag{12.9.28}$$

where $\langle \cdots \rangle_{\mathrm{bath}}$ denotes an equilibrium average over the phase space variables of the bath particles in the external field of the brownian particle.

Bringing together the results to first and second order in ϵ embodied in (12.9.23) and (12.9.28), returning both to physical time via the relation (12.9.10) and to the original momentum variable $\mathbf{P}$, we arrive finally at the Fokker–Planck equation for $f_{\mathrm{B}}(\mathbf{R}, \mathbf{P}; t)$:

$$\begin{aligned}\frac{\partial f_{\mathrm{B}}(\mathbf{R}, \mathbf{P}; t)}{\partial t} &= \left(\epsilon \frac{\partial}{\partial t_1} + \epsilon^2 \frac{\partial}{\partial t_2}\right) f_{\mathrm{B}0}(\mathbf{R}, \mathbf{P}; t_1, t_2)\Big|_{t_1=\epsilon t,\, t_2=\epsilon^2 t} \\ &= \left[-\frac{\mathbf{P}}{M} \cdot \nabla_{\mathbf{R}} + \xi \nabla_{\mathbf{P}} \cdot \left(\mathbf{P} + Mk_{\mathrm{B}}T\nabla_{\mathbf{P}}\right)\right] f_{\mathrm{B}}(\mathbf{R}, \mathbf{P}; t)\end{aligned} \tag{12.9.29}$$

where the friction coefficient ξ is given by the integral of the autocorrelation function of the force exerted on the brownian particle by the bath:

$$\xi = \frac{\beta}{3M}\int_0^{\infty} \left\langle \mathbf{F}_{\mathrm{B}} \cdot \mathbf{F}_{\mathrm{B}}(-s)\right\rangle_{\mathrm{bath}} \mathrm{d}s \tag{12.9.30}$$

The friction coefficient has the same form as that derived from the Langevin equation in Section 7.3 except that the random force in (7.3.8) is replaced by the microscopic force $\mathbf{F}_{\mathrm{B}}$.

The Fokker–Planck equation is commonly written in terms of the velocity $\mathbf{V} = \mathbf{P}/M$ rather than momentum. It is also straightforward to generalise its derivation to the inhomogeneous case in which an external force field $\mathbf{F}_{\text{ext}}(\mathbf{R})$ acts on the particle as well as the force due to the bath. With these modifications (12.9.29) takes the from

$$\left(\frac{\partial}{\partial t} + \mathbf{V}\cdot\nabla_{\mathbf{R}} + \frac{\mathbf{F}_{\text{ext}}(\mathbf{R})}{M}\cdot\nabla_{\mathbf{V}}\right) f_{\text{B}}(\mathbf{R},\mathbf{V};t) = \xi\nabla_{\mathbf{V}}\cdot\left(\mathbf{V} + \frac{k_{\text{B}}T}{M}\nabla_{\mathbf{V}}\right) f_{\text{B}}(\mathbf{R},\mathbf{V};t) \tag{12.9.31}$$

The derivation can also be adapted to the technically more difficult case of a large hard sphere in a bath of small spheres, where the instantaneous nature of the collisions means that the Liouville operator no longer has the simple form given by (12.9.4).[119]

Equation (7.3.20) suggests that correlations in the velocity of the brownian particle decay on a time scale $1/\xi$. Hence, in the high-friction limit, the velocity distribution relaxes rapidly and the evolution of $f_{\text{B}}(\mathbf{R},\mathbf{V};t)$ at long times reduces to that of the spatial distribution, i.e. the single-particle density given by

$$\rho_{\text{B}}(\mathbf{R},t) = \int f_{\text{B}}(\mathbf{R},\mathbf{V};t)\text{d}\mathbf{V} \tag{12.9.32}$$

An evolution equation[120] for $\rho_{\text{B}}(\mathbf{R};t)$ can be derived from (12.9.32) by an expansion in powers of the small parameter $(k_{\text{B}}T/M)^{1/2}/\Sigma\xi$ via a multiple time scale analysis[118] similar to that already described; the result is the Smoluchowski equation:

$$\frac{\partial\rho_{\text{B}}(\mathbf{R},t)}{\partial t} = \nabla_{\mathbf{R}}\cdot D\big(\nabla_{\mathbf{R}} - \beta\mathbf{F}_{\text{ext}}(\mathbf{R})\big)\rho_{\text{B}}(\mathbf{R},t) \tag{12.9.33}$$

where D, the self-diffusion constant, is related to ξ by (7.3.17). The Smoluchowski equation can be viewed as a generalisation of the diffusion equation (8.2.3) to the case where an external force acts on the brownian particle and is more easily obtained by the route which leads to that result. The current density $\mathbf{j}_{\text{B}}(\mathbf{R},t)$ of a brownian particle in a dilute solution is given by the constitutive relation (7.7.3), i.e.

$$\mathbf{j}_{\text{B}}(\mathbf{R},t) = \zeta\rho_{\text{B}}(\mathbf{R},t)\mathbf{F}_{\text{ext}}(\mathbf{R}) - D\nabla\rho_{\text{B}}(\mathbf{R},t) \tag{12.9.34}$$

Insertion of this expression in the continuity equation (8.2.1) for $\rho_{\text{B}}(\mathbf{R},t)$ leads immediately to (12.9.33), since the mobility $\zeta = \beta D$.

To assess the relevance to dilute colloidal dispersions of the evolution equations (12.9.31) and (12.9.33) we must return to the time scale comparison made at the start of this section. Equation (8.4.3) shows that the decay of a transverse current fluctuation of wavenumber k is characterised by a viscous

relaxation time τ_η equal to $\rho_{\rm m}\eta k^2$ where, in the present context, η is the shear viscosity of the suspending fluid and $\rho_{\rm m}$ is its mass density. For $k \approx 1/\Sigma$ the relaxation time can be interpreted as being roughly the time required for a shear perturbation to propagate over a distance equal to the diameter of the brownian particle. The shortest brownian time scale is $\tau_{\rm B} = 1/\xi$ which, from Stokes's law (7.3.18), is related to τ_η within a numerical factor by

$$\tau_{\rm B} \approx \frac{\rho_M}{\rho_{\rm m}}\tau_\eta \tag{12.9.35}$$

where $\rho_M = 6M/\pi\Sigma^3$ is the mass density of the brownian particle. Hence a separation of brownian and bath time scales such that $\tau_{\rm B} \gg \tau_\eta$ would require ρ_M to be much larger than $\rho_{\rm m}$, or $M \gg (\Sigma/\sigma)^3$, a condition which is far more difficult to satisfy than the one requiring $(m/M)^{1/2}$ to be much less than unity. To avoid sedimentation of the colloidal particles, experiments are usually carried out on suspensions for which $\rho_M \approx \rho_{\rm m}$, so that in practice a full separation of time scales cannot be achieved; the dynamics of the bath particles involve slowly decaying shear modes which relax on the same time scale as the velocity of the brownian particle. This means that the Fokker–Planck equation in the local form represented by (12.9.31) is not in general applicable and must be generalised to account for memory effects linked to correlated recollisions between the particles of the bath and the brownian particle.[121] The limitations of the Fokker–Planck equation do not extend to the Smoluchowski equation, since the spatial distribution of the brownian particle relaxes on the much longer, configurational time scale $\tau_{\rm c}$. It is, however, the Smoluchowski equation which is the more relevant to calculations of experimentally measurable quantities.

The Fokker–Planck equation for the distribution function $f_{\rm B}^{(n)}(\mathbf{R}^n, \mathbf{V}^n; t)$ of a suspension consisting of n interacting brownian particles in a bath of N much lighter particles can be derived from the Liouville equation for the phase space probability density of the $(N+n)$-particle system by a multiple time scale method or a physically less transparent, projection operator technique.[122–124] The Smoluchowski equation for the n-particle density $\rho^{(n)}(\mathbf{R}^n, t)$ can then be obtained by integration over particle velocities. These manipulations are inevitably more complicated than those leading to the corresponding single-particle expressions. We therefore limit ourselves to sketching what is involved in the case of the Smoluchowski equation. Two modifications of (12.9.33) are required. The first is straightforward. Allowance must be made for the interaction between brownian particles, meaning that the external force in (12.9.33) must be augmented by the sum over ℓ of the force $\mathbf{F}_\ell$ acting on particle ℓ. That force is itself the sum of two terms, since there will be contributions both from direct interactions with other particles and from bath-induced forces, of which the most important is the depletion force.[125] The second modification is of a more subtle nature. As a brownian particle moves through the bath it experiences a frictional force proportional to its velocity, an effect that already appears in the single-particle case. However, the motion of the particle also creates a flow field

in the solvent, which influences the motion of other particles, giving rise to an additional, 'hydrodynamic' interaction. On the time scale for which the Smoluchowski equation is valid the time required for the effect of the flow field to reach other brownian particles is so short that the hydrodynamic interaction is essentially instantaneous. The total frictional force on particle ℓ can then be written as

$$\mathbf{F}_\ell^\xi = -M \sum_{m=1}^{n} \boldsymbol{\xi}_{\ell m} \cdot \mathbf{V}_m \tag{12.9.36}$$

The quantity $\boldsymbol{\xi}_{\ell m}$ is a component of a friction matrix $\boldsymbol{\Xi}$ defined as

$$\boldsymbol{\xi}_{\ell m} = \frac{\beta}{M} \int_0^\infty \langle \delta \mathbf{F}_\ell(0) \delta \mathbf{F}_m(-s) \rangle_{\text{bath}} \, \mathrm{d}s \tag{12.9.37}$$

where $\delta \mathbf{F}_\ell(s)$ is the fluctuating force exerted at time s on particle ℓ by the bath for fixed locations of all brownian particles. The definition provided by (12.9.36) shows that $\boldsymbol{\xi}_{\ell m}$ depends explicitly on the coordinates of particles ℓ and m and implicitly on those of all other brownian particles; the hydrodynamic forces are therefore fundamentally many-body in character. The diagonal element $\boldsymbol{\xi}_{\ell\ell}$ determines the frictional exerted on particle ℓ by virtue of its own velocity, but this is not the same as the friction coefficient of an isolated particle in the same solvent; hydrodynamic interactions around a circuit of particles mean that the motion of particle ℓ can be reflected back on itself, thereby influencing the value of $\boldsymbol{\xi}_{\ell\ell}$. The Smoluchowski equation that emerges when the factors listed have been allowed for, but in the absence of an external force field, is

$$\frac{\partial \rho_{\text{B}}^{(n)}(\mathbf{R}^n, t)}{\partial t} = \sum_\ell \sum_m \nabla_\ell \cdot \mathbf{D}_{\ell m} \cdot \left(\nabla_m - \beta \mathbf{F}_m \right) \rho_{\text{B}}^{(n)}(\mathbf{R}^n, t) \tag{12.9.38}$$

where $\mathbf{D}_{\ell m}$ is a component of a diffusion tensor matrix $\mathbf{D}$; the matrices $\mathbf{D}$ and $\boldsymbol{\Xi}$ are related by a generalisation of Einstein's relation (7.3.17):

$$\mathbf{D} = \frac{k_{\text{B}} T}{M} \boldsymbol{\Xi}^{-1} \tag{12.9.39}$$

Calculation of the friction tensors requires the solution of the Navier–Stokes equation for the fluid velocity field, with boundary conditions imposed at the surfaces of the moving particles. This is a highly complex problem that can be solved, even approximately, only in the low velocity, high dilution regime.[123,126] If hydrodynamic interactions are ignored, the diagonal elements of the matrix $\mathbf{D}$ are equal to $D\mathbf{I}$, where $\mathbf{I}$ is the 3×3 identity matrix, and the off-diagonal elements vanish. Equation (12.9.38) then reduces to

$$\frac{\partial \rho_{\text{B}}^{(n)}(\mathbf{R}^n, t)}{\partial t} = \sum_\ell \nabla_\ell \cdot D \left(\nabla_\ell - \beta \mathbf{F}_\ell \right) \rho_{\text{B}}^{(n)}(\mathbf{R}^n, t) \tag{12.9.40}$$

The Smoluchowski equation can be written more compactly as

$$\frac{\partial \rho_{\mathrm{B}}^{(n)}(\mathbf{R}^n;t)}{\partial t} = -i\mathcal{S}\rho_{\mathrm{B}}^{(n)}(\mathbf{R}^n,t) \tag{12.9.41}$$

where $\mathcal{S}$ is the Smoluchowski operator. There is an obvious analogy with the Liouville operator $\mathcal{L}$, which has the form appropriate to newtonian mechanics. In the liouvillian description of the dynamics the time evolution of the phase space distribution function is determined by the unitary operator $\exp(-i\mathcal{L}t)$ and that of an arbitrary dynamical variable by the operator $\exp(i\mathcal{L}t)$. Here, however, it can be shown[127] that the evolution of a dynamical variable is controlled not by $\exp(i\mathcal{S}t)$, as analogy would suggest, but by the operator $\exp(-i\tilde{\mathcal{S}}t)$, where $\tilde{\mathcal{S}}$ differs from $\mathcal{S}$ by a change in sign of the $\mathbf{F}_m$ in (12.9.38). In the notation of Section 7.1 the formal expression for the time autocorrelation function of a dynamical variable, A say, is therefore

$$C_{AA}(t) = \langle A(t)A^* \rangle = \left(A, \exp(-i\tilde{\mathcal{S}}t)A\right) \tag{12.9.42}$$

The difference between newtonian and brownian propagators reflects the irreversibility of brownian dynamics, which has its origin in the frictional forces exerted on the brownian particles by the bath. The prescription provided by (12.9.42), when combined with approximations of the type discussed in Chapters 7–9 provide a basis for the calculation of time correlation functions descriptive, in particular, of concentration fluctuations and collective diffusion in colloidal dispersions.

The Smoluchowski equation was arrived at from what was initially a fully deterministic description of the system by progressive elimination of the degrees of freedom of the bath. The more traditional derivation starts with the stochastic equations of motion of a system of n interacting, brownian particles, corresponding to the high-friction limit of a set of Langevin equations similar to (7.3.1) but expanded to include the effect of interparticle forces. If the friction coefficient in (7.3.1) is sufficiently large, the inertial term on the left-hand side can be neglected. If, in addition, the contribution to the force on particle ℓ arising from interactions with other particles is added to the right-hand side, (7.3.1) can be rearranged to give an a set of coupled equations of motion of the form

$$\dot{\mathbf{R}}_\ell(t) = \zeta\left[-\nabla_\ell V_n(\mathbf{R}^n) + \delta\mathbf{F}_\ell(t)\right] \tag{12.9.43}$$

where $\zeta = 1/M\xi$ is the mobility defined by (7.7.2) and $\delta\mathbf{F}_\ell$ is the fluctuating force which appears in (12.9.37). The potential energy $V_n(\mathbf{R}^n)$ incorporates both the direct interactions between particles and those induced by the bath, but hydrodynamic interactions have been ignored. These equations can be shown[114] to lead to the Smoluchowski equation in the simplified form given by (12.9.40), but they are important in their own right, not least because their use allows the numerical simulation of brownian motion. The link with (12.9.40) is easily

established, given that the n-particle density must satisfy the continuity equation

$$\frac{\partial \rho_{\mathrm{B}}^{(n)}(\mathbf{R}^n,t)}{\partial t} = -\sum_{\ell} \nabla_\ell \cdot \dot{\mathbf{R}}_\ell(t)\rho_{\mathrm{B}}^{(n)}(\mathbf{R}^n,t)$$
$$= \sum_{\ell} \nabla_\ell \cdot \zeta\left[\nabla_\ell V_n(\mathbf{R}^n) - \delta\mathbf{F}_\ell\right]\rho_{\mathrm{B}}^{(n)}(\mathbf{R}^n,t) \quad (12.9.44)$$

As $t \to \infty, \rho_{\mathrm{B}}^{(n)}(\mathbf{R}^n,t)$ will approach its equilibrium form, proportional to $\exp\left[-\beta V_n(\mathbf{R}^n)\right]$, the right-hand side of (12.9.44) will vanish, and the two terms within square brackets must therefore cancel each other. It follows that in the long-time limit $\delta\mathbf{F}_\ell = -k_{\mathrm{B}}T\nabla_\ell \ln \rho_{\mathrm{B}}^{(n)}(\mathbf{R}^n)$. Equation (12.9.40) is therefore recovered if it is assumed that the same relationship applies away from equilibrium, i.e. if

$$\delta\mathbf{F}_\ell(t) = -k_{\mathrm{B}}T\frac{\nabla_\ell \rho_{\mathrm{B}}^{(n)}(\mathbf{R}^n,t)}{\rho_{\mathrm{B}}^{(n)}(\mathbf{R}^n,t)} \quad (12.9.45)$$

for all t.

12.10 DYNAMICAL DENSITY FUNCTIONAL THEORY

We saw in Chapter 6 that density functional theory can be applied successfully to the calculation of the single particle density $\rho^{(1)}(\mathbf{R})$ and associated, static properties of a fluid under confinement or subject to an external force field, the key requirement being the availability of a good approximation for the free energy functional $\mathcal{F}[\rho^{(1)}]$. It is therefore natural to seek a generalisation of the theory which describes the dynamics of inhomogeneous fluids in cases, for example, where the system is initially out of equilibrium or when it is driven by a time-dependent, external field. That generalisation is provided by *dynamical density functional theory*, or DDFT, which focuses on the time evolution of the time-dependent, single-particle density $\rho(\mathbf{R},t)$. (As in the previous section, we omit the superscript (1) for sake of notational simplicity, together with the subscript B.) The dynamical theory was originally formulated for systems of interacting brownian particles suspended in a bath of solvent molecules.[128,129] Within the theory, interaction between the brownian particles and the bath is assumed to lead to quasi-instantaneous thermalisation of the particle velocities. This is the situation in which the time dependence of the full, n-particle density is described by the Smoluchowski equation (12.9.38), which provides the starting point for the derivation of the DDFT equation. We shall assume, however, that conditions are such that the many body, hydrodynamic interactions between particles are negligible. The Smoluchowski equation (12.9.38) then takes the simplified form given by (12.9.40).

We start by rewriting (12.9.40) in terms of the mobility:

$$\frac{\partial \rho^{(n)}(\mathbf{R}^n,t)}{\partial t} = \sum_{i=1}^{n} \nabla_i \cdot \zeta \left[k_B T \nabla_i + \nabla_i V_n(\mathbf{R}^n) \right] \rho^{(n)}(\mathbf{R}^n,t) \tag{12.10.1}$$

where

$$V_n(\mathbf{R}^n) = \sum_i \sum_{j<i} v(\mathbf{R}_i,\mathbf{R}_j) + \sum_i \phi(\mathbf{R}_i) \tag{12.10.2}$$

is the total potential energy; here the interactions between particles are assumed to be pairwise-additive and ϕ represents any external potential that may be present. The evolution equation for the single-particle density $\rho(\mathbf{R},t) \equiv \rho^{(1)}(\mathbf{R};t)$ can be derived from (12.10.1) by integrating both sides over the coordinates of the remaining $(n-1)$ particles. The calculation follows the same lines that lead to the YBG equation (4.2.5), which relates the single-particle and pair densities of a fluid at equilibrium. By proceeding in this way it is found that

$$\begin{aligned} \frac{\partial \rho(\mathbf{R}_1,t)}{\partial t} &= \nabla_1 \cdot \zeta \left[k_B T \nabla_1 \rho(\mathbf{R}_1,t) + \rho(\mathbf{R}_1,t) \nabla_1 \phi(\mathbf{R}_1) \right] \\ &\quad + \nabla_1 \cdot \zeta \int \rho^{(2)}(\mathbf{R}_1,\mathbf{R}_2;t) \nabla_1 v(\mathbf{R}_1,\mathbf{R}_2) \mathrm{d}\mathbf{R}_2 \end{aligned} \tag{12.10.3}$$

The same result can be deduced much more easily from the single-particle Smoluchowski equation (12.9.33) simply by adding the mean force due to interaction with the remaining particles to the external force $\mathbf{F}_{\text{ext}} = -\nabla_1 \phi(\mathbf{R}_1)$.

Two approximations are now made. First, the instantaneous pair density $\rho^{(2)}(\mathbf{R}_1,\mathbf{R}_2;t)$ in (12.10.3) is replaced by the pair density $\rho^{(2)}(\mathbf{R}_1,\mathbf{R}_2)$ of a fluid in thermodynamic equilibrium for which the particle density, $\rho(\mathbf{R})$, is equal to $\rho(\mathbf{R},t)$. This is reasonable assumption for dense fluids, where the pair structure is dominated by excluded volume effects. For a fluid at equilibrium, (3.5.4) and (4.2.5) together imply that

$$\int \rho^{(2)}(\mathbf{R}_1,\mathbf{R}_2) \nabla_1 v(\mathbf{R}_1,\mathbf{R}_2) \mathrm{d}\mathbf{R}_2 = -k_B T \rho(\mathbf{R}_1) \nabla c^{(1)}(\mathbf{R}_1) \tag{12.10.4}$$

where $c^{(1)}(\mathbf{R})$ is the single-particle direct correlation function of an inhomogeneous fluid, defined by (3.5.1). The second approximation is to assume that (3.5.1) carries over to the non-equilibrium situation, with the same, excess free energy functional $\mathcal{F}_{\text{ex}}[\rho^{(1)}]$ as in the equilibrium case. Then substitution of (12.10.4) and (3.5.1) in (12.10.3) shows that

$$\frac{\partial \rho(\mathbf{R},t)}{\partial t} = \nabla \cdot \zeta \left(\rho(\mathbf{R},t) \nabla \frac{\delta \mathcal{F}[\rho(\mathbf{R},t)]}{\delta \rho(\mathbf{R},t)} \right) \tag{12.10.5}$$

where

$$\mathcal{F} = \mathcal{F}_{\text{id}} + \mathcal{F}_{\text{ex}} + \int \phi(\mathbf{R},t) \rho(\mathbf{R},t) \mathrm{d}\mathbf{R} \tag{12.10.6}$$

is the total free energy functional, in which the ideal contribution is given by (3.1.22) and allowance is made for a possible time dependence of the external potential. Equation (12.10.5) is the DDFT equation. Written in this form it also allows for a spatial dependence of the mobility; in the more commonly occurring situation, ζ appears as a constant prefactor on the right-hand side and the quantity $\xi^{-1} = m\zeta$ serves to define the time scale. If there are no interactions between particles, $\mathcal{F}_{\text{ex}} = 0$, and (12.10.5) leads back to (12.9.33). By defining the local chemical potential as $\mu[\rho(\mathbf{R},t)] = \delta\mathcal{F}[\rho(\mathbf{R},t)]/\delta\rho(\mathbf{R},t)$, which is a natural generalisation of the thermodynamic relation (2.3.8), the DDFT equation (for constant ζ) can be written in the intuitively appealing form first suggested by Evans[130]:

$$\zeta^{-1}\frac{\partial}{\partial t}\rho(\mathbf{R},t) = \nabla\big[\rho(\mathbf{R},t)\nabla\mu(\mathbf{R},t)\big] \tag{12.10.7}$$

The quantity $-\nabla\mu(\mathbf{R},t)$ plays the role of a driving force that acts on a particle located at $\mathbf{R}$ at time t.

In its applications the DDFT equation must be solved numerically for a given initial condition $\rho(\mathbf{r},0)$ and a physically motivated choice of approximate free energy functional; the extension to multi-component systems is straightforward.[131] It also applies[132] to particles obeying newtonian rather than stochastic dynamics in those situations where rapid thermalisation of velocities is ensured by a high collision rate ν, the only difference being that ζ must be replaced by $1/m\nu$. Efforts have been made to go beyond the Smoluchowski regime by shifting the emphasis from the single-particle density to the distribution function $f(\mathbf{R},\mathbf{V};t)$, the time evolution of which is described by the Fokker–Planck equation (12.9.31). The local density, local particle current and local stress tensor are all expressible in terms of $f(\mathbf{R},\mathbf{V};t)$ and its pair counterpart, $f^{(2)}(\mathbf{R},\mathbf{V},\mathbf{R}',\mathbf{V}';t)$, which allows contact to be made with the flow equations of hydrodynamics.[133]

Equation (12.10.5) and its variants have been applied to a wide range of mostly colloid-related problems. An important, early application concerned the onset of spinodal decomposition in colloidal fluids; the discussion that follows is based on the work of Archer and Evans.[129] Figure 12.18 shows the liquid–gas coexistence curve and spinodal line in the density–temperature plane for a fluid of particles interacting via a Yukawa potential (1.2.2); in the Figure η is the packing fraction of the hard cores and the reduced temperature is expressed in terms of the integrated strength a of the attractive part of the potential:

$$a = -\int_d^\infty v(R)\mathrm{d}\mathbf{R} \tag{12.10.8}$$

The spinodal line, which is also pictured in the density–pressure plane in Figure 5.12, is the locus of points at which the isothermal compressibility diverges or, equivalently, the second derivative of the free energy, $(\partial^2 F/\partial^2 V)_T$

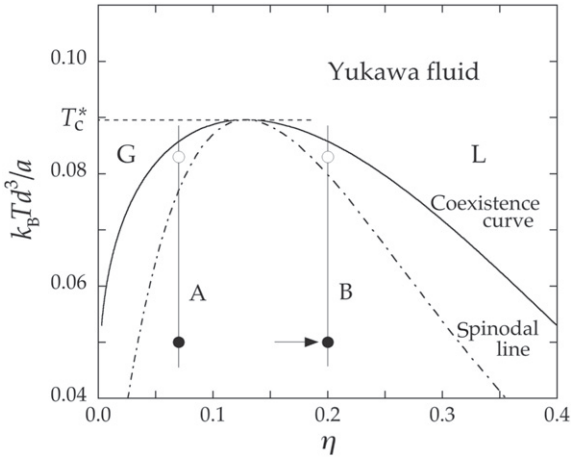

FIGURE 12.18 Liquid–gas coexistence curve and spinodal line of a Yukawa fluid. Open circles mark the regions in which nucleation of liquid droplets may occur, if the fluid is quenched along line A, or of gas bubbles if quenched along line B. Black circles show the region in which spinodal decomposition occurs and the arrow marks the thermodynamic state to which the system is quenched in the calculations described in the text. *Redrawn with permission from Ref. 129* © *American Institute of Physics.*

vanishes. In the regions of the density–temperature plane lying between the coexistence curve and the spinodal, which can be reached by quenching the homogeneous liquid or gas along an isochore, the initially homogeneous fluid becomes metastable in the sense that it is stable against small fluctuations in density. Phase separation requires the nucleation and subsequent growth[134] of small liquid droplets, if the quench is made along line A in Figure 12.18, or small gas bubbles, if made along line B. Nucleation is an example of a 'rare event'; the existence of a large free energy barrier means that the metastable state may be long lived. However, if the quench continues beyond the spinodal, the fluid becomes thermodynamically unstable against density fluctuations, however small, and the rapid growth of domains corresponding to one or other of the two emerging phases, liquid in one case and gas in the other, leads to spinodal decomposition. The early and intermediate stages of this process, in which no sharp interfaces have yet formed, can be described within the framework of DDFT. No external field is involved, so the free energy functional is simply $\mathcal{F} = \mathcal{F}_{\rm id} + \mathcal{F}_{\rm ex}$.

We start by supposing that a small, local fluctuation occurs around the initial, bulk density $\rho_{\rm b}$:

$$\delta\rho(\mathbf{R}, t) = \rho(\mathbf{R}, t) - \rho_{\rm b} \tag{12.10.9}$$

Since the fluctuation is small, we can approximate the excess contribution to the free energy function by the quadratic expansion (4.3.11) around the free energy of the homogeneous phase. Then substitution of (3.1.22), (4.3.11) and

(12.10.9) in (12.10.5) leads to an evolution equation for $\delta\rho(\mathbf{R};t)$:

$$(\zeta k_{\mathrm{B}}T)^{-1}\frac{\partial\delta\rho(\mathbf{R},t)}{\partial t} = \nabla^2\delta\rho(\mathbf{R},t) - \rho_{\mathrm{b}}\nabla^2\int\delta\rho(\mathbf{R},t)c^{(2)}(|\mathbf{R}-\mathbf{R}'|;\rho_{\mathrm{b}})\,\mathrm{d}\mathbf{R}' - \nabla^2\left(\delta\rho(\mathbf{R},t)\int\delta\rho(\mathbf{R}',t)c^{(2)}(|\mathbf{R}-\mathbf{R}'|;\rho_{\mathrm{b}})\,\mathrm{d}\mathbf{R}'\right) \tag{12.10.10}$$

At short times it is sufficient to retain only those terms that are linear in $\delta\rho(\mathbf{R},t)$; the last term on the right-hand side may therefore be discarded. Then, on taking Fourier transforms of the remaining terms, we find that

$$(\zeta k_{\mathrm{B}}T)^{-1}\frac{\partial\rho_{\mathbf{k}}(t)}{\partial t} = -k^2\rho_{\mathbf{k}}(t)[1-\rho_{\mathrm{b}}\hat{c}(k)] \tag{12.10.11}$$

where $\hat{c}(k)$ is the transform of the (pair) direct correlation of the bulk fluid. Equation (12.10.11) has an exponential solution given by

$$\delta\rho_{\mathbf{k}}(t) = \delta\rho_{\mathbf{k}}(0)\exp[-\gamma(k)t] \tag{12.10.12}$$

with

$$\gamma(k) = \zeta k_{\mathrm{B}}Tk^2\big[1-\rho_{\mathrm{b}}\hat{c}(k)\big] = \frac{\zeta k_{\mathrm{B}}Tk^2}{S(k)} \tag{12.10.13}$$

where $S(k)$ is the structure factor of the bulk fluid, which is related to $\hat{c}(k)$ by (3.6.10). In both the stable and metastable phases $S(k)$ is finite for all k; a small density fluctuation therefore decays on a time scale $1/\gamma(k)$. On approaching the spinodal, $S(k)$ diverges as $k\to 0$, so long-wavelength fluctuations become increasingly long lived. Below the spinodal there is no longer a physically meaningful structure factor, but the damping coefficient $\gamma(k)$ can still be defined by the first equality in (12.10.13) through the definition of the direct correlation function as the second functional derivative (3.5.2) of $\mathcal{F}_{\mathrm{ex}}$. An explicit expression can therefore be obtained from an approximate free energy functional appropriate to the system of interest. For a model system, such as the Yukawa fluid, described by a pair potential consisting of a hard-sphere core and an attractive tail, $w(R)$, a suitable choice[129] would be that contained in the grand potential functional (6.6.6), i.e.

$$\mathcal{F}_{\mathrm{ex}}[\rho] = \mathcal{F}_{\mathrm{ex},d}[\rho] + \frac{1}{2}\iint\rho(\mathbf{R})w(\mathbf{R}-\mathbf{R}')\rho(\mathbf{R})\mathrm{d}\mathbf{R}\,\mathrm{d}\mathbf{R}' \tag{12.10.14}$$

where $\mathcal{F}_{\mathrm{ex},d}$ is the excess free energy functional of hard spheres of diameter d; this is well approximated by the fundamental measure theory of Section 6.5. Calculations for the Yukawa potential shows that $\gamma(k)$ is negative for $k<k_{\mathrm{c}}$, where k_{c} is a critical wavenumber having a value dependent on temperature and bulk density. Density fluctuations in that range of k therefore grow exponentially with time, leading to spinodal instability. An example of

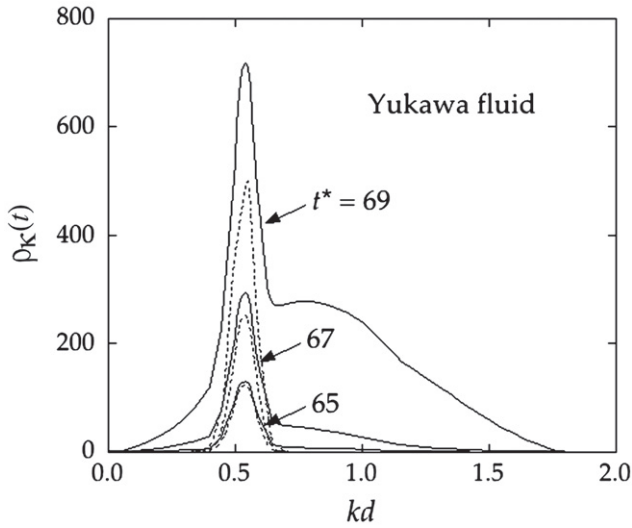

FIGURE 12.19 Predictions of dynamic density functional theory for the growth of Fourier components of the single-particle density of a Yukawa fluid quenched along line B of Figure 12.18. The broken curves show the results of a linear approximation and the full curves include the contribution from a quadratic term; see text for details. The unit of time is the relaxation time τ_c defined by (12.9.1) and $\rho_{\mathbf{k}}(0) = 10^{-8}$. *Redrawn with permission from Ref. 129* © *American Institute of Physics.*

the growth of $\rho_{\mathbf{k}}(t)$ when the fluid is quenched along line B in Figure 12.18, is shown in Figure 12.19, where the unit of time is the configurational relaxation time τ_c defined by (12.9.1) and $\rho_{\mathbf{k}}(0)$ is arbitrarily set equal to 10^{-8}. The peak occurs at a wavenumber k_0 corresponding to the minimum in $\gamma(k)$; this provides a measure of the mean size, $\lambda_0 \approx 2\pi/k_0$, of the domains of liquid or, in this case, gas that develop in the early stages of spinodal decomposition. Similar behaviour had been predicted in the pioneering work of Cahn and Hilliard,[135] based on the square-gradient approximation (6.2.12).

At somewhat longer times, use of the linear approximation cannot be justified. The effect of the quadratic correction to the linear theory may be estimated[129] by including the third term on the right-hand side of (12.10.10). The evolution equation for the Fourier components is now

$$(\zeta k_B T)^{-1} \frac{\partial \rho_{\mathbf{k}}(t)}{\partial t} = -k^2 \rho_{\mathbf{k}}(t)[1 - \rho_b \hat{c}(k)] + \frac{1}{(2\pi)^3} \int \mathbf{k} \cdot \mathbf{k}' \rho_{\mathbf{k}'}(t) \hat{c}(k') \rho_{|\mathbf{k}-\mathbf{k}'|}(t) d\mathbf{k}' \tag{12.10.15}$$

The additional, non-linear term acts in a mode coupling sense, since its effect is to couple together density fluctuations of different wavenumber. As Figure 12.19

illustrates, this leads to a marked spread, mostly to larger k, in the spectrum of wavenumbers that contribute to the time evolution of $\rho_{\mathbf{k}}(t)$. A broad component also appears at intermediate times, lying beyond the single peak predicted by the linear approximation. The position of the first peak scarcely changes with time, but the overall width of the non-linear spectrum suggests that there is a wide distribution in size of the domains corresponding to the conjugate phase.

Other problems to which DDFT has been successfully applied include the growth of a colloidal crystal from an initial nucleus[136] and the non-equilibrium sedimentation of interacting colloidal particles under the influence of gravity.[137] The theoretical predictions can in many cases be tested against the results of brownian dynamics simulations.[138] This is a computational technique which in most respects resembles molecular dynamics except that the particle trajectories are computed, not from Newton's equations, but from the coupled, stochastic equations of motion given by (12.9.43). In this way, for example, it has been shown that use of a mean field, excess free energy functional is justified in the case of gaussian-core particles, a system that serves as a model of interacting polymer coils confined to a cavity of variable radius.[139]

REFERENCES

[1] For introductory treatments, see: (a) Barrat, J.L. and Hansen, J.P., 'Basic Concepts for Simple and Complex Fluids'. Cambridge University Press, Cambridge, 2003. (b) Witten, T.A., 'Structured Fluids: Polymers, Colloids, Surfactants'. Oxford University Press, New York, 2004.

[2] Hertlein, C., Helden, L., Gambassi, A., Dietrich, S. and Bechinger, C., *Nature* **45**, 172 (2008).

[3] See, e.g., Shelley, J.C., Shelley, M.Y., Reeder, R.C., Bandyopadhyay, S., Moore, P.B. amd Klein, M.L., *J. Phys. Chem. B* **105**, 9785 (2001).

[4] Noid, W.G., Chu, J.W., Ayton, G.S., Krishna, V., Izekov, S., Voth, G.A., Das, A. and Andersen, H.C., *J. Chem. Phys.* **128**, 244114 (2008).

[5] (a) Doi, M., 'Introduction to Polymer Physics'. Oxford University Press, New York, 1996. (b) Rubinstein, M. and Colby, R.H., 'Polymer Physics'. Oxford University Press, New York, 2003.

[6] (a) Flory, P.J., 'Statistical Mechanics of Chain Molecules'. John Wiley, New York, 1969. (b) de Gennes, P.G., 'Scaling Concepts in Polymer Physics'. Cornell University Press, Ithaca, 1979. (c) Doi, M. and Edwards, S.F., 'The Theory of Polymer Dynamics'. Oxford University Press, New York, 1986. (d) des Cloizeaux, J. and Jannink, G., 'Polymers in Solution'. Oxford University Press, New York, 1989. (e) Grosberg, A.Yu. and Khokhlov, A.R., 'Statistical Physics of Macromolecules'. AIP Press, New York, 1994.

[7] Pelissetto, A. and Hansen, J.P., *J. Chem. Phys.* **122**, 134904 (2005).

[8] Flory, P.J. and Krigbaum, W.R., *J. Chem. Phys.* **18**, 1086 (1950).

[9] Grosberg, A.Y., Khalutur, P.G. and Khoklov, A.R., *Macromol. Chem. Rapid Commun.* **3**, 709 (1982).

[10] Dautenhahn, J. and Hall, C.K., *Macromolecules* **27**, 5399 (1994).

[11] Krakoviack, V., Hansen, J.P. and Louis, A.A., *Phys. Rev. E* **67**, 041801 (2003).

[12] Ruelle, D., 'Statistical Mechanics: Rigorous Results'. W.A. Benjamin, London, 1969.
[13] Grassberger, P. and Hegger, R., J. Chem. Phys. **102**, 6881 (1995).
[14] Stillinger, F.H., *J. Chem. Phys.* **65**, 3968 (1976).
[15] Lang, A., Likos, C.N., Watzlawek, M. and Löwen, H., *J. Phys. Condens. Matter* **12**, 5087 (2000).
[16] Louis, A.A., Bolhuis, P.G. and Hansen, J.P., *Phys. Rev. E* **62**, 7961 (2000).
[17] des Cloizeaux, J., *J. Phys. (Paris)* **36**, 281 (1975).
[18] Bolhuis, P.G., Louis, A.A., Hansen, J.P. and Meijer, E.J., *J. Chem. Phys.* **114**, 4296 (2001).
[19] (a) Witten, T.A. and Pincus, P.A., *Macromolecules* **19**, 2501 (1986). (b) Likos, C.N., *Phys. Reports* **348**, 267 (2001).
[20] Likos, C.N., Löwen, H., Watzlawek, M., Abbas, B., Jucknische, O., Algaier, J., and Richter, D., *Phys. Rev. Lett.* **80**, 4450 (1998).
[21] Pierleoni, C., Capone, B. and Hansen, J.P., *J. Chem. Phys.* **127**, 171102 (2007).
[22] (a) Edwards, S.F., *Proc. Phys. Soc.* **88**, 265 (1966). (a) Daoud, M., Cotton, J.P., Farnoux, B., Jannink, G., Sarma, G., Benoit, H., Duplessix, C., Picot, C. and de Gennes, P.G., *Macromolecules* **8**, 804 (1975).
[23] D'Adamo, G., Pelissetto, A. and Pierleoni, C., *J. Chem. Phys.* **137**, 024901 (2012).
[24] Vettorel, T., Besold, G. and Kremer, K., *Soft Matter* **6**, 2282 (2010).
[25] (a) Bang, J. and Lodge, T.P., *Macromol. Res.* **16**, 51 (2005). (b) Capone, B., Coluzza, I. and Hansen, J.P., *J. Phys. Condens Matter* **23**, 194102 (2011).
[26] Note, however, that some systematic deviations from strictly gaussian statistics have been detected in analysis of data from both neutron scattering experiments and computer simulations. See Beckrich, P., Johner, A., Semenov, A.N., Obukhov, S.P., Benoît, H. and Wittner, J.P., *Macromolecules* **40**, 3805 (2007).
[27] Ref. 1(a), pp. 103–6.
[28] (a) Schweizer, K.S. and Curro, J.G., *Phys. Rev. Lett.* **58**, 246 (1987). (b) Curro, J.G., Schweizer, K.S., Grest, G.S and Kremer, K., *J. Chem. Phys.* **91**, 1357 (1989). (c) Schweizer, K.S. and Curro, J.G., *Adv. Chem. Phys.* **98**, 1 (1997).
[29] See, e.g., Yethiraj, A., *J. Phys. Chem. B* **113**, 1539 (2009).
[30] (a) Laria, D., Wu, D. and Chandler, D., *J. Chem. Phys.* **95**, 4444 (1991). (b) Schweizer, K.S. and Yethiraj, A., *J. Chem. Phys.* **98**, 9053 (1993).
[31] Krakoviack, V., Hansen, J.P. and Louis, A.A., *Europhys. Lett.* **58**, 53 (2002).
[32] Clark, A.J. and Guenza, M.G., *J. Chem. Phys.* **132**, 044902 (2010).
[33] Lekkerkerker, H.N.W. and Tuinier, R., 'Colloids and the Depletion Interaction'. Springer, Heidelberg, 2011.
[34] See, e.g., Hunter, R.J., 'Foundations of Colloid Science', vol. 1, Section 4.4. Clarendon Press, Oxford, 1987.
[35] (a) Alexander, S., *J. Physique* **38**, 983 (1977). (b) de Gennes, P.G., *Macromolecules* **13**, 1069 (1980).
[36] Milner, S.T., Witten, T.A. and Cates, M.E., *Macromolecules* **21**, 2610 (1988).
[37] Coluzza, I. and Hansen, J.P., *Phys. Rev. Lett.* **100**, 016104 (2008).
[38] de Gennes, P.G. *Adv. Colloid Interface Sci.* **27**, 189 (1987).
[39] Pusey, P.N. and van Megen, W., *Nature* **320**, 340 (1986).
[40] Barrat, J.L. and Hansen, J.P., *J. Physique* **47**, 1547 (1986). See also Pusey, P.N., *J. Physique* **48**, 709 (1987).
[41] Wilding, N.B. and Sollich, P. *J. Chem. Phys.* **133**, 224102 (2010).
[42] Biben, T., Hansen, J.P. and Barrat, J.L., *J. Chem. Phys.* **98**, 7330 (1993).
[43] Buzzaccaro, S., Rusconi, R. and Piazza, R., *Phys. Rev. Lett.* **99**, 098301 (2007).

[44] Bannerman, M.N., Lue, L. and Woodcock, L.V., *J. Chem. Phys.* **132**, 084507 (2010). The equation of state is of the form proposed by Speedy, R.J., *J. Phys. Condens. Matter* **10**, 4387 (1998) but with revised values of the parameters.
[45] Piazza, R., Buzzaccaro, S., Secchi, E. and Parola, A., *Soft Matter* **8**, 7112 (2012).
[46] (a) Asakura, S. and Oosawa, F., *J. Chem. Phys.* **22**, 1255 (1954). (b) Asakura, S. and Oosawa, F., *J. Polymer Sci.* **33**, 123 (1958). See also Vrij, A., *Pure Appl. Chem.* **48**, 471 (1976).
[47] Lekkerkerker, H.N.W., Poon, W.C.K., Pusey, P.N., Stroobants, A. and Warren, P.B., *Europhys. Lett.* **20**, 559 (1992).
[48] Dijkstra, M., van Rooij, R., Roth, R. and Fortini, A., *Phys. Rev. E* **73**, 0141404 (2006).
[49] Ilett, S.M., Orrock, A., Poon, W.C.K. and Pusey, P.N., *Phys. Rev. E* **51**, 1344 (1995).
[50] Louis, A.A., Bolhuis, P.G., Meijer, E.J. and Hansen, J.P., *J. Chem. Phys.* **117**, 1893 (2002).
[51] Bolhuis, P.G., Louis, A.A. and Hansen, J.P., *Phys. Rev. Lett.* **89**, 128302 (2002).
[52] The discussion here is limited to the case when $q \leq 1$, the 'colloid limit'. For phase behaviour in the extreme 'protein limit', $q \gg 1$ see Bolhuis, P.G., Meijer, E.J. and Louis, A.A., *Phys. Rev. Lett.* **90**, 068304 (2003).
[53] Mao, Y., Cates, M.E. and Lekkerkerker, H.N.W., *Physica A* **222**, 10 (1995).
[54] Dijkstra, M., van Roij, R. and Evans, R., *Phys. Rev. E* **52**, 5744 (1999).
[55] Biben, T. and Hansen, J.P., *J. Phys. Condens. Matter* **3**, F65 (1991).
[56] Vliegenthart, G.A. and Lekkerkerker, H.N.W., *J. Chem. Phys.* **112**, 5364 (2000).
[57] Noro, M.G. and Frenkel, D., *J. Chem. Phys.* **113**, 2941 (2000).
[58] (a) van Roij, R., Dijkstra, M. and Hansen, J.P., *Phys. Rev. E* **59**, 2010 (1999). (b) van Roij, R. and Evans, R., *J. Phys. Condens. Matter* **11**, 1004 (1999).
[59] Löwen, H., Hansen, J.P. and Madden, P.A., *J. Chem. Phys.* **98**, 3275 (1993).
[60] Car, R. and Parrinello, M., *Phys. Rev. Lett.* **55**, 247 (1985).
[61] We ignore any non-coulombic component of the external potential.
[62] Verwey, E.J.W. and Overbeek, J.T.G., 'Theory of Stability of Lyophobic Colloids'. Elsevier, Amsterdam, 1948.
[63] Belloni, L., *Colloids Surf.* **A140**, 227 (1998).
[64] Löwen, H. and Allahyarov, E., *J. Phys. Condens. Matter* **10**, 4147 (1998).
[65] Crocker, J.C. and Grier, D.G., *Phys. Rev. Lett.* **73**, 352 (1994).
[66] Bocquet, L., Trizac, E. and Aubouy, M., *J. Chem. Phys.* **117**, 8138 (2002).
[67] Aubouy, M., Trizac, E. and Bocquet, L., *J. Phys. A: Math. Gen.* **36**, 5835 (2003).
[68] (a) Alexander, A., Chaikin, P.M., Grant, P., Morales, G.J., Pincus, P. and Hone, D.J., *J. Chem. Phys.* **80**, 5776 (1984). (b) Trizac, E., Bocquet, L., Aubouy, M. and von Grünberg, H.H., *Langmuir* **19**, 4027 (2003).
[69] For a review, see Naji, A., Jungblut, S., Moreira, A.G. and Netz, R.R., *Physica A* **352**, 131 (2005).
[70] Rouzina, I. and Bloomfield, V.A., *J. Phys. Chem.* **100**, 9977 (1996).
[71] Samaj, L. and Trizac, E., *Phys. Rev. E* **84** 041401 (2011).
[72] Ruzicka, B., Zaccarelli, E., Zulian, L., Angelini, R., Sztucki, M., Moussaïd, A., Narayanan, T. and Sciortino, F., *Nat. Mater.* **10**, 56 (2011).
[73] Tanaka, H., Meunier, J. and Bonn, D., *Phys. Rev. E* **69**, 031404 (2004).
[74] Leote de Carvalho, R.J.F., Trizac, E. and Hansen, J.P., *Phys. Rev. E* **61**, 1634 (2000).
[75] Chapot, D., Bocquet, L. and Trizac, E., *J. Chem. Phys.* **120**, 3969 (2004).
[76] (a) Chandrasekhar, S., 'Liquid Crystals', 2nd edn. Cambridge University Press, Cambridge, 1992. (b) de Gennes, P.G. and Prost, J., 'The Physics of Liquid Crystals', 2nd edn. Oxford

University Press, New York, 1993. (c) Chaikin, P.M. and Lubensky, T.C., 'Principles of Condensed Matter Physics'. Cambridge University Press, Cambridge, 1995.
[77] (a) Frenkel, D., *In* 'Liquids, Freezing and Glass Transition', Part II (J.P. Hansen, D.Levesque and J. Zinn-Justin, eds). North-Holland, Amsterdam, 1991. (b) Vroege, G.J. and Lekkerkerker, *Rep. Prog. Phys.* **55**, 1241, (1992).
[78] Onsager, L., *Ann. N.Y. Acad. Sci.* **51**, 627 (1949).
[79] Frenkel, D., *J. Phys. Chem.* **92**, 3280 (1988). See also *J. Phys. Chem.* **93**, 5314 (1988) (Erratum).
[80] Kayser, R.F. and Raveché, H.J., *Phys. Rev. A* **17**, 2067 (1978).
[81] (a) Parsons, J.D., *Phys. Rev. A* **19**, 1225 (1979). (b) Lee, S.D., *J. Chem. Phys.* **87**, 4792 (1987).
[82] Colot, J.L., Wu, X.G., Xu, H. and Baus, M., *Phys. Rev. A* **38**, 2022 (1988).
[83] (a) Frenkel, D. and Mulder, B.M., *Mol. Phys.* **55**, 1171 (1985). (b) Frenkel, D., *Mol. Phys.* **60**, 1 (1987).
[84] (a) Somoza, A.M. and Tarazona, P., *J. Chem. Phys.* **91**, 517 (1989). (b) Poniewierski, A. and Sluckin, T.J., *Phys. Rev. A* **43**, 6837 (1991).
[85] (a) Stroobants, A., Lekkerkerker, H.N.W. and Frenkel, D., *Phys. Rev. A* **36**, 2929 (1987). (b) Holyst, R. and Poniewierski, A., *Phys. Rev. A* **39**, 2742 (1989).
[86] Lebowitz, J.L. and Perram, W.J., *Mol. Phys.* **50**, 1207 (1983).
[87] Poniewierski, A. and Holyst, R., *Phys. Rev. A* **41**, 6871 (1990).
[88] Bolhuis, P. and Frenkel, D., *J. Chem. Phys.* **106**, 666 (1997).
[89] Polson, J.M. and Frenkel, D., *Phys. Rev. E* **56**, R6260 (1997).
[90] Eppenga, R. and Frenkel, D., *Mol. Phys.* **52**, 1303 (1984).
[91] Harnau, L., Costa, D. and Hansen, J.P., *Europhys. Lett.* **53**, 729 (2001).
[92] Pickett, G.T. and Schweizer, K.S., *J. Chem. Phys.* **110**, 6597 (1999).
[93] Dijkstra, M., Hansen, J.P. and Madden, P.A., *Phys. Rev. E* **55**, 3044 (1997).
[94] Marechal, M., Cuetos, A., Martinez-Haya, B. and Dijkstra, M., *J. Chem. Phys.* **134**, 094501 (2011).
[95] Veerman, J.A.C. and Frenkel, D., *Phys. Rev. A* **45**, 5632 (1992).
[96] van der Kooij, F.M. and Lekkerkerker, H.N.W., *Phil. Trans. R. Soc. A* **359**, 985 (2001).
[97] Zaccarelli, E., *J. Phys. Condens. Matter* **19**, 323101 (2007).
[98] Sciortino, F. and Zaccarelli, E., *Curr. Opin. Solid State Mater. Sci.* **15**, 246 (2011).
[99] Campbell, A.I., Anderson, V.J., van Duijneveldt, J.S. and Bartlett, P., *Phys. Rev. Lett.* **94**, 208301 (2005).
[100] Stradner, A., Sedgwick, H., Cardinaux, F., Poon, W.C.K., Egelhaaf, S.U. and Schurtenberger, P., *Nature* **432**, 492 (2004).
[101] (a) Sciortino, F., Mossa, S., Zaccarelli, E. and Tartaglia, P., *Phys. Rev. Lett.* **93**, 055701 (2004). (b) Fernandez Toldano, J.C., Sciortino, F. and Zaccarelli, E., *Soft Matter* **5**, 2390 (2009).
[102] Archer, A.J., Pini, D., Evans, R. and Reatto, L., *J. Chem. Phys.* **126**, 014104 (2007).
[103] Sear, R.F. and Gelbart, W.M., *J. Chem. Phys.* **110**, 4582 (1999).
[104] Archer, A.J., Ionescu, C., Pini, D., and Reatto, L., *J. Phys. Condens. Matter* **20**, 415106 (2008).
[105] Bomont, J.M., Bretonnet, J.L. and Costa, D., *J. Chem. Phys.* **132**, 184508 (2010).
[106] Bianchi, E., Blaak, R. and Likos, C.N., *Phys. Chem. Chem. Phys.* **13**, 6397 (2011).
[107] Bianchi, E., Tartaglia, P., Zaccarelli, E. and Sciortino, F., *J. Chem. Phys.* **128**, 144504 (2008).
[108] Bianchi, E., Largo, J., Tartaglia, P., Zaccarelli, E. and Sciortino, F., *Phys. Rev. Lett.* **97**, 168301 (2006).

[109] A point on the percolation line is identified as one for which the bond probability p_B given by (11.10.22) is equal to $1/(f-1)$.
[110] Russo, J., Tartaglia, P. and Sciortino, F., *J. Chem. Phys.* **131**, 014504 (2009).
[111] Weis, J.J. and Levesque, D., *Adv. Polym. Sci.* **185**, 163 (2005).
[112] Miller, M.A., Blaak, R., Lumb, C.N. and Hansen, J.P., *J. Chem. Phys.* **130**, 114507 (2009).
[113] Rovigatti, L. and Sciortino, F., *Phys. Rev. Lett.* **107**, 237801 (2011).
[114] Résibois, P. and De Leener, M., 'Classical Kinetic Theory of Fluids'. Wiley, New York, 1977.
[115] van Kampen, N.G., 'Stochastic Processes in Physics and Chemistry'. North-Holland, Amsterdam, 1981.
[116] For an introduction to multiple time scale methods, see Anderson, J.L., *Am. J. Phys.* **60**, 923 (1992).
[117] Cukier, R.I. and Deutch, J.M., *Phys. Rev.* **177**, 240 (1969).
[118] Bocquet, L., *Am. J. Phys.* **65**, 140 (1997).
[119] Bocquet, L., Piasecki, J. and Hansen, J.P., *J. Stat. Phys.* **76**, 505 and 527 (1994).
[120] Kramers, H.A., *Physica* **7**, 284 (1940).
[121] Bocquet, L. and Piasecki, J., *J. Stat. Phys.* **87**, 1005 (1997).
[122] Mazo, R.M., *J. Stat. Phys.* **1**, 559 (1969).
[123] Deutch, J.M. and Oppenheim, I., *J. Chem. Phys.* **54**, 3547 (1971).
[124] Murphy, T.J. and Aguirre, J.L., *J. Chem. Phys.* **57**, 2098 (1972).
[125] The isotropy of the distribution of bath particles around an isolated B-particle means that there is no depletion force in the case when $n = 1$.
[126] Happel, J. and Brenner, H., 'Low Reynolds Number Hydrodynamics'. Nordhoff, Leiden, 1973.
[127] For a detailed discussion, see Pusey, P.N., *In* 'Liquids, Freezing and the Glass Transition' (J.P. Hansen, D. Levesque and J. Zinn-Justin, eds). North-Holland, Amsterdam, 1991.
[128] Marconi, U.M.B. and Tarazona, P., *J. Chem. Phys.* **110**, 8032 (1999).
[129] Archer, A.J. and Evans, R., *J. Chem. Phys.* **121**, 4246 (2004).
[130] Evans, R., *Adv. Phys.* **28**, 143 (1979).
[131] Archer, A.J., *J. Phys. Condens. Matter* **17**, 1405 (2006).
[132] Archer, A.J., *J. Phys. Condens. Matter* **18**, 5617 (2006).
[133] Marconi, U.M.B. and Melchionna, S., *J. Chem. Phys.* **131**, 04105 (2009).
[134] Onuki, A., 'Phase Transition Dynamics'. Cambridge University Press, Cambridge, 2002.
[135] (a) Cahn, J.W. and Hilliard, J.E., *J. Chem. Phys.* **31**, 688 (1959). (b) Cahn, J.W., *Acta Metall.* **9**, 795 (1961).
[136] van Teefelelen, S., Likos, C.N. and Löwen, H., *Phys. Rev. Lett.* **98**, 188304 (2007).
[137] Royall, C.P., Dzubiella, J., Schmidt, M. and van Blaaderen, A., *Phys. Rev. Lett.* **98**, 188304 (2007).
[138] Ermak, D.L., *J. Chem. Phys.* **62**, 4189 (1975).
[139] Dzubiella, J. and Likos, C.N., *J. Phys. Condens. Matter* **15**, L147 (2003).